THE UNIVERSITY
of ADELAIDE

Faculty of Sciences, Engineering and Technology

School of Physics, Chemistry and Earth Sciences

Department of Physics

Quark Propagator Studies with Overlap Fermions in Lattice QCD

Adam Virgili

Supervisors

Dr. Waseem Kamleh and Prof. Derek Leinweber

March 2023

Contents

Non nobis Domine

Abstract

Lattice QCD is the only first-principles approach to performing calculations in the nonperturbative regime of QCD. Within this paradigm, continuum QCD is discretised and embedded into a finite-volume lattice of Euclidean spacetime points. This process is nontrivial, particularly in the fermion sector. The overlap formalism provides an implementation of fermions on the lattice which incorporates chiral symmetry. Although this is desirable, it comes at great computational expense, restricting the use of overlap fermions to situations where their favourable properties are deemed beneficial or necessary. We make extensive use of overlap fermions in this work. We consider the Landau-gauge overlap quark propagator from dynamical gauge fields for the first time, where the overlap formalism provides a straightforward, prescribed way of extracting the mass and renormalisation functions. Furthermore, the chiral nature and sensitivity to gauge field topology of the overlap operator makes the overlap quark propagator the ideal probe to study the role of centre vortices in dynamical chiral symmetry breaking. To this end, we investigate the effect of centre-vortex modification of QCD ground-state fields on the quark propagator. In order to compute vortex-only quark propagator we perform an extensive investigation into the viability of various smoothing algorithms applied to vortex-only gauge fields, developing novel approaches necessary to satisfy the smoothness condition of the overlap Dirac operator. Given recent suggestions that chiral symmetry could be key to understanding the origin of the low-lying nature of the Roper resonance, we also systematically examine the role of chiral symmetry in the nucleon spectrum by directly comparing the Wilson clover and overlap fermion actions.

I certify that this work contains no material which has been accepted for the award of any other degree or diploma in my name, in any university or other tertiary institution and, to the best of my knowledge and belief, contains no material previously published or written by another person, except where due reference has been made in the text. In addition, I certify that no part of this work will, in the future, be used in a submission in my name, for any other degree or diploma in any university or other tertiary institution without the prior approval of the University of Adelaide and where applicable, any partner institution responsible for the joint award of this degree.

I give permission for the digital version of my thesis to be made available on the web, via the University's digital research repository, the Library Search and also through web search engines, unless permission has been granted by the University to restrict access for a period of time.

I acknowledge the support I have received for my research through the provision of an Australian Government Research Training Program Scholarship.

Adam Virgili

Acknowledgements

I thank first and foremost my supervisors Waseem and Derek for their patience, advice and guidance. I also thank my parents, Carlo and Susan, for all they have done, especially in providing for my material needs. I thank my sister Gemma, and again my father Carlo, for offering their time to proofread this thesis. I am grateful to my fellow physics postgrads Rami and Minh for their friendship and companionship, on and off campus. Finally, I would like to acknowledge and thank everyone who at one stage or another over the past five years was, or continues to be, a significant part of my life.

Chapter 1

Introduction

Quantum chromodynamics (QCD) is the gauge field theory which describes the strong interaction between colour-charged particles, mediated by the gluon gauge boson. In addition to quarks, gluons themselves also carry colour charge, a fact which is reflected in the nonabelian nature of the QCD gauge group SU(3). Gluons are therefore self-interacting. In Chapter 2, we introduce the QCD Lagrangian, motivated by the principle of local gauge symmetry. Furthermore, we shall see that due to the running of the gauge coupling that perturbative techniques breakdown in the low-energy regime, necessitating an alternative approach.

Initially developed in 1974 [1], lattice QCD offers a nonperturbative approach to performing QCD calculations from first principles. Within this paradigm, as outlined in Chapter 3, QCD is transformed from Minkowski to Euclidean space via a Wick rotation. The Euclidean theory is then discretised and embedded in a finite-volume hypercubic lattice. This process is nontrivial, particularly in the fermion sector. As we shall explore in Chapter 4, a naive approach to implementing fermions on the lattice leads to the phenomenon of *fermion doubling*. This problem is resolved via the introduction of the Wilson term, but this approach has its own issues as the term breaks chiral symmetry explicitly. Furthermore, the No-Go theorem precludes the existence of a local, doubler-free and chirally symmetric lattice Dirac operator which has the correct continuum limit. With no obvious solution to this dilemma, it was thought chiral symmetry may never be realised on the lattice. However, the Ginsparg-Wilson relation offers a lattice implementation of chiral symmetry that successfully navigates the limitations imposed by the No-Go theorem for any lattice Dirac operator which satisfies it. One need only find such a lattice Dirac operator, and an explicit solution came about in the form of the overlap Dirac operator.

As a solution to the Ginsparg-Wilson relation, the overlap Dirac operator provides an implementation of chirally symmetric fermions on the lattice, and is sensitive to the topological structures of the gauge field. This, however, comes at significant computational expense due to the presence of the matrix sign function in

the operator. As such, the use of the overlap fermions is typically restricted to situations where these, and its other properties are deemed beneficial. For example, the absence of additive mass renormalisation makes the overlap formalism an excellent choice for computing the quark propagator since the mass and renormalisation functions are extracted in a straightforward, prescribed manner. This is in contrast to the nontrivial process necessary for Wilson-type fermions. In Chapter 5 we compute the Landau-gauge overlap quark propagator on 2+1-flavour dynamical gauge fields for the first time. The observed features of the mass and renormalisation functions are discussed and compared with recent results which used $\mathcal{O}(a)$-improved Wilson fermions on 2-flavour dynamical gauge fields [2].

On the other hand, Wilson-type fermions are used extensively in hadron spectroscopy where the explicit breaking of chiral symmetry is expected to have negligible impact, and the additional computational expense of overlap fermions is difficult to justify. However, it has been suggested that chiral symmetry could be key to understanding the origin of the low-lying nature of $N^*(1440)$, or the Roper resonance [3]. This nucleon resonance has been the subject of significant interest for many years, including several lattice QCD studies. The majority of lattice studies have not observed an excited state energy level in the region of the Roper resonance. In Chapter 6 we systematically examine the role of chiral symmetry in the low-lying nucleon spectrum by directly comparing the Wilson-type clover fermion action with the overlap fermion action, such that the only difference between respective simulations is the choice of fermion action.

Where overlap fermions are important, not only due to their chiral nature but also their sensitivity to topological structures of the gauge field, is in the study of the role of centre vortices in the nonperturbative aspects of QCD. In particular, we are interested in dynamical chiral symmetry breaking. There is already strong evidence which supports centre vortices as the mechanism which underpins both key features of nonperturbative QCD, dynamical chiral symmetry breaking and confinement. However, the majority of these studies were conducted in the pure-gauge sector, and found quantitative discrepancies in their results. In the context of the quark propagator, this manifests as remnant dynamical mass generation in the mass function following vortex removal. This is a signal of dynamical chiral symmetry breaking which persists after vortex removal despite being fully reproduced on a vortex-only background. Buoyed by recent studies of the static quark potential and gluon propagator which found the presence of dynamical quarks resolved similar discrepancies which were present in the pure-gauge sector [4, 5], we consider the impact

of vortex modification on the Landau-gauge overlap quark propagator in dynamical QCD in Chapter 8.

However, to compute the overlap quark propagator on a vortex-only background, the gauge fields must be smoothed. This is to ensure the otherwise rough centre-vortex fields satisfy the smoothness condition of the overlap Dirac operator, necessary to guarantee its locality. In past pure-gauge studies, cooling has sufficed to this end, but is not ideal for smoothing vortex-only gauge fields derived from dynamical backgrounds. In Chapter 7, we examine the applicability of existing SU(3) gauge field smoothing algorithms to Z(3) vortex-only gauge fields. Due to the proportionality of the centre-vortex links to the identity, naive applications of these methods are either ineffectual or limited in scope, containing subtle issues which are not obviously manifest. To overcome these issues we introduce *centrifuge preconditioning*, a novel method applied prior to smoothing that rotates the links away from the centre while preserving the fundamental structure of the vortex field. Additionally, the concept of *vortex-preserved annealed smoothing* is formulated to ensure the smoothing procedure maintains the underlying vortex structure. Through the application of these new methods in the context of annealed smoothing we develop smoothing 'recipes' which when applied to vortex-only gauge fields are able to successfully achieve the desired smoothness condition.

The work presented in this thesis is summarised in Chapter 9.

Chapter 2

Quantum Chromodynamics

The foundation of any field theory is its Lagrangian. A gauge field theory is defined by a Lagrangian that exhibits gauge symmetry, which is to say that the Lagrangian is invariant under a set of local transformations which form a Lie group – the gauge group of a theory. The gauge symmetry fundamentally shapes the structure of the Lagrangian, and by extension its associated gauge field theory. QCD is the gauge field theory which describes the strong interaction mediated by the gluon gauge boson between the colour-charged particles of the Standard Model. In addition to quarks, gluons themselves also carry colour charge, a fact which is reflected in the nonabelian nature of the QCD gauge group SU(3).

Quarks, as fermions, are described by the Dirac equation. The free Dirac Lagrangian for the Minkowski metric tensor $\eta^{\mu\nu}$ with signature $(-,+,+,+)$ is given by [6, 7]

$$\mathcal{L}_{\text{Dirac}} = -\overline{\psi}(x)\,(\gamma^{\mu}\partial_{\mu} + m)\,\psi(x)\,, \tag{2.1}$$

where m is the quark mass, the Dirac gamma matrices γ^{μ} are defined by

$$\{\gamma^{\mu}\,,\,\gamma^{\nu}\} = 2\eta^{\mu\nu}\,, \tag{2.2}$$

and ψ is a Dirac spinor. Dirac spinors carry a Dirac index and a colour index (both of which have been suppressed here for notational convenience), whilst x denotes the spacetime position. The adjoint spinor $\overline{\psi}$ is given by

$$\overline{\psi} \equiv \psi^{\dagger}\gamma^{0}i\,. \tag{2.3}$$

If the Dirac Lagrangian is to form part of the QCD Lagrangian, it must be invariant under the local transformation

$$\begin{aligned} \psi(x) &\to G(x)\,\psi(x)\,, \\ \overline{\psi}(x) &\to \overline{\psi}(x)\,G^{\dagger}(x)\,. \end{aligned} \tag{2.4}$$

where $G(x) \in \mathrm{SU}(3)$ acts on the colour index of the Dirac spinor. Whilst the mass term transforms trivially under these local transformations

$$m\overline{\psi}(x)\,\psi(x) \to m\overline{\psi}(x)\,G^{\dagger}(x)\,G(x)\,\psi(x) = m\overline{\psi}(x)\,\psi(x)\,, \tag{2.5}$$

the derivative term does not. Following Ref. [8] whilst noting the different choice of conventions, let us consider the derivative of ψ at x in the direction of the vector n^{μ} using the formal definition of the derivative. Applying the local transformation to the derivative term

$$\begin{aligned} n^{\mu}\partial_{\mu}\psi(x) &= \lim_{\epsilon\to 0}\frac{1}{\epsilon}\left[\psi(x+\epsilon n) - \psi(x)\right] \\ &\to \lim_{\epsilon\to 0}\frac{1}{\epsilon}\left[G(x+\epsilon n)\,\psi(x+\epsilon n) - G(x)\,\psi(x)\right]\,, \end{aligned} \tag{2.6}$$

offers no straightforward transformation law, or meaningful interpretation. This is a consequence of $\psi(x+\epsilon n)$ and $\psi(x)$ transforming independently. However, through the introduction of a comparator $U(y,x) \in \mathrm{SU}(3)$, which has the property $U(x,x) = 1$ and transforms according to

$$U(y,x) \to G(y)\,U(y,x)\,G^{\dagger}(x)\,, \tag{2.7}$$

we can define a new *covariant* derivative, such that the covariant derivative of ψ at x in the n^{μ} direction is given by

$$n^{\mu}D_{\mu}\psi(x) = \lim_{\epsilon\to 0}\frac{1}{\epsilon}\left[\psi(x+\epsilon n) - U(x+\epsilon n, x)\,\psi(x)\right]\,. \tag{2.8}$$

This quantity transforms according to

$$\begin{aligned} n^{\mu}D_{\mu}\psi(x) &= \lim_{\epsilon\to 0}\frac{1}{\epsilon}\left[\psi(x+\epsilon n) - U(x+\epsilon n, x)\,\psi(x)\right] \\ &\to \lim_{\epsilon\to 0}\frac{1}{\epsilon}\left[G(x+\epsilon n)\,\psi(x+\epsilon n) - G(x+\epsilon n)\,U(x+\epsilon n, x)\,G^{\dagger}(x)\,G(x)\,\psi(x)\right] \\ &= \lim_{\epsilon\to 0} G(x+\epsilon n)\,\frac{1}{\epsilon}\left[\psi(x+\epsilon n) - U(x+\epsilon n, x)\,\psi(x)\right] \\ &= \left(\lim_{\epsilon\to 0} G(x+\epsilon n)\right)\left(\lim_{\epsilon\to 0}\frac{1}{\epsilon}\left[\psi(x+\epsilon n) - U(x+\epsilon n, x)\,\psi(x)\right]\right) \\ &= G(x)\,n^{\mu}D_{\mu}\psi(x)\,, \end{aligned} \tag{2.9}$$

which implies the covariant derivative of the Dirac spinor has the same transformation law as the Dirac spinor

$$D_\mu \psi(x) \to G(x)\, D_\mu \psi(x)\,, \tag{2.10}$$

that is, it co-varies with the Dirac spinor. Replacing the regular derivative in the Dirac Lagrangian of Eq. (2.1) with the covariant derivative

$$\mathcal{L}_{\text{Dirac}} = -\overline{\psi}(x)\,(\gamma^\mu D_\mu + m)\,\psi(x)\,, \tag{2.11}$$

the Lagrangian is now invariant under the local gauge transformations of Eq. (2.4)

$$\begin{aligned}
\mathcal{L}_{\text{Dirac}} &= -\overline{\psi}(x)\,(\gamma^\mu D_\mu + m)\,\psi(x) \\
&= -\overline{\psi}(x)\,(\gamma^\mu D_\mu \psi(x) + m\psi(x)) \\
&\to -\overline{\psi}(x)\,G^\dagger(x)\,(\gamma^\mu G(x) D_\mu \psi(x) + mG(x)\,\psi(x)) \\
&= -\overline{\psi}(x)\,G^\dagger(x)\,G(x)\,(\gamma^\mu D_\mu \psi(x) + m\psi(x)) \\
&= -\overline{\psi}(x)\,(\gamma^\mu D_\mu + m)\,\psi(x) \\
&= \mathcal{L}_{\text{Dirac}}\,.
\end{aligned} \tag{2.12}$$

The explicit form of the covariant derivative is found by considering the comparator for infinitesimal ϵ. Since $U(x,x) = 1$, we can expand the comparator as

$$U(x + \epsilon n, x) = 1 + ig\epsilon n^\mu A^a_\mu t^a + \mathcal{O}(\epsilon^2)\,, \tag{2.13}$$

where $t^a = \frac{\lambda^a}{2}$ and λ^a are the eight Gell-Mann matrices, the generators of SU(3), each of which is associated with a vector field A^a_μ. Geometrically, $A^a_\mu t^a$ is a connection, but interpreted physically, each A^a_μ is a gluon field. The extracted constant g is identified with the gauge field coupling. It is then straightforward to show that the covariant derivative is given by

$$D_\mu = \partial_\mu - igA^a_\mu t^a\,, \tag{2.14}$$

and not difficult to verify that it transforms according to Eq. (2.10).

The commutator of the covariant derivative defines the field strength tensor

$$[D_\mu\,,\, D_\nu] \equiv -igF^a_{\mu\nu} t^a\,. \tag{2.15}$$

where

$$F^a_{\mu\nu} = \partial_\mu A^a_\nu - \partial_\nu A^a_\mu + g f^{abc} A^b_\mu A^c_\nu \,, \tag{2.16}$$

is the field strength tensor, and f^{abc} are the structure constants defined by

$$\left[t^a \,,\, t^b\right] = i f^{abc} t^c \,, \tag{2.17}$$

both of which are totally antisymmetric. The field strength tensor is not itself gauge invariant, but it is possible to find gauge invariant terms which contain it, from which we can construct the pure-gauge Lagrangian. Furthermore, any such terms must have dimension of E^4, where E is energy, to ensure the dimensional consistency of the Lagrangian and renormalisability of the theory. In fact, if we postulate time reversal and parity symmetry, only one term that is purely a function of the gauge fields A^a_μ meet these requirements. As such, the pure-gauge part of the QCD Lagrangian is

$$\mathcal{L}_{\text{gauge}} = -\frac{1}{2}\text{Tr}\left[\left(F^a_{\mu\nu} t^a\right)^2\right] = -\frac{1}{4}\left(F^a_{\mu\nu} F^{\mu\nu}_a\right) \,. \tag{2.18}$$

The Dirac Lagrangian meets the dimensionality criteria, and as has been shown, is gauge invariant. Since the terms of Dirac and pure-gauge Lagrangians exhaust all possible terms which meet these criteria, the QCD Lagrangian is straightforwardly constructed by combining them, such that it is given by

$$\mathcal{L}_{\text{QCD}} = \overline{\psi}(x)\left(\not{D} + m\right)\psi(x) - \frac{1}{4}\left(F^a_{\mu\nu} F^{\mu\nu}_a\right) \,, \tag{2.19}$$

where we have used Feynman slash notation $\gamma^\mu D_\mu \equiv \not{D}$.

2.1 Running coupling

In the previous section we treated the coupling g as a constant value. Strictly speaking this is not the case and its value depends on the energy scale of an interaction. This running of the QCD coupling is governed by a Callan-Symanzik equation

$$\mu \frac{d}{d\mu} g(\mu) = \beta(g(\mu)) \,, \tag{2.20}$$

where μ is the energy scale and the β-function can be expressed as a perturbative series

$$\beta(x) = -\sum_{n=0} b_n x^{2n+3} \,, \tag{2.21}$$

where the coefficients of the first two terms

$$b_0 = \frac{1}{(4\pi)^2}\left(11 - \frac{2}{3}n_f\right), \tag{2.22}$$

$$b_1 = \frac{1}{(4\pi)^4}\left(102 - \frac{38}{3}n_f\right), \tag{2.23}$$

are independent of renormalisation scheme, and n_f is the number of fermions with mass $\ll \mu$. To first order, Eq. (2.20) is

$$\mu\frac{d}{d\mu}g(\mu) = -b_0 g^3(\mu), \tag{2.24}$$

which has solution [9]

$$g^2(\mu) = \frac{1}{2b_0 \ln(\mu/\Lambda)}. \tag{2.25}$$

Here, Λ is the QCD scale parameter and is dependent on choice of renormalisation scheme.

The coupling $g(\mu)$ is related to $\alpha_s(\mu)$, the QCD analogue of the fine structure constant from QED, according to

$$\alpha_s(\mu) \equiv \frac{g^2(\mu)}{4\pi}. \tag{2.26}$$

From the form of Eq. (2.25), it is clear that $g^2(\mu) \to 0$, and thus $\alpha_s(\mu) \to 0$, as $\mu \to \infty$. This is asymptotic freedom. The small value of α_s at large energy scales permits the use of perturbative techniques to perform calculations in QCD. On the other hand, at energy scales $\mu \sim \Lambda$, quarks and gluons exhibit confinement, $\alpha_s(\mu) \sim 1$, and perturbative techniques breakdown. In this regime other approaches are necessary. The only first-principles approach to performing QCD calculations in this regime is lattice QCD.

Chapter 3

Fundamentals of Lattice QCD

Within the paradigm of lattice QCD, the continuum QCD theory is embedded into a finite-volume lattice of Euclidean spacetime points, and calculations performed numerically. This process is nontrivial, but in this chapter we will outline the fundamental aspects of the process.

3.1 Wick Rotation

The first step in taking QCD from the continuum to the lattice is to transform the theory from Minkowski space to Euclidean space via a Wick rotation. This is necessary due to the oscillatory nature of the complex exponential which appears in the generating functional

$$Z_{\mathrm{QCD}} = \int DAD\overline{\psi}D\psi \exp\left[i \int d^4x \mathcal{L}_{\mathrm{QCD}}\right] , \tag{3.1}$$

which makes numerical computation intractable.

The Euclidean metric tensor is $\delta^{\mu\nu}$ with signature $(+,+,+,+)$ such that contravariance and covariance are equivalent. Euclidean Lorentz indices run over $\mu =$ 1, 2, 3, 4. The Euclidean time coordinate is related to Minkowski time x^0 via a Wick rotation [10],

$$x_4^E = ix^0 , \tag{3.2}$$

The Wick rotation does not affect the spatial coordinates, such that

$$x_j^E = x^j \tag{3.3}$$

where the superscript E denotes Euclidean space, and j, $k \in \{1, 2, 3\}$ correspond to the spatial dimensions. This convention is used throughout the remainder of this chapter. Furthermore, it immediately follows that the components of the partial

derivative change according to

$$\partial_j^E = \partial_j \,, \tag{3.4}$$
$$\partial_4^E = -i\partial_0 \,, \tag{3.5}$$

The effect of this rotation on each sector of the QCD Lagrangian shall now be treated in turn.

3.1.1 Pure-Gauge Sector

First let us consider the pure-gauge sector of the QCD Lagrangian. For the gauge vector field we have

$$-A_a^0 = A_0^a = i(A_4^a)^E \,, \tag{3.6}$$
$$A_a^j = A_j^a = (A_j^a)^E \,. \tag{3.7}$$

Separating out the purely spatial components of the antisymmetric field strength tensor

$$\begin{aligned}
\mathcal{L}_{\text{gauge}} &= -\frac{1}{4} F_{\mu\nu} F^{\mu\nu} \\
&= -\frac{1}{4} \left(\cancelto{0}{F_{00} F^{00}} + F_{0j} F^{0j} + F_{j0} F^{j0} + F_{kj} F^{kj} \right) \\
&= -\frac{1}{4} \left(2F_{0j} F^{0j} + F_{kj} F^{kj} \right) \\
&= -\frac{1}{4} \left(-2F_{0j} F_{0j} + F_{kj} F_{kj} \right) \\
&= \frac{1}{2} F_{0j} F_{0j} - \frac{1}{4} F_{kj} F_{kj} \,.
\end{aligned} \tag{3.8}$$

we can treat each term in turn. From Eqs. (3.4) and (3.7), and the definition of the field strength tensor in Eq. (2.16), it is straightforward to see that the purely spatial components remain unchanged

$$F^{kj} = F_{kj} = F_{kj}^E \,. \tag{3.9}$$

For the components associated with time, however, Eqs. (3.5) and (3.6) imply

$$\begin{aligned}
F_{0j} &= \partial_0 A_j^a - \partial_j A_0^a + g f^{abc} A_0^b A_j^c \\
&= i\partial_4^E (A_j^a)^E - i\partial_j^E (A_4^a)^E + i g f^{abc} (A_4^b)^E (A_j^c)^E \\
&= i(F_{4j}^a)^E \,,
\end{aligned} \tag{3.10}$$

and similarly

$$F^a_{j0} = i(F^a_{j4})^E \,. \tag{3.11}$$

Hence, for the pure-gauge Lagrangian we have

$$\begin{aligned}
\mathcal{L}_{\text{gauge}} &= \frac{1}{2}F_{0j}F_{0j} - \frac{1}{4}F_{ij}F_{ij} \\
&= i^2\frac{1}{2}(F_{4j})^E(F_{4j})^E - \frac{1}{4}(F_{ij})^E(F_{ij})^E \\
&= -\frac{1}{2}(F_{4j})^E(F_{4j})^E - \frac{1}{4}(F_{ij})^E(F_{ij})^E \\
&= -\frac{1}{4}F^E_{\mu\nu}F^{\mu\nu}_E \\
&= -\mathcal{L}^E_{\text{gauge}} \,.
\end{aligned} \tag{3.12}$$

3.1.2 Dirac Sector

Now let us consider the Dirac sector of the QCD Lagrangian. Separating the spatial and time components of the Dirac Lagrangian, and taking the derivative and gauge vector field terms to Euclidean space by applying Eqs. (3.5), (3.4), (3.6) and (3.7), we can write

$$\begin{aligned}
\mathcal{L}_{\text{Dirac}} &= -\overline{\psi}\left(\gamma^\mu\partial_\mu - ig\gamma^\mu A^a_\mu t^a + m\right)\psi \\
&= -\psi^\dagger\gamma^0 i\left(\gamma^0\partial_0 + \gamma^j\partial_j - ig\left[\gamma^0 A^a_0 t^a + \gamma^j A^a_j t^a\right] + m\right)\psi \\
&= -\psi^\dagger\gamma^0 i\left(i\gamma^0\partial^E_4 + \gamma^j\partial^E_j - ig\left[i\gamma^0(A^a_4)^E t^a + \gamma^j(A^a_j)^E t^a\right] + m\right)\psi \,.
\end{aligned} \tag{3.13}$$

Making the identification

$$\gamma^j_E = \gamma^j \,, \tag{3.14}$$

$$\gamma^4_E = i\gamma^0 \,, \tag{3.15}$$

gives a sensible defining relation for the Dirac gamma matrices

$$\{\gamma^\mu \,,\, \gamma^\nu\} = 2\delta^{\mu\nu} \,, \tag{3.16}$$

providing the Euclidean analogue of Eq. (2.2). Inserting the definitions of the Euclidean gamma matrices from Eq. (3.15) and (3.14) into the Dirac Lagrangian of

Eq. (3.13), we have

$$\begin{aligned}\mathcal{L}_{\text{Dirac}} &= -\psi^\dagger\gamma_E^4\left(\gamma_E^4\partial_4^E + \gamma_E^j\partial_j^E - ig\left[\gamma_E^4(A_4^a)^E t^a + \gamma_E^j(A_j^a)^E t^a\right] + m\right)\psi \\ &= -\overline{\psi}\left(\gamma_E^\mu\partial_\mu^E - ig\gamma_E^\mu(A_\mu^a)^E t^a + m\right)\psi \\ &= -\mathcal{L}_{\text{Dirac}}^E\,.\end{aligned} \tag{3.17}$$

3.1.3 Euclidean QCD

Combing the results of the previous sections, in particular Eqs. (3.12) and (3.17), obtains the Euclidean QCD Lagrangian

$$\begin{aligned}\mathcal{L}_{\text{QCD}} &= \mathcal{L}_{\text{Dirac}} + \mathcal{L}_{\text{gauge}} \\ &= -\mathcal{L}_{\text{Dirac}}^E - \mathcal{L}_{\text{gauge}}^E \\ &= -\mathcal{L}_{\text{QCD}}^E\,.\end{aligned} \tag{3.18}$$

Furthermore, Eqs. (3.2) and (3.3) imply

$$\int d^4x = \int dx_0dx_1dx_2dx_3 = \int -idx_1^Edx_2^Edx_3^Edx_4^E = -i\int d^4x_E\,, \tag{3.19}$$

such that the Minkowski QCD action S is related to the Euclidean QCD S_E action by

$$iS = i\int d^4x\mathcal{L}_{\text{QCD}} = i^2\int d^4x_E\mathcal{L}_{\text{QCD}}^E = -\int d^4x_E\mathcal{L}_{\text{QCD}}^E = -S_E\,, \tag{3.20}$$

where we have used Eq. (3.18).

Consequently, the QCD generating functional becomes

$$\begin{aligned}Z_{\text{QCD}} &= \int DAD\overline{\psi}D\psi\exp\left[i\int d^4x\mathcal{L}_{\text{QCD}}\right] \\ &\to \int DAD\overline{\psi}D\psi\exp\left[-\int d^4x\mathcal{L}_{\text{QCD}}^E\right] \\ &= Z_{\text{QCD}}^E\,,\end{aligned} \tag{3.21}$$

and the oscillatory exponential has been removed. Most notably, the Euclidean generating functional resembles the partition function of statistical mechanics, and can be treated as a probability weighting for sampling a given gauge field configuration.

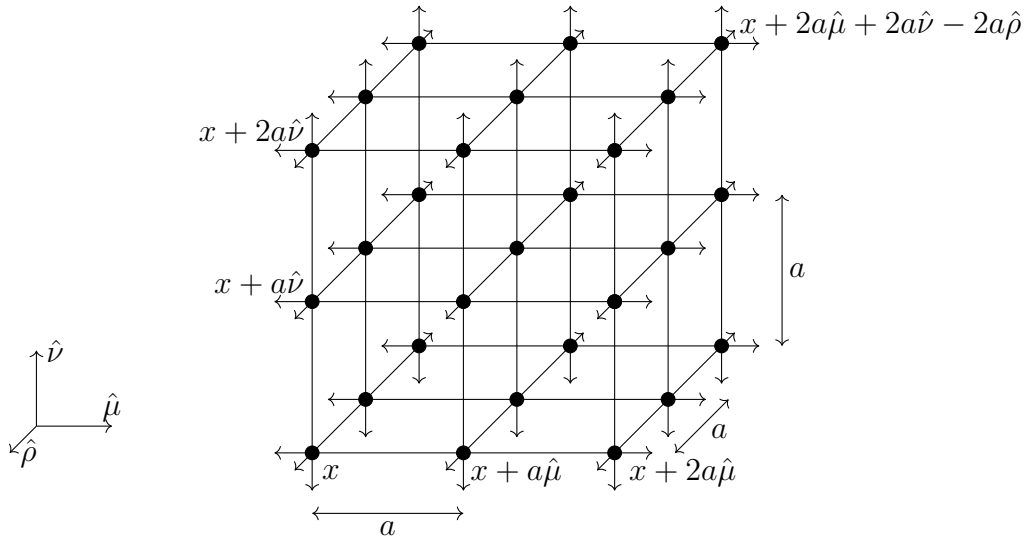

Figure 3.1: A 3-dimensional sublattice with spacing a. The lattice sites $x \in \mathbb{L}$ are represented by black dots.

3.2 Spacetime Discretisation

Before proceeding to discretise the Euclidean QCD theory, we first define the finite-volume Euclidean spacetime lattice in which we will embed the discretised theory. A spacetime lattice $\mathbb{L}$ is defined by the set of Euclidean spacetime points $x \in \mathbb{R}^4$ such that each component of x is an integer multiple of the lattice spacing a, up to the number of lattice sites in that direction. More formally,

$$\mathbb{L} = \left\{ x \in \mathbb{R}^4 \,|\, x_\mu = a n_\mu \,,\, n \in \left(\mathbb{Z}^3_{N_s} \times \mathbb{Z}_{N_t} \right) \right\} \,, \tag{3.22}$$

where $\mathbb{Z}_N$ is the set of integers modulo N. The lattice size is defined by the number of lattice sites in the Euclidean time direction N_t, and each spatial direction N_s, for a total of $N_s^3 N_t$ sites. Formally, the lattice spacetime point adjacent to x in the $\hat{\mu}$ direction is $x + a\hat{\mu}$, but for notational convenience we suppress the lattice spacing throughout this thesis such that it is written $x + \hat{\mu}$.

As we shall see, the process of discretisation and embedding of the continuum theory into the finite-volume lattice is nontrivial, particularly in the fermion sector.

3.3 Naive Fermions

Fermions are defined on the lattice by Dirac spinors ψ, $\overline{\psi}$ which carry the usual indices from continuum QCD at each lattice site $x \in \mathbb{L}$. Naively discretising the

partial derivative operator ∂_μ by the symmetrical finite difference

$$\partial_\mu \to \nabla_\mu = \frac{1}{2a}\left(T_\mu - T_\mu^\dagger\right) , \tag{3.23}$$

where

$$T_\mu \psi(x) = \psi(x+\hat{\mu}) , \tag{3.24}$$
$$T_\mu^\dagger \psi(x) = \psi(x-\hat{\mu}) , \tag{3.25}$$

we arrive at the *naive* discretisation of the free Dirac Lagrangian

$$\mathcal{L}_{\text{Dirac}} = \overline{\psi}(x)\left(\gamma^\mu \nabla_\mu + m\right)\psi(x) , \tag{3.26}$$

or, more explicitly

$$\mathcal{L}_{\text{Dirac}} = \overline{\psi}(x) \sum_\mu \left(\gamma^\mu \frac{\psi(x+\hat{\mu}) - \psi(x-\hat{\mu})}{2a} + m\psi(x) \right) . \tag{3.27}$$

Whilst this reasonable and straightforward approach to implementing fermions on the lattice appears sensible at first glance, it carries a fatal flaw which we shall revisit in Section 4.1. For now, the naive discretisation is sufficient to motivate the introduction of link variables on the lattice.

3.4 Link Variables

To ensure consistency with the continuum theory, we require the lattice Dirac Lagrangian to be invariant under the same local transformations

$$\begin{aligned} \psi(x) &\to G(x)\,\psi(x) , \\ \overline{\psi}(x) &\to \overline{\psi}(x)\,G^\dagger(x) . \end{aligned} \tag{2.4}$$

where $G(x) \in \mathrm{SU}(3)$ acts on the colour index of the Dirac spinor. It is straightforward to see that the mass term in Eq. (3.27) transforms as in the continuum (cf. Eq. (2.5))

$$m\overline{\psi}(x)\,\psi(x) \to m\overline{\psi}\,G^\dagger(x)\,G(x)\,\psi(x) = m\overline{\psi}(x)\,\psi(x) , \tag{3.28}$$

and is invariant. As with the derivative operator in the continuum, this is not the case for the terms which arise from its discretisation, the finite difference operator.

These terms transform as

$$\overline{\psi}(x)\,\psi(x+\hat{\mu}) \to \overline{\psi}(x)\,G^{\dagger}(x)\,G(x+\hat{\mu})\,\psi(x+\hat{\mu})\,, \tag{3.29}$$

$$\overline{\psi}(x)\,\psi(x-\hat{\mu}) \to \overline{\psi}(x)\,G^{\dagger}(x)\,G(x-\hat{\mu})\,\psi(x-\hat{\mu})\,. \tag{3.30}$$

Where, in the continuum, we introduced the comparator, here we introduce a variable defined on the link between neighbouring lattice sites x and $x+\hat{\mu}$, such that it acts as a parallel transport operator between the sites. Defining the link variable in terms of the comparator

$$U_{\mu}(x) \equiv U(x, x+\hat{\mu})\,, \tag{3.31}$$

it necessarily has the same gauge transformation law (cf. Eq. (2.7))

$$U_{\mu}(x) \to U'_{\mu}(x) = G(x)\,U_{\mu}(x)\,G^{\dagger}(x+\hat{\mu})\,. \tag{3.32}$$

Whereas in Chapter 2 an infinitesimal transport was considered, here a finite transport must be considered, and the comparator is defined by the Wilson line [8]

$$U(x, x+\hat{\mu}) \equiv \mathcal{P}\exp\left[-ig\int_0^1 ds \frac{dx^{\mu}}{ds} A^a_{\mu}(x(s))t^a\right] \tag{3.33}$$

along a path from x to $x+\hat{\mu}$, parameterised by s where $\mathcal{P}$ denotes path ordering. Linearly approximating the integral along the link from x to $x+\hat{\mu}$, the link variable is given by [11]

$$U_{\mu}(x) = \exp\left[-iagA_{\mu}(x)\right]\,, \tag{3.34}$$

where no path ordering is needed up to $\mathcal{O}(a)$. Expanding the exponential up to $\mathcal{O}(a)$ then gives

$$U_{\mu}(x) = 1 - iagA_{\mu}(x) + \mathcal{O}(a^2)\,. \tag{3.35}$$

Similarly, starting again at x, but now transporting in the reverse direction from x to $x-\hat{\mu}$, define

$$U_{-\mu}(x) \equiv U(x, x-\hat{\mu})\,, \tag{3.36}$$

such that it transforms according to

$$U_{-\mu}(x) \to U'_{-\mu}(x) = G(x)\,U_{-\mu}(x)\,G^{\dagger}(x-\hat{\mu})\,, \tag{3.37}$$

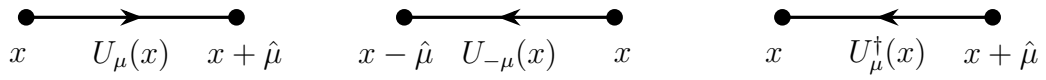

Figure 3.2: Link variables.

and is given by

$$U_{-\mu}(x) = \exp\left[iagA_\mu(x-\hat{\mu})\right] , \tag{3.38}$$

which expanded to $\mathcal{O}(a)$ is

$$U_{-\mu}(x) = 1 + iagA_\mu(x-\hat{\mu}) + \mathcal{O}(a^2) . \tag{3.39}$$

From the above definitions, it follows that

$$U_\mu^\dagger(x) = U_\mu^{-1}(x) = U_{-\mu}(x+\hat{\mu}) . \tag{3.40}$$

which transforms as

$$U_\mu^\dagger(x) \to G(x+\hat{\mu})\, U_\mu^\dagger(x)\, G^\dagger(x) . \tag{3.41}$$

and is given by

$$U_\mu(x) = \exp\left[-iagA_\mu(x)\right] , \tag{3.42}$$

which expanded to $\mathcal{O}(a)$ is

$$U_\mu^\dagger(x) = 1 + iagA_\mu(x) + \mathcal{O}(a^2) . \tag{3.43}$$

A graphical representation of the each of these definition is given in Figure 3.2.

Inserting the appropriate link variables into the naive lattice Dirac Lagrangian we have

$$\mathcal{L} = \overline{\psi}(x) \sum_\mu \left(\gamma^\mu \frac{U_\mu(x)\,\psi(x+\hat{\mu}) - U_\mu^\dagger(x-\hat{\mu})\,\psi(x-\hat{\mu})}{2a} + m\psi(x) \right) . \tag{3.44}$$

This is now gauge invariant since

$$\begin{aligned} \overline{\psi}(x)\, U_\mu(x)\, \psi(x+\hat{\mu}) &\to \overline{\psi}(x)\, G^\dagger(x)\, G(x)\, U_\mu(x)\, G^\dagger(x+\hat{\mu})\, G(x+\hat{\mu})\, \psi(x+\hat{\mu}) \\ &= \overline{\psi}(x)\, U_\mu(x)\, \psi(x+\hat{\mu}) , \end{aligned} \tag{3.45}$$

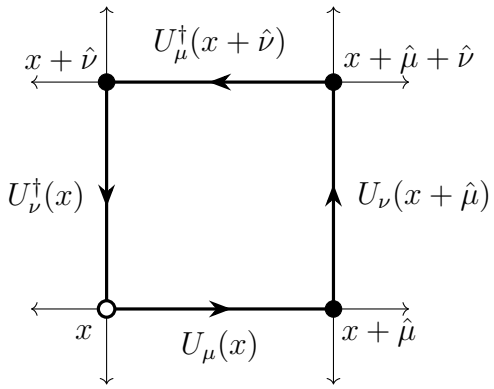

Figure 3.3: Plaquette at x in the μ–ν plane.

and

$$\begin{aligned}\overline{\psi}(x)\,U_\mu^\dagger(x-\hat{\mu})\,\psi(x-\hat{\mu}) &\to \overline{\psi}(x)\,G^\dagger(x)\,G(x)\,U_\mu^\dagger(x-\hat{\mu})\,G^\dagger(x-\hat{\mu})\,G(x-\hat{\mu})\,\psi(x-\hat{\mu}) \\ &= \overline{\psi}(x)\,U_\mu^\dagger(x-\hat{\mu})\,\psi(x-\hat{\mu})\,.\end{aligned} \tag{3.46}$$

Substituting Eqs. (3.35) and (3.43) into the new gauge invariant form of the lattice Dirac Lagrangian of Eq. (3.44) gives

$$\begin{aligned}\mathcal{L} = \overline{\psi}(x)\sum_\mu \Bigg(&\gamma^\mu \frac{[1-iagA_\mu(x)]\;\psi(x+\hat{\mu})}{2a} \\ &-\gamma^\mu \frac{[1+iagA_\mu(x-\hat{\mu})]\;\psi(x-\hat{\mu})}{2a} + m\psi(x)\Bigg) + \mathcal{O}(a^2)\,.\end{aligned} \tag{3.47}$$

Considering only the finite difference terms, and taking the limit $a \to 0$

$$\begin{aligned}&\lim_{a\to 0}\left(\frac{[1-iagA_\mu(x)]\;\psi(x+\hat{\mu}) - [1+iagA_\mu(x-\hat{\mu})]\;\psi(x-\hat{\mu}) + \mathcal{O}(a^2)}{2a}\right) \\ &= \lim_{a\to 0}\left(\frac{\psi(x+\hat{\mu})-\psi(x-\hat{\mu})}{2a}\right) \\ &\qquad - \lim_{a\to 0}\left(\frac{iagA_\mu(x)\,\psi(x+\hat{\mu}) + iagA_\mu(x-\hat{\mu})\,\psi(x-\hat{\mu})}{2a}\right) \\ &= \partial_\mu\psi(x) - igA_\mu(x)\,\psi(x) \\ &\equiv D_\mu(x)\,\psi(x)\,,\end{aligned} \tag{3.48}$$

the continuum covariant derivative is recovered.

3.5 Gauge Action

The elementary plaquette originating at lattice site x in the μ–ν plane, $P_{\mu\nu}(x)$, is given by

$$P_{\mu\nu}(x) = U_\mu(x)\, U_\nu(x+\hat{\mu})\, U_\mu^\dagger(x+\hat{\nu})\, U_\nu^\dagger(x)\,, \tag{3.49}$$

and is represented graphically in Figure 3.3. Under an arbitrary gauge transformation

$$U_\mu(x) \to U'_\mu(x) = G(x)\, U_\mu(x)\, G^\dagger(x+\mu)\,, \tag{3.32}$$

the plaquette $P_{\mu\nu}(x)$, and any other closed loop of gauge link variables on the lattice, transforms as

$$P_{\mu\nu}(x) \to P'_{\mu\nu}(x) = G(x)\, P_{\mu\nu}(x)\, G^\dagger(x)\,. \tag{3.50}$$

Although the plaquette itself is not gauge invariant, it is easy to see that $\mathrm{Tr}\,[P_{\mu\nu}(x)]$ is by the cyclical properties of the trace, and therefore can be used to define gauge invariant quantities on the lattice, in particular the Wilson gauge action given by

$$S_\mathrm{w} = \beta \sum_{x\in\mathbb{L}} \sum_{\mu<\nu} \frac{1}{3}\,\mathrm{Re}\,\mathrm{Tr}\,[1 - P_{\mu\nu}(x)]\ , \tag{3.51}$$

where $\beta = 6/g^2$.

Recalling Eqs. (3.34) and (3.42)

$$U_\mu(x) = \exp\left[-iagA_\mu(x)\right]\ , \tag{3.34}$$
$$U_\mu^\dagger(x) = \exp\left[iagA_\mu(x)\right]\ , \tag{3.42}$$

it follows that

$$\begin{aligned} P_{\mu\nu}(x) = \exp\left\{-iagA_\mu(x)\right\} \exp\left\{-iagA_\nu(x+\hat{\mu})\right\} \\ \times \exp\left\{iagA_\mu(x+\hat{\nu})\right\} \exp\left\{iagA_\nu(x+\hat{\nu})\right\}\ . \end{aligned} \tag{3.52}$$

Applying the Baker-Campbell-Hausdorf formula up to first order in the commutator

$$\exp(A)\exp(B) = \exp\left(A + B + \frac{1}{2}\,[A\,,B] + ...\right) \tag{3.53}$$

it can be shown that

$$\begin{aligned} P_{\mu\nu}(x) &= \exp\left\{-ia^2 g\left(\partial_\mu A^a_\nu(x) - \partial_\nu A^a_\mu(x) + g f^{abc} A^b_\mu(x) A^c_\nu(x)\right) t^a + \mathcal{O}(a^3)\right\} \\ &= \exp\left\{-ia^2 g F_{\mu\nu}(x) + \mathcal{O}(a^3)\right\}\ . \end{aligned} \tag{3.54}$$

A full derivation is given in Appendix A.1.

Dropping the higher order terms and substituting Eq. (3.54) for $P_{\mu\nu}$ into the Wilson gauge action, expanding the exponential gives

$$\begin{aligned} S_{\mathrm{w}} &= \frac{2}{g^2} \sum_{x\in\mathbb{L}} \sum_{\mu<\nu} \mathrm{Re}\,\mathrm{Tr}\left[1 - P_{\mu\nu}(x)\right] \\ &= \frac{2}{g^2} \sum_{x\in\mathbb{L}} \sum_{\mu<\nu} \mathrm{Re}\,\mathrm{Tr}\left[1 - \exp\left\{-ia^2 g F_{\mu\nu}(x)\right\}\right] \\ &= \frac{2}{g^2} \sum_{x\in\mathbb{L}} \sum_{\mu<\nu} \mathrm{Re}\,\mathrm{Tr}\left[1 - \left\{1 + \left(-ia^2 g F_{\mu\nu}(x)\right) + \frac{1}{2}\left(-a^4 g^2 F_{\mu\nu}(x)^2\right)\right\}\right] \\ &= \frac{2}{g^2} \sum_{x\in\mathbb{L}} \sum_{\mu<\nu} \mathrm{Re}\,\mathrm{Tr}\left[\frac{1}{2} a^4 g^2 F_{\mu\nu}(x)^2\right] \\ &= a^4 \sum_{x\in\mathbb{L}} \sum_{\mu<\nu} \mathrm{Re}\,\mathrm{Tr}\left[F_{\mu\nu}(x)^2\right] \\ &= \frac{a^4}{2} \sum_{x\in\mathbb{L}} \sum_{\mu,\nu} \mathrm{Tr}\left[F_{\mu\nu}(x)^2\right] \,, \end{aligned} \tag{3.55}$$

which in the limit $a \to 0$ becomes

$$\begin{aligned} \lim_{a\to 0} S_{\mathrm{w}} &= \lim_{a\to 0} \frac{a^4}{2} \sum_{x\in\mathbb{L}} \sum_{\mu,\nu} \mathrm{Tr}\left[F_{\mu\nu}(x)^2\right] \\ &= \int d^4x\, \frac{1}{2} \mathrm{Tr}\left[F_{\mu\nu}(x)\, F_{\mu\nu}(x)\right] \,, \end{aligned} \tag{3.56}$$

recovering the Euclidean gauge action.

3.6 Numerical Methods

The framework which has been developed over the previous sections provides the foundations to numerically compute observable quantities from first principles. Recalling the generating functional for Euclidean QCD from Subsection 3.1.3, and here considering only the pure-gauge sector with the discretised gauge action S_{gauge}, the vacuum expectation value of an observable O on the lattice is given by

$$\langle O \rangle = \frac{1}{Z_{\mathrm{gauge}}} \int \mathcal{D}U \exp\left(-S_{\mathrm{gauge}}[U]\right) O[U] \,, \tag{3.57}$$

where

$$Z_{\mathrm{gauge}} = \int \mathcal{D}U \exp\left(-S_{\mathrm{gauge}}[U]\right) \,, \tag{3.58}$$

is analogous to the partition function of statistical mechanics. As such, we can use Monte Carlo methods to calculate an approximate value for the expectation value of the observable O, such that

$$\langle O \rangle \approx \frac{1}{N} \sum_{n=1}^{N} O[U_n] \tag{3.59}$$

where N is the total number of gauge field configurations sampled, U_n is the nth gauge field configuration sampled with probability $\propto e^{-S[U_n]}$, and $O[U_n]$ is the value of observable for the configuration U_n. The configurations U_n are generated sequentially via Markov-chain Monte Carlo processes such as the Metropolis-Hastings algorithm [12, 13]. Relatively simple, local update algorithms can potentially suffice for the pure-gauge sector, but become intractable when the action is nonlocal as is the case when fermions are included. More sophisticated algorithms such as Hybrid Monte Carlo [14] are required.

Chapter 4

Fermions on the Lattice

4.1 Fermion Doubling

We return now to the naive discretisation of the fermion Lagrangian from Section 3.4

$$\begin{aligned}\mathcal{L}_{\text{Dirac}} &= \overline{\psi}(x)\left(\not{\nabla} + m\right)\psi(x) \\ &= \overline{\psi}(x)\sum_{\mu}\left(\gamma^{\mu}\frac{U_{\mu}(x)\,\psi(x+\hat{\mu}) - U_{\mu}^{\dagger}(x-\hat{\mu})\,\psi(x-\hat{\mu})}{2a} + m\psi(x)\right),\end{aligned} \tag{4.1}$$

where ∇_{μ} has been redefined from Eq. (3.23) to be the discretisation of the covariant derivative such that

$$D_{\mu} \to \nabla_{\mu} = \frac{1}{2a}\left(T_{\mu} - T_{\mu}^{\dagger}\right), \tag{4.2}$$

where T_{μ} and $T_{\mu}^{\dagger}$ have been redefined as

$$T_{\mu}\psi(x) = U_{\mu}(x)\,\psi(x+\hat{\mu}), \tag{4.3}$$

$$T_{\mu}^{\dagger}\psi(x) = U_{\mu}^{\dagger}(x-\mu)\,\psi(x-\hat{\mu}). \tag{4.4}$$

As alluded to in Section 3.3, the naive formulation suffers from a symmetry under the transformation

$$\psi(x) \to \gamma_5\,\gamma_{\nu}\,e^{ix_{\nu}\pi/a}\,\psi(x) \tag{4.5}$$

which gives rise to a distinct, additional *doubler* fermion species with momentum $p_{\nu} = \frac{\pi}{a}$ for each expected fermion flavour. Applying the transformation successively for each unique combination of one or more directions in d-dimensions results in the presence of $2^d - 1$ doubler fermions for each fermion flavour. For example, applying the transformation first in the $\mu = 1$ direction, and then in the $\mu = 3$ direction, corresponds to a doubler fermion with $p = \left(\frac{\pi}{a}, 0, \frac{\pi}{a}, 0\right)$. In four dimensions this gives rise to fifteen additional and distinct fermion species for each fermion flavour. Crucially, these do not vanish in the continuum limit. This is the well-known *fermion doubling* problem.

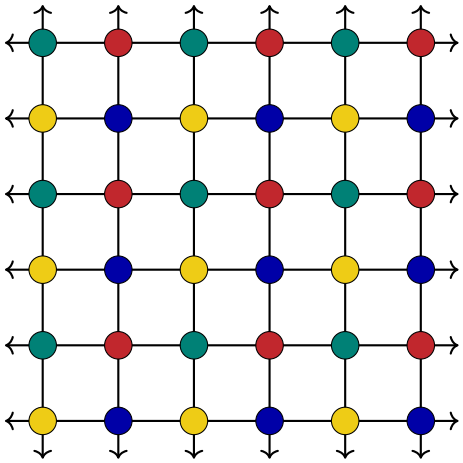

Figure 4.1: Coupling only lattice sites separated by $2a$ produces $2^d = 4$ fermion species in $d = 2$ dimensions. Each colour represents a distinct fermion field.

We can gain graphical insight into the problem by recognising that the lattice finite difference operator ∇_μ couples only lattice sites separated by $2a$. By marking coupled sites with matching colours in Figure 4.1 it is clear how $2^d = 4$ distinct fermion fields arise in $d = 2$ dimensions.

Let us now consider the lattice finite difference operator taken to momentum space

$$\nabla_\mu \to \frac{i}{a} \sin(a p_\mu) \,, \tag{4.6}$$

which has zeroes at $p_\mu = 0$ and $p_\mu = \frac{\pi}{a}$. It therefore follows that

$$\sum_\mu \sin(a p_\mu) = 0 \iff p_\mu \in \left\{ 0 \,, \frac{\pi}{a} \right\} \quad \forall \quad \mu \,. \tag{4.7}$$

giving a total of sixteen zeros – each associated with one of the distinct fermion species. The zero for which $p_\mu = 0 \; \forall \; \mu$ corresponds to the expected, single fermion flavour. The fifteen other zeroes which have at least one component $p_\mu = \frac{\pi}{a}$ each correspond to one of the fifteen additional doubler fermion species. For these zeroes, $p_\mu = \frac{\pi}{a}$ corresponds the symmetry transformation of Eq. (4.5) applied in the $\hat{\mu}$ direction.

Since fermion doublers do not vanish in the continuum limit, the naive formulation of fermions on the lattice introduces significant complications. Fortunately, the naive approach may be modified.

4.2 Wilson Fermions

Wilson resolved the fermion doubling problem through the introduction of an additional term to the naive formulation [1]. This term, the Wilson term, is given by

$$\frac{ra}{2}\Delta\,, \tag{4.8}$$

where Δ is the lattice Laplacian defined as

$$\Delta = \frac{1}{a^2}\sum_{\mu}\left(2 - T_\mu - T_\mu^\dagger\right)\,, \tag{4.9}$$

and r is the Wilson coefficient, typically set to 1. Unlike the finite difference operator, the lattice Laplacian couples adjacent sites. Incorporating this term into the naive fermion Lagrangian, we arrive at the Wilson fermion Lagrangian

$$\mathcal{L} = \overline{\psi}(x)\left(\not{\nabla} + \frac{ra}{2}\Delta + m\right)\psi(x)\,, \tag{4.10}$$

which does not exhibit fermion doubling.

To understand why this is the case, let us consider the Wilson term taken to momentum space

$$\frac{ra}{2}\Delta \to \frac{r}{a}\sum_{\mu}\left[1 - \cos(ap_\mu)\right]\,. \tag{4.11}$$

This term behaves as a supplementary mass term. At $p = 0$, it vanishes, leaving the mass of the single intended fermion species unaltered. However, at momenta associated with each of the doubler fermions, there is an additional contribution of $2r/a$ to the fermion mass for each component $p_\mu = \pi/a$. The masses of the doubler fermions are then given by

$$m + \frac{2rn}{a}\,, \tag{4.12}$$

where n is the number of components of p equal to π/a for a particular doubler species. In the continuum limit $a \to 0$ the doubler fermions become infinitely heavy, decoupling from the theory, and the correct continuum limit is recovered. The masslike behaviour of the Wilson term is not inconsequential, as its presence breaks chiral symmetry explicitly.

4.3 Chiral Symmetry

We now return briefly to continuum QCD. In the continuum, a Dirac Lagrangian obeys chiral symmetry if and only if it is invariant under chiral rotation of the fermion fields

$$\begin{aligned} \psi &\to \psi' = e^{i\alpha\gamma^5}\psi\,, \\ \overline{\psi} &\to \overline{\psi}' = \overline{\psi}e^{i\alpha\gamma^5}\,, \end{aligned} \tag{4.13}$$

where α is a real parameter. Note that the spacetime coordinate has been suppressed for notational convenience. For infinitesimal α the transformation can be written

$$\psi \to \psi' = (1 + i\alpha\gamma^5)\psi + \mathcal{O}(\alpha^2)\,, \tag{4.14}$$

$$\overline{\psi} \to \overline{\psi}' = \overline{\psi}(1 + i\alpha\gamma^5) + \mathcal{O}(\alpha^2)\,. \tag{4.15}$$

Performing the chiral rotation on the massless fermion Lagrangian,

$$\begin{aligned} \mathcal{L}_{m=0} &= \overline{\psi}\,\gamma^\mu D_\mu \psi \\ &\to \overline{\psi}\,(1 + i\alpha\gamma^5)\gamma^\mu D_\mu (1 + i\alpha\gamma^5)\psi + \mathcal{O}(\alpha^2) \\ &= \overline{\psi}\,\gamma^\mu D_\mu \psi + i\alpha\overline{\psi}(\gamma^5\gamma^\mu D_\mu + D_\mu\gamma^\mu\gamma^5)\psi + \mathcal{O}(\alpha^2) \\ &= \overline{\psi}\,\gamma^\mu D_\mu \psi \\ &= \mathcal{L}_{m=0}\,, \end{aligned} \tag{4.16}$$

where we have used

$$\left\{\gamma^\mu, \gamma^5\right\} = 0\,, \tag{4.17}$$

leaves it invariant, and therefore obeys chiral symmetry. However, for $m > 0$ chiral symmetry is explicitly broken by the mass term which transforms under chiral rotation as

$$m\psi\,\overline{\psi} \to m\psi'\,\overline{\psi}' = m\psi\,\overline{\psi}\,e^{i2\alpha\gamma^5}\,. \tag{4.18}$$

The fermion fields of Lagrangians that obey chiral symmetry can be decomposed into uncoupled left- and right-handed fields which can be rotated independently

$$\begin{aligned} \psi_L \to \psi'_L = e^{i\alpha_L\gamma^5}\,\psi_L\,, \quad \psi_R \to \psi'_R = e^{i\alpha_R\gamma^5}\,\psi_R\,, \\ \overline{\psi}_L \to \overline{\psi}'_L = \overline{\psi}_L\,e^{i\alpha_L\gamma^5}\,, \quad \overline{\psi}_R \to \overline{\psi}'_R = \overline{\psi}_R\,e^{i\alpha_R\gamma^5}\,, \end{aligned} \tag{4.19}$$

where the left- and right-handed fields are defined by

$$\begin{aligned} \psi_L &= P_-\,\psi\,, \quad \psi_R = P_+\,\psi\,, \\ \overline{\psi}_L &= \overline{\psi}\,P_+\,, \quad \overline{\psi}_R = \overline{\psi}\,P_-\,. \end{aligned} \tag{4.20}$$

Here

$$P_{\pm} = \frac{1}{2}\left(1 \pm \gamma^5\right) , \tag{4.21}$$

are the chiral projection operators which have the properties

$$P_{\pm}^2 = P_{\pm} , \tag{4.22}$$
$$P_{\pm}\, P_{\mp} = 0 , \tag{4.23}$$
$$P_{\pm} + P_{\mp} = \mathbb{1} , \tag{4.24}$$
$$\gamma^{\mu}\, P_{\pm} = P_{\mp}\, \gamma^{\mu} . \tag{4.25}$$

Performing the decomposition

$$\begin{aligned} \mathcal{L}_{m=0} &= \overline{\psi}\, \not{D}\, \psi \\ &= \overline{\psi}\, (P_+ + P_-)\, \not{D}\, (P_+ + P_-)\, \psi \\ &= \overline{\psi}\, P_+\, \not{D}\, P_+\, \psi + \overline{\psi}\, P_+\, \not{D}\, P_-\, \psi + \overline{\psi}\, P_-\, \not{D}\, P_+\, \psi + \overline{\psi}\, P_-\, \not{D}\, P_-\, \psi \\ &= \overline{\psi}_L\, \not{D}\, \psi_L + \overline{\psi}_R\, \not{D}\, \psi_R , \end{aligned} \tag{4.26}$$

where we have used

$$P_{\pm}\, \not{D}\, P_{\pm} = \not{D}\, P_{\mp}\, P_{\pm} = 0 , \tag{4.27}$$

it is clear from Eq. (4.16) that the Lagrangian is invariant under independent rotation of the left- and right-handed sectors.

In fact, the third step of Eq. (4.16) demonstrates that the essence of chiral symmetry is encapsulated in the relation

$$\left\{ \not{D} , \gamma^5 \right\} \equiv \not{D}\gamma^5 + \gamma^5 \not{D} = 0 . \tag{4.28}$$

This is to say that a Dirac operator D which satisfies this relation obeys chiral symmetry. Extending this to the lattice, it is straightforward to see that the massless naive lattice Dirac operator satisfies this relation

$$\left\{ \not{\nabla} , \gamma^5 \right\} \equiv \nabla_{\mu}\gamma^{\mu}\gamma^5 + \gamma^5\gamma^{\mu}\nabla_{\mu} = 0 . \tag{4.29}$$

As is the case for the continuum Dirac operator, a nonzero mass term breaks the symmetry explicitly

$$\left\{ \not{\nabla} + m , \gamma^5 \right\} = \left\{ \not{\nabla} , \gamma^5 \right\} + \left\{ m , \gamma^5 \right\} = m\gamma^5 + \gamma^5 m = 2m\gamma^5 \neq 0 . \tag{4.30}$$

However, the Wilson Dirac operator does not satisfy chiral symmetry, even in the massless case, as the Wilson term breaks the symmetry explicitly

$$\left\{\not{\nabla} + \frac{ra}{2}\Delta\,,\gamma^5\right\} = \left\{\not{\nabla}\,,\gamma^5\right\} + \left\{\frac{ra}{2}\Delta\,,\gamma^5\right\} = \frac{ra}{2}\Delta\gamma^5 + \gamma^5\frac{ra}{2}\Delta = ra\gamma^5\Delta \neq 0\,. \quad (4.31)$$

This is not surprising since, as was shown in Section 4.2, the Wilson term has masslike behaviour. Nonetheless, the explicit breaking of chiral symmetry by the Wilson term is not ideal. However, as in the case of fermion doubling which led to the introduction of the Wilson term in the first place, the implementation of fermions on the lattice may, in principle, be modified, provided the correct theory is recovered in the continuum limit. The difficulty of this in practice, however, is elucidated by the Nielson-Ninomiya No-Go Theorem [15–17].

4.4 No-Go Theorem

Theorem (Nielson-Ninomiya No-Go Theorem)**.** *There does not exist a lattice Dirac operator* D_{lat} *which satisfies all of the following conditions:*

1. ***Correct limit:*** $\lim_{a\to 0} D_{\text{lat}} = \not{D}$*, where* D_μ *is the covariant derivative associated with a single fermion species with finite* $m \geq 0$*.*

2. ***Doubler-free:*** *Additional fermion species decouple in continuum limit.*

3. ***Locality:*** $\exists \;\; r\,,\, c\,,\, A \geq 0 \;\; s.t. \;\; |D_{\text{lat}}(x,y)| < Ae^{-cr} \;\; \forall \;\; |x-y| > r$

4. ***Chiral symmetry:*** $\{D_{\text{lat}}\,,\gamma^5\} = 0$ *for* $m = 0$

Within this framework, it is clear that the naive Dirac operator which has the correct limit, is local, and obeys chiral symmetry, necessarily violates the doubler-free condition. Furthermore, it is clear that to remove doublers it is necessary to sacrifice one of the other conditions, chiral symmetry in the case of the Wilson Dirac operator.

The No-Go Theorem presents a fundamental limitation to the realisation of chiral symmetry on the lattice and it was thought for some time that it may never be. This was until an explicit solution to the Ginsparg-Wilson relation was found, offering a lattice implementation of chiral symmetry.

4.5 Ginsparg-Wilson Relation

Whilst the No-Go Theorem precludes a local, doubler-free, lattice Dirac operator with the correct continuum limit from satisfying continuum chiral symmetry as encapsulated by Eq. (4.28), the Ginsparg-Wilson relation [18]

$$\left\{D_{\text{lat}}\,,\gamma^5\right\} = 2aD_{\text{lat}}\,\gamma^5\,D_{\text{lat}}\,, \tag{4.32}$$

where D_{lat} is a lattice Dirac operator, offers a lattice implementation of chiral symmetry which successfully navigates the limitations imposed by the No-Go Theorem. As shall be shown, the implementation of lattice chiral symmetry offered by the Ginsparg-Wilson relation not only has features analogous to those of the continuum, but recovers continuum chiral symmetry in the continuum limit. This is hinted at in the Ginsparg-Wilson relation itself which in the limit $a \to 0$ recovers Eq. (4.28).

To implement chiral symmetry on the lattice as defined by the Ginsparg-Wilson relation, the lattice chiral rotation must be defined such that any Ginsparg-Wilson Lagrangian (i.e. a lattice fermion Lagrangian that has a lattice Dirac operator that satisfies the Ginsparg-Wilson relation) remains invariant under lattice chiral rotation. Furthermore, it must recover the continuum transformations in the limit $a \to 0$. Defining the lattice chiral rotation as

$$\psi \to \psi' = \exp\left[i\alpha\gamma^5\left(1 - aD_{\text{lat}}\right)\right]\psi\,, \tag{4.33}$$

$$\overline{\psi} \to \overline{\psi}' = \overline{\psi}\exp\left[i\alpha\left(1 - aD_{\text{lat}}\right)\gamma^5\right]\,, \tag{4.34}$$

satisfies both conditions. It is straightforward to see that the continuum transformation of Eq. (4.13) is recovered in the limit $a \to 0$. Write the lattice chiral rotation for infinitesimal α as

$$\psi \to \psi' = \left[1 + i\alpha\gamma^5\left(1 - aD_{\text{lat}}\right)\right]\psi + \mathcal{O}(\alpha^2)\,, \tag{4.35}$$

$$\overline{\psi} \to \overline{\psi}' = \overline{\psi}\left[1 + i\alpha\left(1 - aD_{\text{lat}}\right)\gamma^5\right] + \mathcal{O}(\alpha^2)\,. \tag{4.36}$$

We then apply it to a Ginsparg-Wilson Lagrangian

$$\begin{aligned}
\mathcal{L} &= \overline{\psi} D_{\text{lat}} \psi \\
&\to \overline{\psi} \left[1 + i\alpha \left(1 - aD_{\text{lat}}\right) \gamma^5\right] D_{\text{lat}} \left[1 + i\alpha\gamma^5 \left(1 - aD_{\text{lat}}\right)\right] \psi + \mathcal{O}(\alpha^2) \\
&= \overline{\psi} D_{\text{lat}} \psi + i\alpha\overline{\psi} \left[\left(1 - aD_{\text{lat}}\right) \gamma^5 D_{\text{lat}} + D_{\text{lat}} \gamma^5 \left(1 - aD_{\text{lat}}\right)\right] \psi + \mathcal{O}(\alpha^2) \\
&= \overline{\psi} D_{\text{lat}} \psi \\
&= \mathcal{L} \,,
\end{aligned} \tag{4.37}$$

and use a rearranged form of the Ginsparg-Wilson relation

$$\left(1 - aD_{\text{lat}}\right) \gamma^5 D_{\text{lat}} + D_{\text{lat}} \gamma^5 \left(1 - aD_{\text{lat}}\right) = 0 \,, \tag{4.38}$$

to demonstrate its invariance under lattice chiral rotation.

Furthermore, to produce analogous features of continuum chiral symmetry on the lattice a Ginsparg-Wilson Lagrangian must be decomposable into left- and right-handed chiral sectors which can be rotated independently. Making the definition

$$\hat{\gamma}^5 = \gamma^5 \left(1 - 2aD_{\text{lat}}\right) \,, \tag{4.39}$$

lattice chiral projection operators analogous to those of the continuum can be constructed

$$\hat{P}_{\pm} = \frac{1}{2} \left(1 \pm \hat{\gamma}^5\right) \,. \tag{4.40}$$

The lattice chiral projection operators have almost all the properties of the continuum projectors, with

$$\hat{P}_{\pm}^2 = \hat{P}_{\pm} \,, \tag{4.41}$$

$$\hat{P}_{\pm} \, \hat{P}_{\mp} = 0 \,, \tag{4.42}$$

$$\hat{P}_{\pm} + \hat{P}_{\mp} = \mathbb{1} \,. \tag{4.43}$$

The continuum operators satisfy $\gamma^\mu \, P_{\pm} = P_{\mp} \, \gamma^\mu$, which is ultimately reflective of the defining relation of continuum chiral symmetry $\left\{\not{D} \,, \gamma^5\right\} = 0$ and implies $\not{D} \, P_{\mp} = P_{\pm} \, \not{D}$. The lattice chiral projection operators instead satisfy

$$D_{\text{lat}} \, \hat{P}_{\pm} = P_{\mp} \, D_{\text{lat}} \,, \tag{4.44}$$

which analogously reflects the defining relation of lattice chiral symmetry, the Ginsparg-Wilson relation. From the properties of the lattice chiral projection operators, the

following definitions of the left and right-handed fermion fields on the lattice can be made

$$\begin{aligned} \psi_L &= \hat{P}_- \, \psi \,, \quad \psi_R = \hat{P}_+ \, \psi \,, \\ \overline{\psi}_L &= \overline{\psi} \, P_+ \,, \quad \overline{\psi}_R = \overline{\psi} \, P_- \,. \end{aligned} \tag{4.45}$$

From these definitions a Ginsparg-Wilson Lagrangian can be decomposed into left- and right-handed fields in a manner analogous to continuum chiral symmetry

$$\begin{aligned} \mathcal{L}_{m=0} &= \overline{\psi} \, D_{\text{lat}} \, \psi \\ &= \overline{\psi} \, (P_+ + P_-) \, D_{\text{lat}} \left(\hat{P}_+ + \hat{P}_- \right) \psi \\ &= \overline{\psi} \, P_+ \, D_{\text{lat}} \, \hat{P}_+ \, \psi + \overline{\psi} \, P_+ \, D_{\text{lat}} \, \hat{P}_- \, \psi + \overline{\psi} \, P_- \, D_{\text{lat}} \, \hat{P}_+ \, \psi + \overline{\psi} \, P_- \, D_{\text{lat}} \, \hat{P}_- \, \psi \\ &= \overline{\psi}_L \, D_{\text{lat}} \, \psi_L + \overline{\psi}_R \, D_{\text{lat}} \, \psi_R \,, \end{aligned} \tag{4.46}$$

where we have used

$$P_\pm \, D_{\text{lat}} \, \hat{P}_\pm = P_\pm \, P_\mp \, D_{\text{lat}} = 0 \,. \tag{4.47}$$

Noting that in the continuum limit $a \to 0$, $\hat{\gamma}^5 \to \gamma^5$ and $\hat{P}_\pm \to P_\pm$, it can be shown that the above terms all recover their continuum counterparts. As such, it has been demonstrated that the Ginsparg-Wilson relation offers a lattice implementation of chiral symmetry which is analogous to that of the continuum, and recovers continuum chiral symmetry in the limit $a \to 0$.

4.6 Overlap Fermions

The overlap Dirac operator D_{o} [19–24], given by

$$D_{\text{o}} = \frac{1}{2a} \left(1 + \gamma^5 \, \epsilon \left[H \right] \right) \,, \tag{4.48}$$

where $\epsilon \left[H \right]$ is the matrix sign function applied to the kernel H, is a solution to the Ginsparg-Wilson relation. This is verified below,

$$\begin{aligned} 2a D_{\text{o}} \, \gamma^5 \, D_{\text{o}} &= 2a \, \frac{1}{2a} \left(1 + \gamma^5 \, \epsilon \left[H \right] \right) \, \gamma^5 \, \frac{1}{2a} \left(1 + \gamma^5 \, \epsilon \left[H \right] \right) \\ &= \frac{1}{2a} \left(1 + \gamma^5 + \gamma^5 \, \epsilon \left[H \right] \, \gamma^5 + \gamma^5 \, \gamma^5 \, \epsilon \left[H \right] + \gamma^5 \, \epsilon \left[H \right] \, \gamma^5 \, \gamma^5 \, \epsilon \left[H \right] \right) \\ &= \frac{1}{2a} \left(1 + \gamma^5 \, \epsilon \left[H \right] \right) \, \gamma^5 + \gamma^5 \, \frac{1}{2a} \left(1 + \gamma^5 \, \epsilon \left[H \right] \right) \\ &= D_{\text{o}} \, \gamma^5 + \gamma^5 \, D_{\text{o}} \\ &= \left\{ D_{\text{o}} \, , \, \gamma^5 \right\} \,. \end{aligned} \tag{4.49}$$

The overlap formulation provides an implementation of fermions which obey a lattice deformed chiral symmetry and is sensitive to the topological structures of the gauge field.

Typically, the kernel is chosen to be the Hermitian form of the Wilson Dirac operator

$$H = \gamma^5 D_{\mathrm{w}} = \gamma^5 \left(\not{\nabla} + \frac{ra}{2}\Delta + m_{\mathrm{w}} \right) , \tag{4.50}$$

where we have previously seen D_{w} in Eq. (4.10), but other choices are valid. In particular, the use of a kernel that incorporates smearing can have numerical advantages [25–31]. One such choice used extensively in this thesis is the Hermitian fat-link-irrelevant-clover (FLIC) fermion action $\gamma^5 D_{\mathrm{flic}}$ [25, 32] where

$$D_{\mathrm{flic}} = \not{\nabla} + \frac{a}{2}\left(\Delta^{\mathrm{fl}} - \frac{1}{2}\sigma \cdot F^{\mathrm{fl}} \right) + m_{\mathrm{w}} \, , \tag{4.51}$$

and the superscript fl denotes terms constructed from fat-links which have undergone four sweeps of stout-link smearing [33] at $\rho = 0.1$. The FLIC action is based on the clover fermion action [34]

$$D_{\mathrm{clover}} = \not{\nabla} + \frac{a}{2}\left(\Delta - \frac{1}{2} c_{\mathrm{sw}} \sigma \cdot F \right) + m_{\mathrm{w}} \, , \tag{4.52}$$

which introduces the clover term $\sigma \cdot F$ and clover coefficient c_{sw} to the Wilson action. The clover coefficient can be nonperturbatively tuned to remove $\mathcal{O}(a)$ errors, but this is not necessary when the clover action is used as the kernel of the overlap action which is automatically $\mathcal{O}(a)$-improved. The quark mass for Wilson-type fermions is usually specified by the hopping parameter

$$\kappa \equiv \frac{1}{8 + 2am_{\mathrm{w}}} \, . \tag{4.53}$$

However, when used as a matrix kernel in the context of the overlap action, the Wilson mass parameter m_{w} must be chosen to have a negative value in order to be in the topological region, with $am_{\mathrm{w}} = -1$ corresponding to $\kappa = \frac{1}{6}$ being the canonical value.

4.6.1 Locality Properties

Unlike the Wilson Dirac operator, the overlap Dirac operator is not *ultralocal*, which is to say

$$\nexists \;\; r \geq 0 \;\; \text{s.t.} \;\; |D_{\mathrm{o}}(x,y)| = 0 \;\; \forall \;\; |x-y| > r \, . \tag{4.54}$$

This arises from the inverse square-root in the matrix sign function. Fortunately, to recover locality in the continuum limit it is sufficient for a lattice Dirac operator to satisfy an *exponential* locality, which is to say

$$\exists \;\; r\,, \;\; c\,, \;\; A \geq 0 \;\; \text{s.t.} \;\; |D(x,y)| < Ae^{-cr} \;\; \forall \;\; |x-y| > r\,. \tag{4.55}$$

The overlap Dirac operator satisfies locality in this sense provided $H^2(-m)$ is bounded, and the lower bound, with the exception of isolated low-lying modes which can be projected out and dealt with explicitly, is well separated from zero.

Since all lattice Dirac operators are bounded from above, it is the lower limit which is of particular interest. With the assumption of a plaquette smoothness condition

$$||1 - P_{\mu\nu}(x)|| < \epsilon \;\; \forall \;\; x\,, \;\; \mu\,, \;\; \nu\,, \tag{4.56}$$

a lower bounds on $H_{\mathrm{w}}^2(-m)$ can be derived, where H_{w} is the Hermitian form of the Wilson Dirac operator [35, 36]. This guarantees the locality of the overlap Dirac operator when H_{w} is used as the matrix kernel.

4.6.2 Implementing the Overlap Operator

The primary hurdle to overcome in computing the overlap Dirac operator is evaluating the matrix sign function $\epsilon(H)$ which, defined formally via the spectral theorem, is given by

$$\epsilon(H) = \sum_i \mathrm{sign}\,(\lambda_i)\,|i\rangle\,\langle i|\;, \tag{4.57}$$

where λ_i are the eigenvalues of H. Computing the matrix sign function directly by diagonalisation is computationally intractable due to the large size of H. Instead, we can write the matrix sign function as

$$\epsilon(H) = \frac{H}{\sqrt{H^\dagger H}}\,, \tag{4.58}$$

which can be approximated by a rational polynomial. Throughout this work we use the Zolotarev optimal rational polynomial approximation [37, 38] which has the form

$$\epsilon(H) \approx d\frac{H}{|\lambda_{\min}|}\left(\frac{H^2}{\lambda_{\min}^2} + c_{2n}\right)\sum_{l=1}^{n}\frac{b_l}{\frac{H^2}{\lambda_{\min}^2} + c_{2l-1}}\,, \tag{4.59}$$

where the coefficients are given in Ref. [38] and is evaluated using an iterative multi-shift conjugate gradient solver [39]. This is nested, with a second level of the multi-

shift conjugate gradient solver enabling the computation of the overlap operator for multiple mass parameters μ, for the computational cost of only the lightest mass.

The condition number of H given by

$$\left|\frac{\lambda_{\max}}{\lambda_{\min}}\right| . \tag{4.60}$$

is related to both the number of polynomial terms and solver iterations (and therefore computational cost) necessary to achieve a desired precision. As $\lambda_{\max}$ is bounded from above, we project out the lowest-lying eigenmodes calculating them explicitly according to Eq. (4.57), such that the condition number of the reduced matrix which enters into the polynomial approximation, and by extension the computational efficiency, is greatly improved. This also has the added bonus of giving a much-improved estimator of the low modes.

The number of low-lying eigenmodes which are projected out and value of the hopping parameter may be chosen for optimal benefit.

Chapter 5

Overlap Quark Propagator

This chapter is based on A. Virgili, W. Kamleh and D. Leinweber, "Overlap quark propagator near the physical pion mass" [40].

The massive overlap Dirac operator [41] is defined as

$$D_o[\mu] = (1-\mu)D_o + \mu\,, \tag{5.1}$$

where $0 \leq \mu \leq 1$ is the overlap fermion mass parameter, related to the bare quark mass by

$$m_q = 2m_{\rm w}\,\mu\,. \tag{5.2}$$

The massive overlap quark propagator in coordinate space is given by

$$S(x,y) = \frac{1}{2m_{\rm w}(1-\mu)}\left(D_{\rm o}^{-1}[\mu](x,y) - \delta_{x,y}\right), \tag{5.3}$$

where colour and spinor indices have been suppressed. The subtraction of the contact term implies that the overlap propagator satisfies

$$\left\{\gamma_5\,, S\big|_{m_q=0}\right\} = 0, \tag{5.4}$$

mirroring the continuum chiral symmetry relation. After taking the colour trace and transforming to momentum space, the general form of the overlap quark propagator on the lattice can be written as

$$S(p) = \frac{Z(p)}{i\not{q} + M(p)}, \tag{5.5}$$

were $Z(p)$ is the renormalisation function and $M(p)$ is the mass function. The kinematical lattice momentum q_μ is defined by considering the tree-level propagator

$$S_{\rm tree}^{-1}(p) = i\not{q} + m_{\rm w}\,, \tag{5.6}$$

with the link variables set to unity, $U_\mu(x) = \mathbb{1} \;\; \forall \;\; x, \mu$. This is the only tree-level correction required for the overlap quark propagator. The simple form of Eq. (5.5) is afforded by the absence of additive renormalisation in the overlap formalism. Isolation of $M(p)$ and $Z(p)$ is straight forward. We can rewrite Eq. (5.5) as

$$\begin{aligned} S(p) &= \frac{-i\not{q}Z(p) + M(p)Z(p)}{q^2 + M^2(p)} \\ &\equiv -i\not{\mathcal{C}}(p) + \mathcal{B}(p), \end{aligned} \tag{5.7}$$

where we have defined

$$\mathcal{B}(p) \equiv \frac{1}{n_s n_c}\mathrm{Tr}\left[S(p)\right] = \frac{M(p)Z(p)}{q^2 + M^2(p)}\,, \tag{5.8}$$

$$\mathcal{C}_\mu(p) \equiv \frac{i}{n_s n_c}\mathrm{Tr}\left[\gamma_\mu S(p)\right] = \frac{q_\mu Z(p)}{q^2 + M^2(p)}\,, \tag{5.9}$$

and n_s and n_c are the respective extents of the spin and colour indices. Defining

$$\mathcal{A}(p) \equiv \frac{q\cdot\mathcal{C}}{q^2} = \frac{Z(p)}{q^2 + M^2(p)}\,, \tag{5.10}$$

the mass and renormalisation functions are calculated with the ratios

$$M(p) = \frac{\mathcal{B}(p)}{\mathcal{A}(p)}\,, \tag{5.11}$$

$$Z(p) = \frac{\mathcal{C}^2(p) + \mathcal{B}^2(p)}{\mathcal{A}(p)}\,. \tag{5.12}$$

5.1 Computing the Overlap Quark Propagator

Lattice QCD calculations can directly probe the structure of the nonperturbative quark propagator. The quark propagator in momentum space offers valuable insight into the two main features of nonperturbative low-energy QCD, namely confinement and dynamical chiral symmetry breaking.

Previous lattice studies of the quark propagator have utilised a range of fermion actions [2, 42–61]. In principle, calculations from all valid fermion actions should agree in the continuum limit. However, at finite lattice spacing the choice of discretisation does have significant implications.

Wilson-type fermions have been used to study the quark propagator [2, 42–45], including the twisted-mass variant [46,47]. However, there are associated difficulties, primarily stemming from the explicit breaking of chiral symmetry by the Wilson

term. This implies that the fermion propagator is not protected from additive mass renormalisation, and the extraction of the mass and renormalisation functions of the quark propagator is nontrivial. Whilst more straightforward 'additive' [44] and 'multiplicative' [45] tree-level correction methods work well within certain regimes, they run into issues. A more sophisticated 'hybrid' method resolves these, however at the expense of introducing ambiguities into the results [45].

A recent study [2] computed the quark propagator on a large-volume lattice with dynamical $\mathcal{O}(a)$-improved Wilson fermions for the first time. The study employed the hybrid tree-level correction method for the mass function and supplemented it with an H4-extrapolation [62, 63] for the renormalisation function. The nonmonotonic behaviour with a peak around $p \sim 3$ GeV observed in the renormalisation function [2] is a phenomenon previously unseen in quark propagator studies.

Studies using staggered fermions [48–51] benefit from being relatively inexpensive to simulate and maintaining a remnant of chiral symmetry, though the formulation is not without its own complications. In particular, the fermion doubling problem is not removed but only reduced, such that a number of additional fermion species, or *tastes*, remain.

Despite its significant computational cost, the overlap action has been used extensively in lattice studies of the quark propagator [52–59]. The advantage of the overlap lies not only in its superior chiral properties, but also the straightforward, prescribed manner in which the mass and renormalisation functions are extracted. The only tree-level correction necessary is to identify the kinematical momentum.

Given the different properties of the various fermion discretisations, it is of interest to compare quark propagator results obtained from the respective fermion actions. As such, we compute the overlap quark propagator and compare with existing results.

5.1.1 Simulation Parameters

We compute the overlap quark propagator on a $32^3 \times 64$ PACS-CS 2+1-flavour ensemble [64] at the lightest available dynamical quark mass, corresponding to a pion mass of $m_\pi = 156$ MeV. The lattice spacing $a = 0.0933$ fm is set by the Sömmer parameter $r_0 = 0.49$ fm, providing a spatial lattice volume of $\sim (3\text{ fm})^3$. These dynamical configurations were generated using a nonperturbatively-improved clover fermion action [34, 65] and an Iwasaki gauge action [66]. The domain-decomposed Hybrid Monte Carlo algorithm [67,68] with mass-preconditioning [69,70], chronological inversion [71], and deflation [72] was employed for the up and down quarks. For

the strange quarks Polynomial Hybrid Monte Carlo [73–77] with UV-filtering [78–81] was used. The molecular dynamics time was 990. The large volume of the configurations provides significant averaging over each configuration such that statistically accurate results are obtained on 30 gauge field configurations.

We employ the overlap fermion action at six values of the valence quark mass $m_q = 6$, 9, 19, 28, 56, 84 MeV where the lightest mass was tuned to match the pion mass of the ensemble. The FLIC fermion action in the kernel $H = \gamma^5 D_{\text{flic}}$ benefits from mean-field improvement [82] applied to the gauge links

$$U_\mu(x) \to \frac{U_\mu(x)}{u_0}\,, \tag{5.13}$$

where

$$u_0 = \left\langle \frac{1}{3}\,\text{Re}\,\text{Tr}\,[P_{\mu\nu}(x)] \right\rangle^{\frac{1}{4}}\,, \tag{5.14}$$

is the mean link, such that

$$D_{\text{flic}} = \not{\nabla}_{\text{mfi}} + \frac{a}{2}\left(\Delta^{\text{fl}}_{\text{mfi}} - \frac{1}{2}\sigma \cdot F^{\text{fl}}_{\text{mfi}}\right) + m_{\text{w}}\,. \tag{5.15}$$

For the applicable terms, mean-field improvement is applied to the fat-links. In obtaining a favourable condition number for the inversion, we set the Wilson mass parameter to $am_{\text{w}} = -1.1$ corresponding to a hopping parameter of $\kappa = 0.17241$ in the kernel. The evaluation of the inner conjugate gradient was accelerated by projecting out the 80 lowest-lying eigenmodes. Cylinder [83] and half cuts are applied to the propagator data. Uncertainties are estimated using second-order jackknife resampling.

Renormalisation Scale

The quark renormalisation function $Z(p)$ implicitly depends on the chosen renormalisation scale ζ. $Z(p)$ is determined by scaling the bare lattice renormalisation function in the MOM scheme [84] such that

$$Z(\zeta) = 1\,, \tag{5.16}$$

at the largest momentum considered, $\zeta = 6.8$ GeV. The mass function is independent of ζ.

Landau Gauge Fixing

The quark propagator is gauge dependent, and hence requires a choice of gauge fixing condition. Here we use the Landau gauge condition, which in the continuum is defined by $\partial_\mu A^\mu(x) = 0$. On the lattice, this condition is satisfied by finding the gauge transformation which maximises the $\mathcal{O}(a^2)$-improved functional [85]

$$\mathcal{F}_{\text{Imp}} = \frac{4}{3}\mathcal{F}_1 - \frac{1}{12u_0}\mathcal{F}_2\,, \tag{5.17}$$

where

$$\mathcal{F}_1 = \sum_{x,\mu} \frac{1}{2}\text{Tr}\left[U_\mu(x) + U_\mu^\dagger(x)\right]\,, \tag{5.18}$$

$$\mathcal{F}_2 = \sum_{x,\mu} \frac{1}{2}\text{Tr}\left[U_\mu(x)\,U_\mu(x+\hat{\mu}) + U_\mu^\dagger(x+\hat{\mu})\,U_\mu^\dagger(x)\right]\,. \tag{5.19}$$

The use of an improved gauge-fixing functional ensures $\mathcal{O}(a)$ improvement contained within the overlap formalism is realised in the results. We use the Fourier accelerated conjugate gradient method [86] to optimise Eq. (5.17).

5.1.2 Results

The mass and renormalisation functions $M(p)$ and $Z(p)$ for all bare quark masses considered are presented as functions of p on a linear scale in Figures 5.1 and 5.2, respectively. To resolve the infrared behaviour we also plot $M(p)$ and $Z(p)$ for all masses considered versus a log scale in Figures 5.3 and 5.4, respectively.

The mass function exhibits the expected qualitative features. Namely, we see agreement in the ultraviolet with the bare mass consistent with asymptotic freedom. The enhancement in the infrared is a clear signature of dynamical chiral symmetry breaking, with a generated constituent quark mass just below 400 MeV. The steadier drop-off of the mass function away from the peak with increasing p as compared to the results of Ref. [2] is consistent with previous overlap studies. The central values of the peak increase with decreasing bare mass, but is otherwise statistically consistent with no mass dependence.

In fact, if we examine the mass function plotted against a log scale in Figure 5.3, we are able to see signs of a plateau at small momenta as has been suggested elsewhere [87, 88]. This is more clear at heavier quark masses. Within statistical errors the level of the plateau is independent of the valence quark mass. This

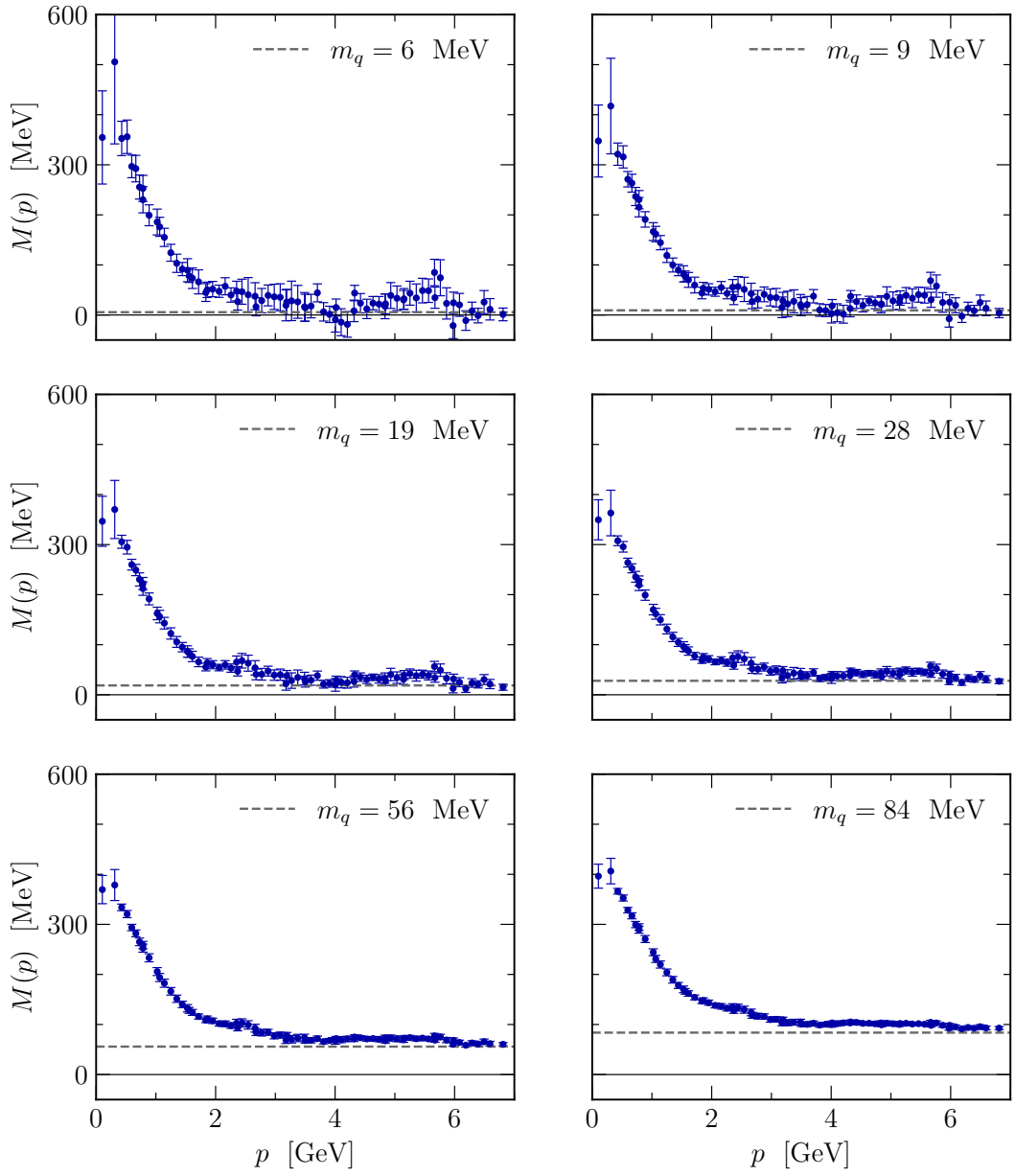

Figure 5.1: Mass function $M(p)$ for all bare quark masses m_q considered with p on a linear scale.

suggests the behaviour may be determined by the sea quarks which in the hybrid setup used herein are treated by the nonperturbatively-improved clover action.

Future studies which are able to more effectively probe the low-momentum behaviour by gaining access to additional data points in the deep infrared region and closer to $p = 0$ through the use of larger volumes or twisted boundary conditions would be of interest to confirm the behaviour observed herein.

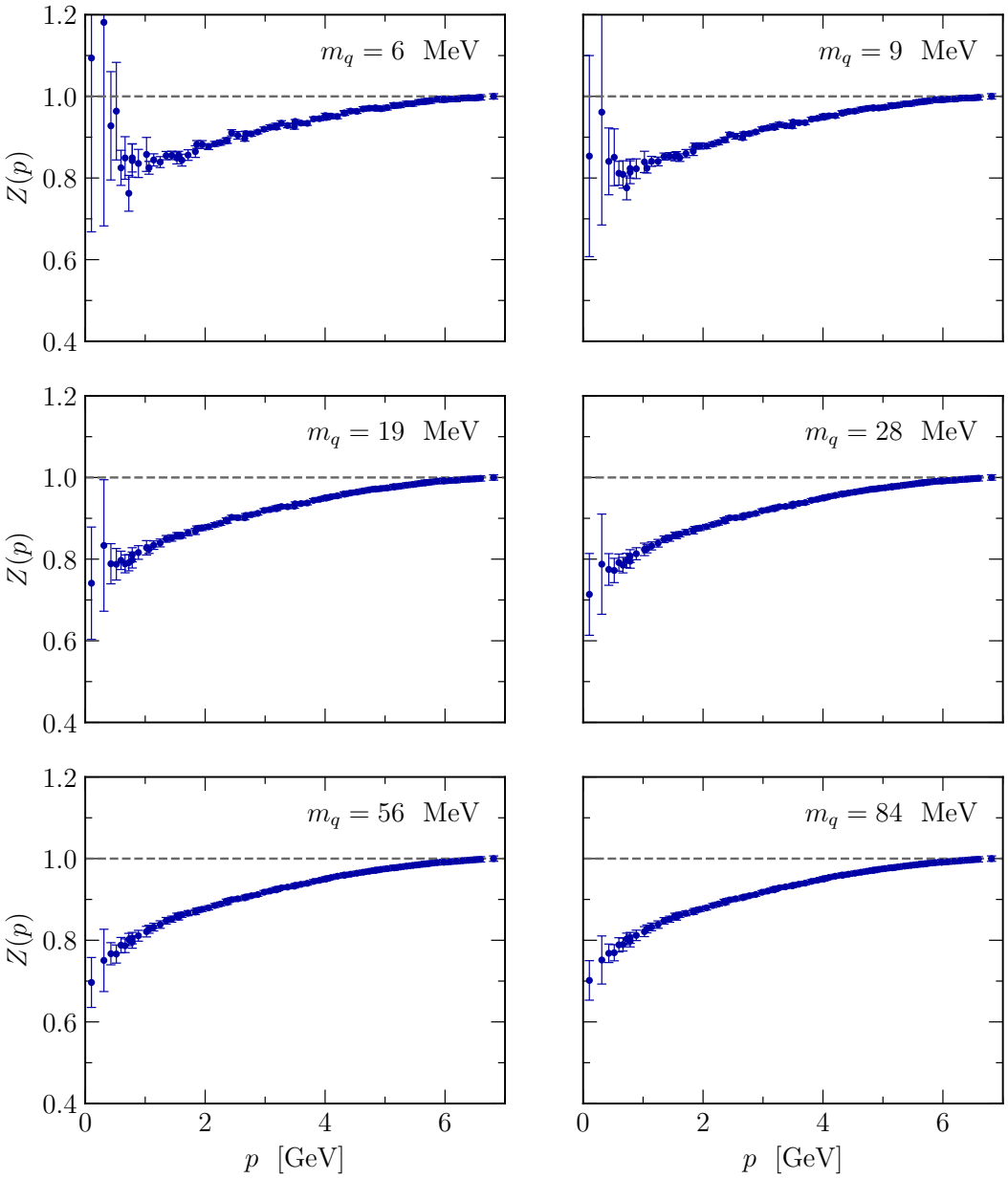

Figure 5.2: Renormalisation function $Z(p)$ for all bare quark masses m_q considered with p on a linear scale.

The renormalisation functions shown in Figure 5.2 are consistent with the tree-level value at large momenta as expected. Within statistical errors, $Z(p)$ is monotonically decreasing with p for the 4 heaviest bare masses considered. For the lightest masses the picture is less clear. The log scale in Figure 5.4 enables the resolution of some fluctuations in the small momenta region. At the lightest masses there appears to be an uptick in the central values in the deep infrared, albeit with very large statistical errors. A low-lying point at $p \sim 0.75$ GeV suggests the possibility

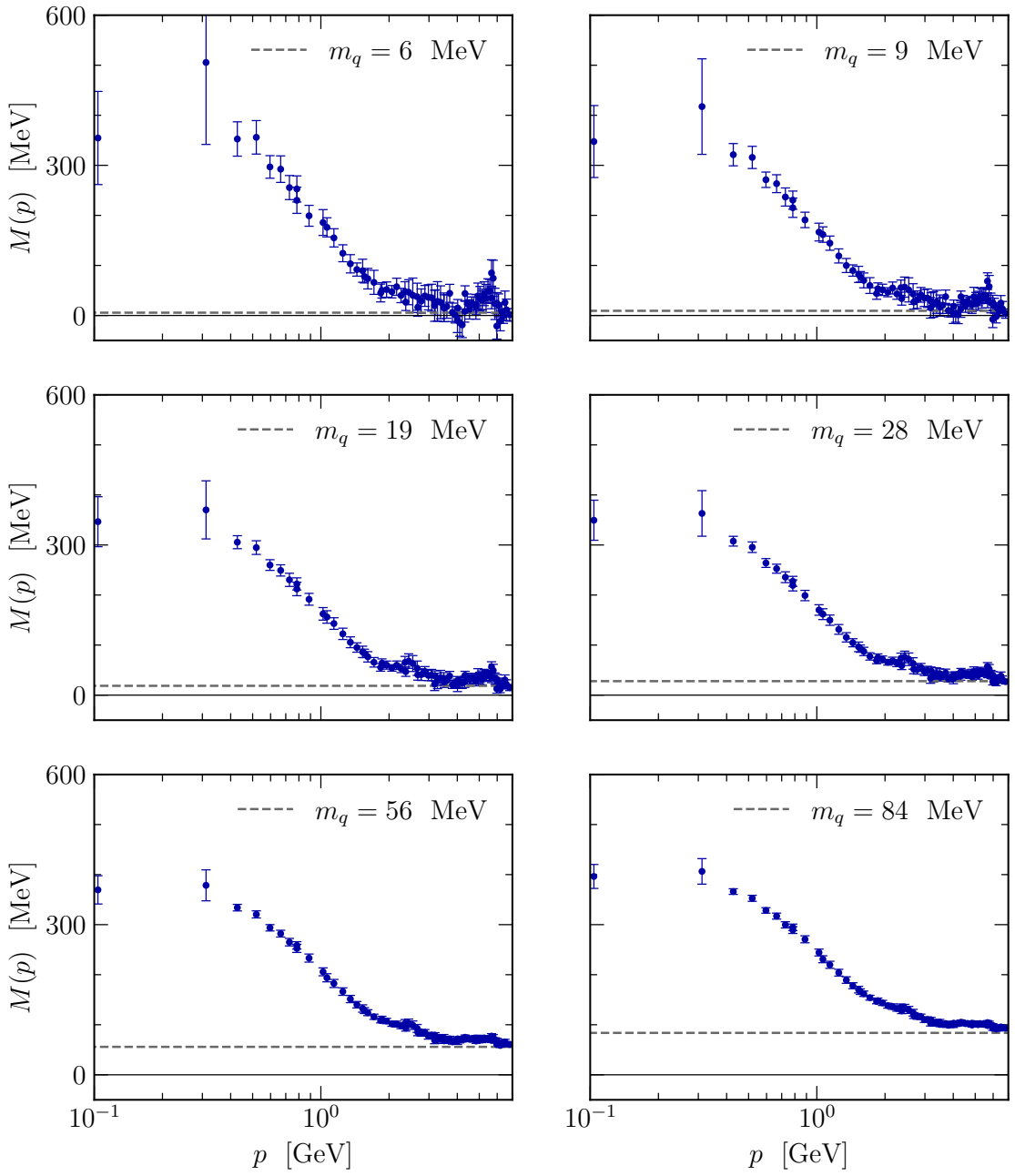

Figure 5.3: Mass function $M(p)$ for all bare quark masses m_q considered with p on a log scale.

of a minimum for $Z(p)$ in the $p = 0.5$–1 GeV region. This would be consistent with Schwinger-Dyson results which reported a minimum for $Z(p)$ in quenched calculations at light quark masses [89–91].

Otherwise, there is a weak mass dependence in the infrared suppression of $Z(p)$, which becomes slightly more prominent at heavier quark masses. This is in contrast to the findings of Ref. [2] which found increasing infrared suppression with decreasing

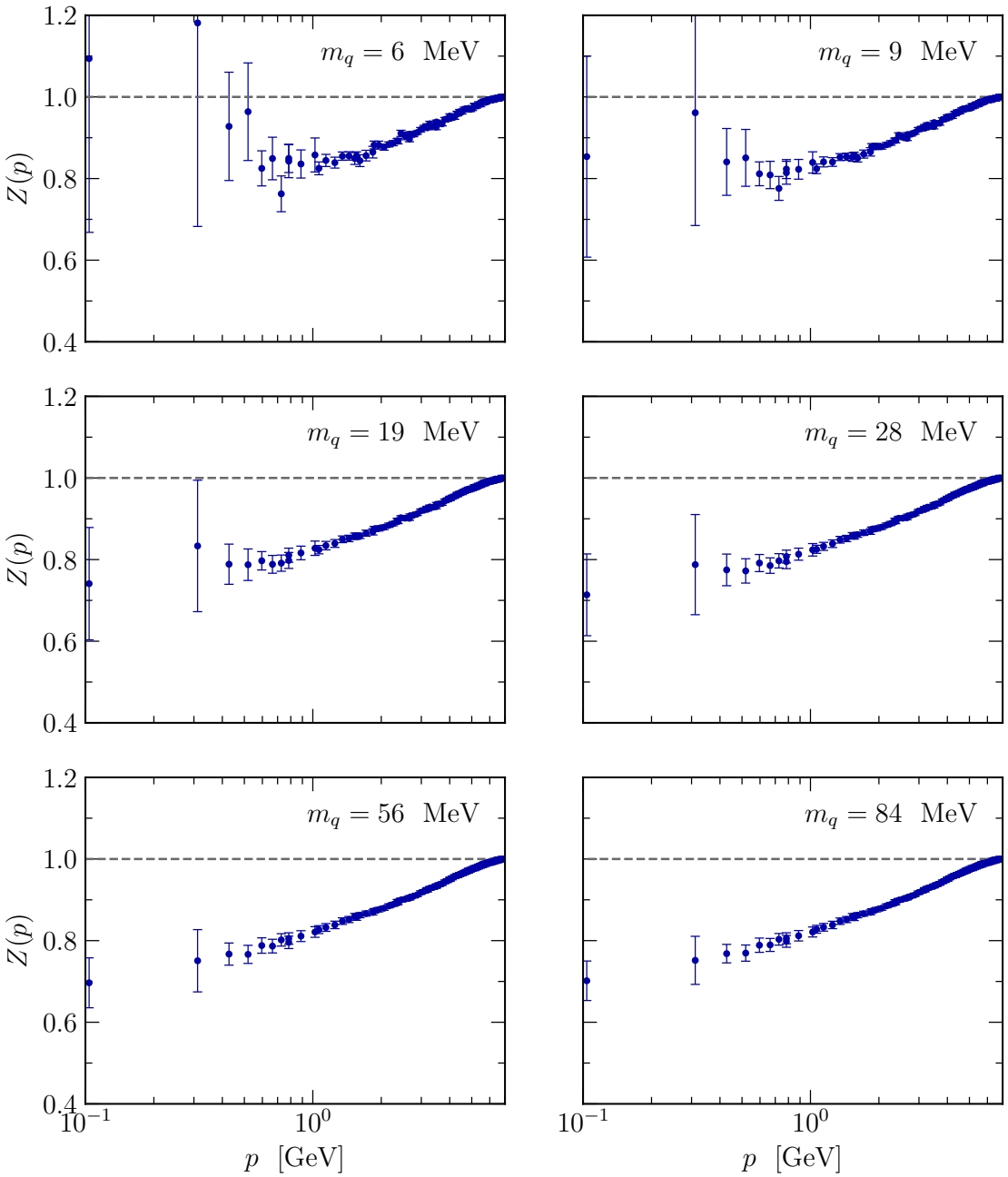

Figure 5.4: Renormalisation function $Z(p)$ for all bare quark masses m_q considered with p on a log scale.

quark mass. Furthermore, Ref. [2] observed a peak in the renormalisation function in the region of 3 GeV. This seems to be a peculiarity of Wilson fermions, and is not seen in our results or studies using other discretisations.

5.2 Summary

The Landau-gauge overlap quark propagator has been calculated on a 2+1-flavour gauge ensemble with light dynamical quarks near the physical pion mass for the first time. The signature of dynamical chiral symmetry breaking is clearly seen in the infrared enhancement of the mass function. Hints of a plateau in $M(p)$ at small momenta can be resolved when plotted on a log scale. The level of the plateau is statistically independent of the quark mass suggesting its behaviour is determined by the sea quarks, which are treated with the nonperturbatively-improved clover action.

The behaviour of the renormalisation function is consistent with previous smaller-volume studies using overlap fermions. The advantage of using a chiral fermion action to study the quark propagator is made clear with the observation that $Z(p)$ monotonically decreases with p (up to statistical fluctuations in the far infrared at the lightest masses considered). The uptick of the central values within these fluctuations and low-lying point around $p \sim 0.75$ GeV are suggestive of a minimum in the $p = 0.5$–1 GeV regions, consistent with Refs. [89–91]. These observations are in contrast to a previous calculation [2] that explored the Wilson fermion propagator with dynamical quarks on a large-volume lattice and found nonmonotonic behaviour in the renormalisation function for $p > 1$ GeV with a maximum around $p = 3$ GeV, and monotonically decreasing behaviour for $p < 1$.

Future investigations using even larger volume lattices, or twisted boundary conditions, would provide access to smaller nontrivial momenta, enabling a better resolution of the infrared behaviour of the mass and renormalisation functions. These results can inform theoretical formalisms that depend on knowledge of the fundamental propagators of QCD constituents [92–97]. Of course, it is desirable to seek an understanding of the nonperturbative properties of the quark propagator by examining the features of the QCD ground-state vacuum fields that give rise to these phenomena. In particular, the role of topologically-motivated degrees of freedom [98] such as centre vortices [99] are of contemporary interest.

Chapter 6

Roper Resonance

This chapter is based on A. Virgili, W. Kamleh and D. Leinweber, "Role of chiral symmetry in the nucleon excitation spectrum" [100].

The true nature of the Roper resonance ($N(1440)\frac{1}{2}^+ P_{11}$), the first positive-parity excited state of the nucleon discovered in 1964 via a partial-wave analysis of pion-nucleon scattering data [101], is a long standing source of debate. The puzzlement surrounding the Roper resonance arises from the discrepancy between the level ordering predicted by otherwise successful quark model calculations, and the energy of the resonance observed in nature. With an energy of 1440 MeV the Roper resonance is the lowest-lying resonance in the nucleon spectrum, sitting even below the first negative-parity excitation, the ($N(1535)\frac{1}{2}^- S_{11}$) state. This is a reversal of the ordering predicted by simple quark models, which place the energy of the positive-parity P_{11} state well above that of the negative-parity S_{11} state.

This apparent discrepancy persists in lattice QCD calculations, with the majority of lattice calculations obtaining an energy level for the first positive-parity nucleon excitation that sits high relative to that expected for the Roper resonance, even near the physical quark mass regime [102–111]. The exception to this is the χQCD Collaboration, which using overlap fermions in combination with the sequential empirical Bayes (SEB) analysis method [112] were able to find a low-lying positive-parity excited state on the lattice with an energy that in the chiral limit is consistent with the Roper resonance in nature [3, 113].

It is clear that some controversy persists regarding how the Roper resonance in the continuum manifests on the lattice [114–121]. The χQCD Collaboration advocates that their result is directly associated with the use of overlap fermions and stresses the importance of implementing exact chiral symmetry when investigating the nucleon spectrum. They motivate this by pointing towards the success of chiral soliton models, based on spontaneous chiral symmetry breaking, predicting the or-

dering of the Roper resonance and S_{11} state observed in nature and the contrasting failure of various, otherwise successful quark models, to do the same [3, 122].

Furthermore, motivated by the increased coupling of the overlap action to ghost states in the quenched approximation, it has been postulated the overlap action may provide better access to pion-nucleon physics on the lattice [113]. On the other hand, even in the absence of a low-lying lattice energy level, it has been shown using effective field theory that it is possible to reconcile the lattice Wilson-type results with experiment by describing the infinite-volume Roper as a resonance generated dynamically through strongly coupled meson-baryon channels [104, 123].

In light of these differing perspectives, it is important and of interest to perform a systematic investigation of the role of chiral symmetry in the nucleon spectrum [124]. In this chapter we directly compare results obtained from simulations employing the overlap and clover fermion actions, respectively. To ensure that any discrepancies between the respective simulations are entirely attributable to the choice of fermion action, both simulations are performed on the same set of gauge field configurations, at matched pion masses, and analysed utilising identical correlation matrix techniques.

Calculations are performed at three values of the valence quark mass. The lattice energies of the ground and first positive-parity excited state are computed for each action from variational analyses, additionally yielding effective mass and eigenstate projected correlation functions which are also compared. Our final analysis avoids the selection of fit regimes, instead presenting the lattice results directly.

6.1 Methodology

6.1.1 Resonance Physics from Lattice QCD

The determination of resonance properties from lattice QCD calculations requires a comprehensive understanding of the spectrum of excited states in the finite periodic volume of the lattice. In principle, this spectrum includes all single, hybrid, and multiparticle contributions having the quantum numbers of the resonance of interest. This finite-volume spectrum then forms the input to the Lüscher method [125] or its generalisations [104, 123, 126, 127] which relate the finite-volume energy levels to infinite-volume momentum-dependent scattering amplitudes. The application of these methods is a necessary step in connecting lattice QCD results to the properties of resonances measured in experiment.

Obtaining an accurate determination of the finite-volume nucleon spectrum is challenging, requiring an extensive set of baryon interpolating fields and robust correlation function analysis techniques. Many collaborations have explored the spectrum excited by local single-particle operators [102–110], and hybrid nucleon interpolators have been investigated in Ref. [111] where additional states were found in the spectrum. Nonlocal multiparticle interpolating fields are necessary to determine the lattice energy eigenstates to the level of accuracy that is required to implement the Lüscher formalism and compare lattice QCD results to experiment. The main approach has been to bring experimental results to the finite volume of the lattice [104, 123]. It is only recently that the first applications of the Lüscher formalism to the baryon sector have emerged [128, 129].

In this work, our focus is on the finite-volume spectrum and its dependence on the choice of fermion action. We consider quasilocal operators as these are sufficient to address this issue. We acknowledge that these localised operators do not have good overlap with multiparticle scattering states and as such the energies obtained in our calculations may contain contributions from more than one energy eigenstate of QCD. The single-state ansatz of Ref. [105] used herein minimises this effect, which can shift the observed energies within the width of the associated resonance. Moreover, we note that this subtle issue of state mixing applies to both fermion actions. Any differences which exist between the actions will be apparent in the results presented, preserving our ability to search for a nontrivial role for chiral symmetry in the nucleon spectrum.

6.1.2 Fermion Actions

Nucleon spectroscopy on the lattice is typically performed using Wilson-type fermions, with the clover [34] and twisted-mass [130] variants the most commonly used today. Due to the presence of the matrix sign function, simulations which implement the overlap formalism are of the order of 100 times more computationally expensive than those which use Wilson-type fermions. Consequently, it is far more common to employ Wilson-type fermions in a hadron spectrum calculation, where the explicit breaking of chiral symmetry on the lattice is expected to have negligible impact. However, one cannot immediately dismiss the possible role that the fermion action might play in examining the nucleon excitation spectrum. It is known that the coupling of interpolation fields to lattice hadron states is action dependent, so it may be the case that a low-lying Roper-like state couples strongly with the overlap action but weakly with Wilson-type actions.

The nonperturbatively-improved clover action has been used extensively in previous studies of the nucleon excitation spectrum. For this reason we choose to use this form of Wilson-type fermions for our comparison with the overlap action. From Section 4.6, the clover Dirac operator is given by

$$D_{\text{clover}} = \nabla\!\!\!/ + \frac{a}{2}\left(\Delta - \frac{1}{2}c_{\text{sw}}\sigma\cdot F\right) + m_{\text{w}}\,. \tag{4.52}$$

6.1.3 Correlation Matrix Techniques

Previous studies by the χQCD Collaboration [3,113] obtained the nucleon excitation spectrum from overlap fermions with the SEB method [112]. The majority of results from other groups use a variational analysis. Here, we use the same correlation matrix method to extract the nucleon excitation spectrum for each respective action. We do this to eliminate any other potential dependencies and perform a direct comparison of the results obtained from the respective clover and overlap fermion actions.

Variational correlation matrix techniques [131,132] are well-established methods for successfully producing hadron spectra from correlation functions [133]. First, a basis of N operators is chosen such that any states of interest are contained within the span. An $N \times N$ matrix of cross-correlation functions,

$$\mathcal{G}_{ij}(\vec{p},t) = \sum_{\vec{x}} \mathrm{e}^{-i\vec{p}\cdot\vec{x}} \left\langle\, \Omega \,\middle|\, \chi_i(\vec{x},t)\,\overline{\chi}_j(\vec{0},t_{src}) \,\middle|\, \Omega \,\right\rangle, \tag{6.1}$$

is constructed, where $\overline{\chi}_j$ and χ_i are the creation and annihilation operators of the interpolating fields, respectively. The parity projection operator

$$\Gamma_{\pm} = \frac{1}{2}\left(\gamma_0 \pm \mathbb{1}\right)\,, \tag{6.2}$$

projects out definite parity at $\vec{p} = \vec{0}$. Defining $G_{ij}(\vec{p},\,t) = \mathrm{Tr}\left[\Gamma\,\mathcal{G}_{ij}(\vec{p},\,t)\right]$, we can write the Dirac-traced correlation function as a sum of exponentials,

$$G_{ij}(t) = \sum_{\alpha} \lambda_i^{\alpha}\,\bar{\lambda}_j^{\alpha}\,\mathrm{e}^{-m_\alpha t}\,, \tag{6.3}$$

where λ_i^{α} and $\bar{\lambda}_j^{\alpha}$ are the couplings of χ_i and $\overline{\chi}_j$ at the sink and source respectively, and m_α is the mass of the αth energy eigenstate. We search for a linear combination of operators

$$\bar{\phi}^{\alpha} = \bar{\chi}_j\,u_j^{\alpha} \qquad \text{and} \qquad \phi^{\alpha} = \chi_i\,v_i^{\alpha}\,, \tag{6.4}$$

such that ϕ and $\bar{\phi}$ ideally couple to a single energy eigenstate. In practice, the energies observed in lattice QCD calculations can be contaminated with states not captured by the spanned basis. To minimise this effect, improved analysis techniques have been developed [105]. From Eq. (6.3) we see that

$$G_{ij}(t_0 + dt)\, u_j^\alpha = \mathrm{e}^{-m_\alpha dt}\, G_{ij}(t_0)\, u_j^\alpha \,, \tag{6.5}$$

and note that we can now find u_j^α and v_i^α for a given choice of variational parameters (t_0, dt) by solving

$$\left[G^{-1}(t_0)\, G(t_0 + dt)\right]_{ij} u_j^\alpha = c^\alpha\, u_i^\alpha \,, \tag{6.6}$$

and

$$v_i^\alpha \left[G(t_0 + dt)\, G^{-1}(t_0)\right]_{ij} = c^\alpha\, v_j^\alpha \,, \tag{6.7}$$

the left- and right-handed eigenvalue equations with eigenvalue $c^\alpha = \mathrm{e}^{-m_\alpha dt}$. G_{ij} is symmetric in the ensemble average so the improved estimator $\frac{1}{2}\left(G_{ij} + G_{ji}\right)$ is employed to ensure the left-handed and right-handed eigenvalues match. As G_{ij} is diagonalised by $u_j^\alpha$and v_i^α at t_0 and $t_0 + dt$ it is possible to write the eigenstate-projected correlation function as

$$G^\alpha(t) = v_i^\alpha\, G_{ij}(t)\, u_j^\alpha \,. \tag{6.8}$$

To extract eigenstate masses, we construct the effective mass function

$$M_{\mathrm{eff}}^\alpha(t) = \ln\left(\frac{G^\alpha(t)}{G^\alpha(t+1)}\right) , \tag{6.9}$$

and apply standard analysis techniques outlined in Ref. [134].

6.2 Results

6.2.1 Simulation Parameters

Computations are performed on a $32^3 \times 64$ PACS-CS 2+1-flavour ensemble [64] at $\kappa = 0.13754$ providing a lattice spacing of $a = 0.0961$ fm and a sea quark mass corresponding to $m_\pi^2 = 0.1506(9)$ GeV^2 in the Sömmer scale with $r_0 = 0.49$ fm. The clover and overlap calculations employ identical sets of 100 configurations.

Table 6.1: Matched pion masses for the clover and overlap actions.

Overlap		Clover	
μ	m_π/GeV	κ	m_π/GeV
0.0628	0.4347(32)	0.13742726	0.4349(43)
0.1205	0.5776(30)	0.13703168	0.5769(40)
0.1815	0.6980(31)	0.13661366	0.6987(40)

Antiperiodic boundary conditions in time are applied for both actions. An operator basis is constructed for each action using 16, 35, 100, and 200 sweeps of Gaussian smearing [135] at the source and sink with smearing parameter $\alpha = 0.7$.

We select input parameters which minimise the computational cost of evaluating the matrix sign function of the overlap kernel $\epsilon(H)$, where $H \equiv \gamma_5 D_{\text{flic}}$. In contrast to Chapter 5, we do not employ mean-field improvement and D_{flic} takes the form of Eq. (4.51). The Wilson term and clover links benefit from four sweeps of stout-link smearing at $\rho = 0.1$. The Wilson mass parameter is set to $am_{\text{w}} = -1.1$, corresponding to a hopping parameter value of $\kappa = 0.17241$ in the kernel. The evaluation of the inner conjugate gradient is accelerated by projecting out the subspace corresponding to the 80 lowest-lying eigenmodes of the overlap kernel and evaluating the sign function explicitly. Overlap propagators are calculated at three values of the overlap mass parameter $\mu = 0.0628,\ 0.1205$, and 0.1815, corresponding to pion masses of $m_\pi = 0.4347(32),\ 0.5776(30)$, and $0.6980(31)$ GeV respectively. We note the lightest mass is similar to that considered in Ref. [113].

We compute the pion correlation functions for each action with 100 sweeps of source and sink smearing. To ensure the pion masses of the respective actions match, we tune the clover hopping parameter by performing a linear fit to the square of the pion mass as a function of $1/\kappa$. Solving for the κ values corresponding to the overlap pion masses, we obtain $\kappa = 0.13742726,\ 0.13703168$, and 0.13661366. The clover coefficient takes its nonperturbative value of $c_{\text{sw}} = 1.715$. Running the clover simulation with these tuned input parameters, we obtain pion masses which closely match those of the overlap simulation. Masses for both actions are presented in Table 6.1.

While the pion masses are carefully matched, both lattice fermion actions have $\mathcal{O}(a^2)$ errors that will lead to small discrepancies in the nucleon mass spectrum. However, these differences are small relative to the 300 MeV differences discussed in Ref. [113].

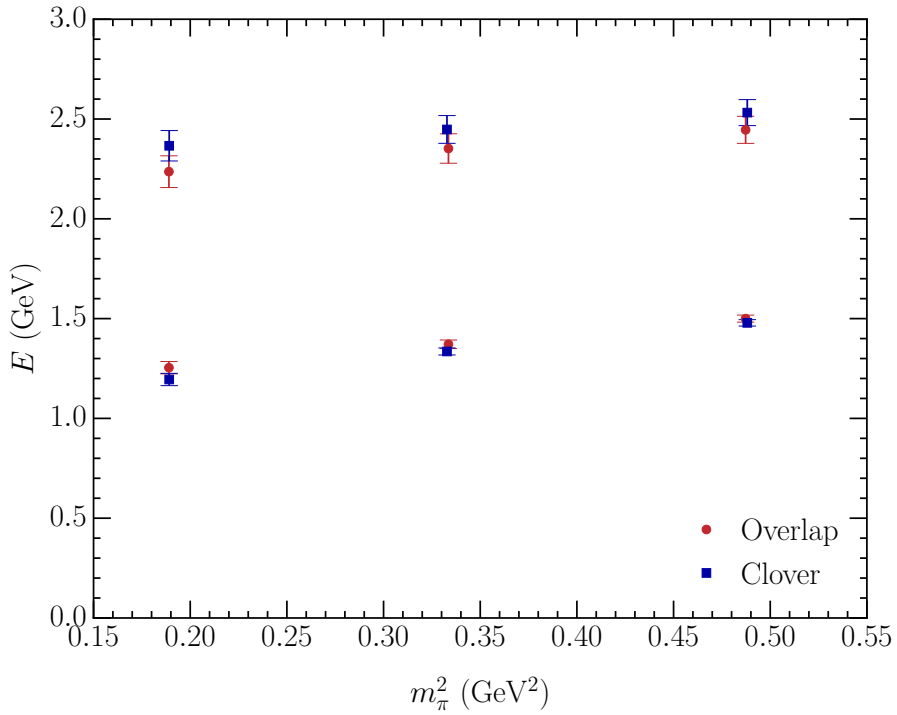

Figure 6.1: Nucleon ground and first-excited state masses for clover (blue, square) and overlap (red, circle) actions as a function of m_π^2.

6.2.2 Correlation Matrix Analyses

For our comparison, we employ the correlation matrix techniques discussed in Section 6.1.3. As we are only concerned with the ground state and first positive-parity excited state, we construct a 4×4 correlation matrix from our operator basis of source/sink Gaussian smearing ($N_{sm} = 16$, 35, 100, 200) and select $t_0 = 1$ relative to the source at $t_s = 0$ and $dt = 3$. Standard analysis techniques [134] provide the results reported in Table 6.2 and plotted in Figure 6.1. All corresponding clover and overlap nucleon ground and first excited state masses are in statistical agreement. The small systematic differences are likely associated with the aforementioned $\mathcal{O}(a^2)$ errors in the fermion action.

These results are dependent on specific choices for the variational parameters and fit windows. To make our results more robust we investigate further, initially avoiding the selection of fit windows. Here we compare the eigenstate projected effective mass and correlation functions for each action. Specifically, we compare how the first excited state compares to the ground state for each action without fits. We do this in two ways.

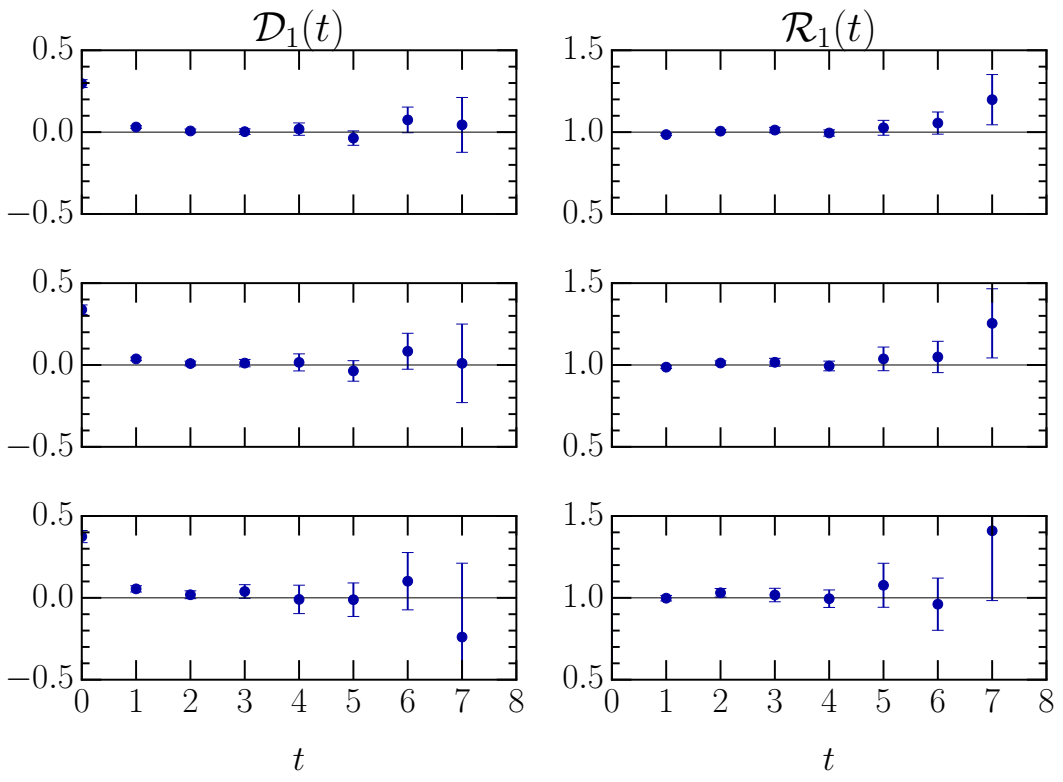

Figure 6.2: $\mathcal{D}_1(t)$ in units of GeV (left) and $\mathcal{R}_1(t)$ (right) for three different valence quark masses with heaviest $\mu = 0.1815$, $\kappa = 0.13661366$ (top), $\mu = 0.1205$, $\kappa = 0.13703168$ (middle), and lightest $\mu = 0.0628$, $\kappa = 0.13742726$ (bottom), for variational parameters $t_0 = 1$, $t = t_0 + dt = 4$.

First, we consider the effective mass functions obtained from the eigenstate projected correlators as in Eq. (6.9). We then take the ratio

$$R_{\alpha/0}(t) = M^{\alpha}_{\text{eff}}(t)/M^{0}_{\text{eff}}(t)\,, \tag{6.10}$$

for each action, where M^0_{eff} and M^α_{eff} are the ground and αth excited state effective mass functions. This scales the excited state mass function for each action in terms of their respective ground states, eliminating any differences which arise from ground state discrepancies and placing the focus on the excitation energy. To compare the actions we take the ratio

$$\mathcal{R}_{\alpha}(t) = \frac{R^{\text{clover}}_{\alpha/0}(t)}{R^{\text{overlap}}_{\alpha/0}(t)}\,. \tag{6.11}$$

As a second point of comparison, we consider the eigenstate projected correlation functions directly. We take the ratio

$$G_{\alpha/0}(t) = G^{\alpha}(t)/G^{0}(t)\,, \tag{6.12}$$

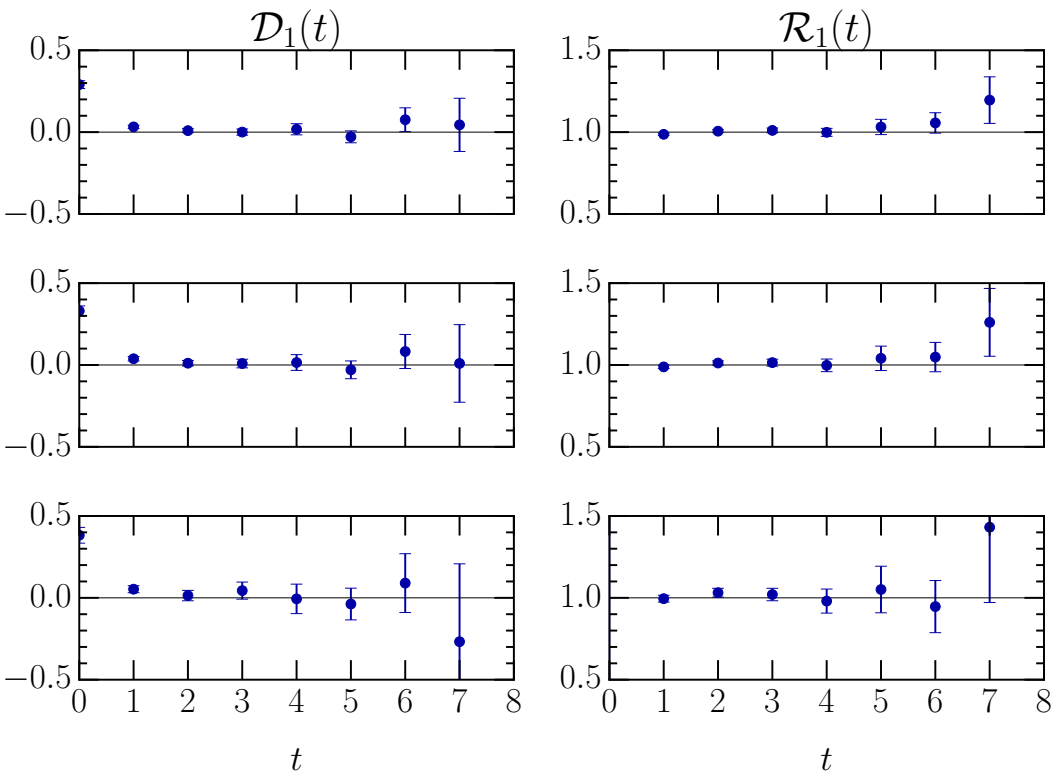

Figure 6.3: $\mathcal{D}_1(t)$ in units of GeV (left) and $\mathcal{R}_1(t)$ (right) for three different valence quark masses with heaviest $\mu = 0.1815$, $\kappa = 0.13661366$ (top), $\mu = 0.1205$, $\kappa = 0.13703168$ (middle), and lightest $\mu = 0.0628$, $\kappa = 0.13742726$ (bottom), for variational parameters $t_0 = 2$, $t = t_0 + dt = 5$.

for each action, where G^0 and G^α are the ground and αth excited state projected correlation functions. We construct the effective mass splitting

$$\Delta M^\alpha_{\text{eff}}(t) = \ln\left(\frac{G_{\alpha/0}(t)}{G_{\alpha/0}(t+1)}\right), \tag{6.13}$$

corresponding to the mass splitting of the αth excited state and the ground state for each action, respectively. Taking the difference

$$\mathcal{D}_\alpha(t) = \Delta M^{\alpha,\text{clover}}_{\text{eff}}(t) - \Delta M^{\alpha,\text{overlap}}_{\text{eff}}(t)\,, \tag{6.14}$$

we obtain the difference between the mass splittings produced by each action.

Both $\mathcal{D}_1(t)$ and $\mathcal{R}_1(t)$ are plotted in Figure 6.2 for each mass regime. We note that $\mathcal{D}_\alpha(t) = 0$ or $\mathcal{R}_\alpha(t) = 1$ correspond to no difference in the excitation energies produced by the clover and overlap fermion actions.

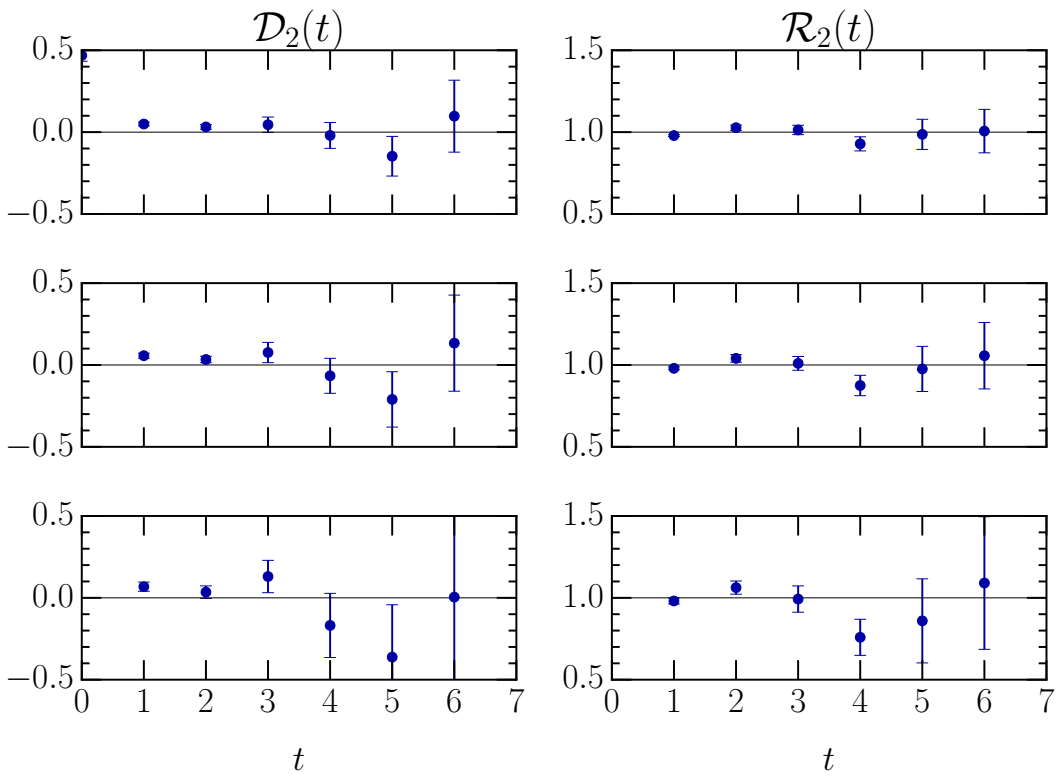

Figure 6.4: $\mathcal{D}_2(t)$ in units of GeV (left) and $\mathcal{R}_2(t)$ (right) for three different valence quark masses with heaviest $\mu = 0.1815$, $\kappa = 0.13661366$ (top), $\mu = 0.1205$, $\kappa = 0.13703168$ (middle), and lightest $\mu = 0.0628$, $\kappa = 0.13742726$ (bottom), for variational parameters $t_0 = 1$, $t = t_0 + dt = 4$.

It is important to demonstrate that these highly correlated ratios and differences can be described with the full covariance matrix $\chi^2/\text{d.o.f.} \approx 1$. Hence, we evaluate the agreement of the difference $\mathcal{D}_1(t)$ and the ratio $\mathcal{R}_1(t)$ with the constants zero and one, respectively. The reduced χ^2 values of each fit with $2 \leqslant t \leqslant 6$ are reported in Table 6.3. These values confirm there is negligible difference between the clover and overlap actions with respect to the nucleon spectrum, and show no evidence for the existence of a low-lying lattice excited state.

The next step in our comprehensive analysis is to explore other variational parameters t_0 and dt. Systematic errors in the correlation matrix analysis enter as $\mathcal{O}\left(e^{-(E_{N+1}-E_N)t}\right)$ for an $N \times N$ correlation matrix. To this end we require a large $t = t_0 + dt$. However, we also require a small t_0 to ensure statistically accurate information is captured from excited state contributions before they are Euclidean-time suppressed. Table 6.4 presents the $\chi^2/\text{d.o.f.}$ values for the results discussed in Table 6.3, this time focusing on the lightest quark mass, closest to the sea quark mass. Again, analyses of $\mathcal{D}_1(t) = 0$ and $\mathcal{R}_1(t) = 1$ return acceptable $\chi^2/\text{d.o.f.}$ values.

Table 6.2: Masses in GeV of the ground state and the first positive-parity excited state for the clover and overlap actions at the three valence quark masses considered.

	Overlap	Clover
Ground State	1.254(31)	1.195(31)
	1.371(21)	1.335(18)
	1.500(18)	1.479(16)
First Excited State	2.236(79)	2.366(76)
	2.352(74)	2.448(70)
	2.446(68)	2.532(65)

Table 6.3: χ^2/d.o.f. for $\mathcal{D}_1(t)$ fitted to the constant 0 and $\mathcal{R}_1(t)$ fitted to the constant 1, for each quark mass regime with $2 \leqslant t \leqslant 6$.

		χ^2/d.o.f.	
μ	κ	$\mathcal{D}_1(t)$	$\mathcal{R}_1(t)$
0.0628	0.13742726	0.619	1.002
0.1205	0.13703168	0.595	0.850
0.1815	0.13661366	0.842	0.757

Figure 6.3 displays results corresponding to Figure 6.2, this time for the variational parameters $t_0 = 2$, $dt = 3$.

Finally, we consider the second excited state. The energy of the second excited state is $\sim$3 GeV [102]. With the limited number of configurations the correlation functions decay to noise rapidly with our $a = 0.0961$ fm lattice spacing. Nonetheless, a solution of the generalised eigenvalue problem is found for variational parameters $t_0 = 1$, $dt = 3$ and results for $\mathcal{D}_2(t)$ and $\mathcal{R}_2(t)$ are presented in Figure 6.4. These results are similar to those presented for $\mathcal{D}_1(t)$ and $\mathcal{R}_1(t)$. While the statistical fluctuations are notably larger, there is no evidence of a significant difference between the fermion actions.

6.3 Summary

In this chapter, the role of chiral symmetry in the nucleon excitation spectrum was systematically examined. Results obtained from simulations employing nonchiral clover fermions and chiral overlap fermions were compared. To ensure that any observed differences or discrepancies in the results are attributable to the choice of

Table 6.4: χ^2/d.o.f. for $\mathcal{D}_1(t) = 0$ and $\mathcal{R}_1(t) = 1$, for the lightest quark mass considered with variational parameters t_0 and $t = t_0 + dt$ relative to the source at $t_s = 0$.

		χ^2/d.o.f.	
t_0	t	$\mathcal{D}_1(t)$	$\mathcal{R}_1(t)$
1	4	0.619	1.002
1	5	0.493	0.930
2	4	0.816	0.962
2	5	0.528	0.843

action the simulations were performed on the same set of gauge field configurations at three matched pion masses.

All corresponding clover and overlap nucleon ground and first excited state masses are in statistical agreement. Further analysis was conducted, showing that the ratios of the first excited and ground state effective mass functions and mass splittings are the same for each action.

The results show a remarkable level of agreement between the clover and overlap actions. Hence, we do not find any evidence supporting the claim that chiral symmetry plays a significant role in understanding the Roper resonance on the lattice.

Chapter 7

Smoothing Centre Vortices

This chapter is based on A. Virgili, W. Kamleh and D. Leinweber, "Smoothing algorithms for projected center-vortex gauge fields" [136].

7.1 Centre Vortices on the Lattice

On the lattice, centre vortices are revealed by projecting each gauge link to an element of the centre $\mathrm{Z}(N)$ of $\mathrm{SU}(N)$ where

$$\begin{aligned} \mathrm{Z}(N) &\equiv \{g \in \mathrm{SU}(N) \,|\, gh = hg \;\; \forall \;\; h \in \mathrm{SU}(N)\} \\ &= \{e^{i2\pi n/N}\mathbb{1} \,|\, n \in \mathbb{Z}_N\}\,, \end{aligned} \tag{7.1}$$

is the set of elements in $\mathrm{SU}(N)$ which commute with every other element of the group.

To obtain the centre-projected links, the gauge field is first fixed to maximal-centre gauge (MCG) by choosing the gauge transform $U_\mu(x) \to U^G_\mu(x)$ which maximises the functional [137]

$$\sum_{x,\mu} \left|\mathrm{Tr}\, U^G_\mu(x)\right|^2 , \tag{7.2}$$

as outlined in Refs. [4, 138, 139]. Each link is then projected to the nearest element of $\mathrm{Z}(N)$, such that for $N = 3$

$$U^G_\mu(x) \to \mathcal{P}_{\mathrm{Z}(3)}\left\{U^G_\mu(x)\right\} \equiv Z_\mu(x) = e^{i\frac{2\pi}{3}n_\mu(x)}\mathbb{1}\,, \tag{7.3}$$

where

$$n_\mu(x) = \begin{cases} 0, \;\text{if}\; \arg \mathrm{Tr}\, U^G_\mu(x) \in \left(-\frac{\pi}{3}\,, +\frac{\pi}{3}\right) , \\ +1, \;\text{if}\; \arg \mathrm{Tr}\, U^G_\mu(x) \in \left(+\frac{\pi}{3}\,, +\pi\right) , \\ -1, \;\text{if}\; \arg \mathrm{Tr}\, U^G_\mu(x) \in \left(-\pi\,, -\frac{\pi}{3}\right) . \end{cases} \tag{7.4}$$

The projected links $Z_\mu(x)$ define a vortex-only configuration in MCG. Centre vortices are identified by the vortex flux through each vortex-projected plaquette, where

$$\begin{aligned} P_{\mu\nu}(x) &= Z_\mu(x)\, Z_\nu(x+\hat{\mu})\, Z_\mu^\dagger(x+\hat{\nu})\, Z_\nu^\dagger(x) \\ &= e^{i\frac{2\pi}{3}p_{\mu\nu}(x)}\mathbb{1}\,, \end{aligned} \tag{7.5}$$

corresponds to a vortex flux value $p_{\mu\nu}(x) \in \{-1, 0, 1\}$. A plaquette with vortex flux $p_{\mu\nu}(x) = \pm 1$ is identified as pierced by a vortex with centre charge ± 1.

A vortex-removed link $U_\mu^{\mathrm{VR}}(x)$ is simply the product of the MCG-fixed link and the inverse of its centre-projected link, given by

$$U_\mu^{\mathrm{VR}}(x) = Z_\mu^\dagger(x)\, U_\mu^G(x)\,. \tag{7.6}$$

The vortex-removed links $U_\mu^{\mathrm{VR}}(x)$ define a vortex-removed configuration in MCG. Throughout this thesis we refer to the original SU(3) gauge fields as *untouched*. Whilst this approach is ad-hoc, in principle we could imagine vortex-modification as an operator applied to the underlying path-integral description of the untouched gauge fields. We do not know of such an operator but conceptually it would be motivated by something analogous to the 't Hooft loop operators of Ref. [140].

Composed only of links which are elements of Z(3), projected centre-vortex gauge fields are rough, and naturally, violate the smoothness condition of the overlap Dirac operator [25, 35, 36, 141]. See Subsection 4.6.1 for a more detailed discussion. As such, the vortex field must be smoothed. Previous pure-gauge centre-vortex studies using overlap fermions [99, 142] have employed cooling to this end. Whilst cooling suffices for vortex fields derived from pure-gauge backgrounds, it is not ideal for smoothing fields derived from dynamical backgrounds. In the dynamical case, an ideal smoothing algorithm would not only be analytical, but also preserve the underlying vortex structure. The constrained cooling algorithm [143] gives an example of the importance of structure-preserving smoothing.

Whilst there has been a successful, novel approach to smoothing Z(2) centre-vortex gauge fields [144], this has not been generalised to Z(3). As such, this work focuses on applying existing SU(3) gauge field smoothing algorithms to Z(3) centre-vortex gauge fields, with the goal of smoothing the vortex field such that the smoothness condition of the overlap Dirac operator is satisfied.

7.2 Analytic Smoothing

When smoothing Monte Carlo generated gauge fields, the use of analytic smoothing methods is inherently desirable. There are a number of such methods, the most commonly used being stout-link smearing [33] and the related gradient flow [145, 146]. Through the use of a unitary projection method, it is also possible to apply APE-style blocking techniques whilst preserving analyticity [147]. The differentiability of such smoothing methods is advantageous as they can be applied within the molecular dynamics integration component of the Hybrid Monte Carlo algorithm [147,148]. More importantly in the context of this work, the use of an analytic smoothing process implies that there is a parameterisable path within the gauge manifold that connects the original gauge links with the smoothed links.

The full SU(3) gauge group is described by 8 real parameters, whereas the centre group Z(3) consists of 3 discrete elements. The discrete nature of the centre group presents significant challenges when attempting to apply standard smoothing techniques, as we demonstrate below. First we define a quantity which is relevant to all the methods considered herein, namely the sum of the *staples* orthogonal to a link $U_\mu(x)$,

$$\Sigma_\mu(x) = \sum_{\nu\neq\mu} \left[U_\nu(x)\, U_\mu(x+\hat{\nu})\, U_\nu^\dagger(x+\hat{\mu}) + U_\nu^\dagger(x-\hat{\nu})\, U_\mu(x-\hat{\nu})\, U_\nu(x-\hat{\nu}+\hat{\mu}) \right] . \tag{7.7}$$

Related to the above, we also introduce the sum of the corresponding plaquettes (by closing the path of the staples via link multiplication) as

$$\Omega_\mu(x) = \Sigma_\mu(x)\, U_\mu^\dagger(x) . \tag{7.8}$$

7.2.1 Stout-Link Smearing

Stout-link smearing [33] provides the simplest case to show the difficulties of analytic smearing of centre-vortex projected fields. A single iteration of stout-link smearing with isotropic smearing parameter ρ is defined by

$$\tilde{U}_\mu(x) = \exp\left(\rho\, Q_\mu(x)\right) U_\mu(x), \tag{7.9}$$

where $Q_\mu(x)$ is the traceless anti-Hermitian projection of $\Omega_\mu(x)$ onto the Lie algebra $\mathfrak{su}(3)$,

$$Q_\mu(x) = \frac{1}{2}\left[\Omega_\mu(x) - \Omega_\mu^\dagger(x)\right] - \frac{1}{6}\mathrm{Tr}\left[\Omega_\mu(x) - \Omega_\mu^\dagger(x)\right] . \tag{7.10}$$

In the case of a vortex field, as each of the centre elements $Z_\mu(x) \propto \mathbb{1}$ is proportional to the identity matrix, we can parameterise any sum of vortex link paths as $re^{i\theta}\mathbb{1}$ where $r, \theta \in \mathbb{R}$. Consequently, we have

$$\begin{aligned} Q_\mu(x) &= \frac{1}{2}\left[re^{i\theta} - re^{-i\theta}\right]\mathbb{1} - \frac{1}{6}\mathrm{Tr}\left[(re^{i\theta} - re^{-i\theta})\mathbb{1}\right]\mathbb{1} \\ &= 0. \end{aligned} \tag{7.11}$$

As $Q_\mu(x)$ vanishes when derived from a centre-vortex field, it immediately follows from Eq. 7.9 that $\tilde{U}_\mu(x) = Z_\mu(x)$. That is, stout-link smearing leaves the vortex field unchanged. This result remains true in the presence of a gauge transformation $G(x)$. In general

$$\Sigma_\mu(x) \to \Sigma_\mu^G(x) = G(x)\,\Sigma_\mu(x)\,G^\dagger(x+\hat{\mu})\,, \tag{7.12}$$

$$\Omega_\mu(x) \to \Omega_\mu^G(x) = G(x)\,\Omega_\mu(x)\,G^\dagger(x)\,. \tag{7.13}$$

In the case of a vortex field, as the centre group commutes, by definition, with all elements of SU(3), we have

$$\Omega_\mu^G(x) = re^{i\theta}\,G(x)\,G^\dagger(x) = re^{i\theta}\mathbb{1}\,, \tag{7.14}$$

proving that a gauge-transformed centre-vortex field is also invariant under stout-link smearing.

7.2.2 Gradient Flow

The gradient flow [145, 146] is defined by the equations

$$\frac{d}{d\tau}U_\mu(x;\tau) = Q_\mu(x)[U(\tau)]\,U_\mu(x;\tau)\,, \tag{7.15}$$

$$U_\mu(x;0) = U_\mu(x)\,, \tag{7.16}$$

where τ is dimensionless *flow time* and $Q_\mu(x)[U(\tau)] \in \mathfrak{su}(3)$ is the generator of the infinitesimal field transformation

$$U \to U + \epsilon\,Q(U)\,U + \mathcal{O}(\epsilon^2)\,. \tag{7.17}$$

In particular, the *Wilson flow* is generated by

$$Q_\mu(x)[U] = T^a \, \partial^a_{x,\mu} \sum_{x,\mu\neq\nu} \mathrm{Tr}\left[P_{\mu\nu}(x)[U]\right] , \tag{7.18}$$

where T^a are the generators of SU(3) (see Appendix A.3) and

$$\partial^a_{x,\mu} f(U) = \frac{d}{ds} f(e^{sX^a} U)\bigg|_{s=0} , \tag{7.19}$$

$$X^a(y,\nu) = \begin{cases} T^a \text{ if } (y,\nu) = (x,\mu) \\ 0 \text{ otherwise.} \end{cases} \tag{7.20}$$

The explicit formula for the generator $Q_\mu(x)[U]$ is identical to that for stout-link smearing given in Eq. 7.10. In fact, noting that

$$\lim_{n\to\infty} (\mathbb{1} + \epsilon\, Q)^n \, U = \exp(\epsilon\, Q)\, U \tag{7.21}$$

we can map $\epsilon \to \rho$ and see that the stout-smeared link is the finite transformation generated by the Wilson flow process for sufficiently small smearing parameters.

It trivially follows that for a centre-vortex field $U_\mu(x;0) = Z_\mu(x)$ we have

$$\frac{d}{d\tau} U_\mu(x;\tau) = 0 \quad \forall \quad x, \quad \mu, \quad \tau \, . \tag{7.22}$$

Hence, independent of the initial gauge or the integration method, the Wilson flow of a centre vortex gauge field is invariant.

7.2.3 APE Smearing With Analytic Projection

We now consider APE smearing [149, 150] with the analytic projection method defined in Ref. [147], which we refer to as *unit-circle projection*. The APE smearing process starts with a blocking step, where the original link $U_\mu(x)$ is mixed with the sum of the staples in proportion to the smearing parameter α to define the blocked matrix

$$V\left[U_\mu(x)\right] \equiv V_\mu(x) = (1-\alpha)\, U_\mu(x) + \frac{\alpha}{6}\, \Sigma_\mu(x) \, . \tag{7.23}$$

This construction of $V_\mu(x)$ is gauge equivariant, which is to say, under a gauge transformation

$$U_\mu(x) \to U^G_\mu(x) = G(x)\, U_\mu(x)\, G^\dagger(x+\hat{\mu}) \, , \tag{7.24}$$

that

$$V\left[U_\mu^G(x)\right] = G(x)\,V\left[U_\mu(x)\right]\,G^\dagger(x+\hat{\mu})\,. \tag{7.25}$$

Setting $U_\mu^{(0)}(x) = U_\mu(x)$, the APE smearing update is then defined by

$$U_\mu^{(n)}(x) \to U_\mu^{(n+1)}(x) = \mathcal{P}\left\{V_\mu^{(n)}(x)\right\}\,, \tag{7.26}$$

where the blocked matrix $V_\mu^{(n)}(x) \equiv V[U_\mu^{(n)}(x)] \notin \mathrm{SU}(3)$ must be returned back to the gauge group. This may be performed in an analytic manner by first performing a unitary projection,

$$W_\mu(x) = V_\mu(x)\,\frac{1}{\sqrt{V_\mu^\dagger(x)\,V_\mu(x)}}\,, \tag{7.27}$$

such that the eigenvalues of W lie on the unit circle. The final step in the unit-circle projection is multiplying by the appropriate phase in order to return to SU(3),

$$\mathcal{P}_{\mathrm{ucp}}\left\{V_\mu(x)\right\} = \frac{1}{\sqrt[3]{\det W_\mu(x)}}\,W_\mu(x)\,. \tag{7.28}$$

As shown in Ref. [147], the unit-circle projection is gauge equivariant such that the smeared links share the same gauge transformation properties as the original link,

$$U_\mu^{(n)}(x) \to G(x)\,U_\mu^{(n)}(x)\,G^\dagger(x+\hat{\mu}). \tag{7.29}$$

In standard APE smearing, the staples term $\Sigma_\mu(x)$ is defined as per equation (7.7), but other choices are possible, in particular the over-improvement formalism [151–153] outlined in Eq. (7.53). For the purposes of the following discussion, we generalise $\Sigma_\mu(x)$ to sum over any combination of operators constructed from paths originating at lattice site x and terminating at $x+\hat{\mu}$.

When APE smearing is applied to a centre-vortex gauge field in arbitrary gauge (noting that $Z_\mu(x) \propto \mathbb{1}$), we can use gauge equivariance to write

$$V_\mu^{(0)}(x) = re^{i\theta}\,G(x)\,G^\dagger(x+\hat{\mu})\,. \tag{7.30}$$

Applying the unitary projection in Eq. (7.27) gives

$$\begin{aligned} W_\mu(x) &= re^{i\theta}\,G(x)\,G^\dagger(x+\hat{\mu})\,\frac{\mathbb{1}}{\sqrt{r^2}} \\ &= e^{i\theta}\,G(x)\,G^\dagger(x+\hat{\mu})\,. \end{aligned} \tag{7.31}$$

Noting that $\det W_\mu(x) = e^{i3\theta}$, we have that

$$\sqrt[3]{\det W_\mu(x)} = e^{i\left(\theta + \frac{2k\pi}{3}\right)}\,, \tag{7.32}$$

where $k \in \{0, 1, 2\}$ is chosen to correspond to the principal cube root, i.e. such that

$$-\frac{\pi}{3} < \theta + \frac{2k\pi}{3} < \frac{\pi}{3}\,. \tag{7.33}$$

Hence, the projected link is given by

$$\begin{aligned} Z^{(1)}_\mu(x) &= \frac{1}{e^{i\left(\theta + \frac{2k\pi}{3}\right)}}\, e^{i\theta}\, G(x)\, G^\dagger(x + \hat{\mu}) \\ &= e^{-i\frac{2k\pi}{3}}\, G(x)\, G^\dagger(x + \hat{\mu})\,, \end{aligned} \tag{7.34}$$

where $e^{-i\frac{2k\pi}{3}}\mathbb{1} \in \mathrm{Z}(3)$.

The key result here is that it is only possible to project to another element of Z(3). That is, applying APE smearing with unit-circle projection to a vortex link results in either the original link remaining unchanged, or updated to a different centre element thereby radically altering the vortex structure such that it no longer resembles its original form. As the method is gauge equivariant, this is true regardless of whether we are in maximal-centre gauge or not.

7.3 Update-Based Smoothing

Having determined that none of the analytic smearing techniques considered above can smoothly deform a vortex field away from the centre group, we consider an nonanalytic alternative. Specifically, we examine APE-style blocking coupled with the update-based reuniterisation method maximising the real part of the trace (MaxReTr) of the plaquette. This process is based on the Cabibbo-Marinari pseudo-heat-bath algorithm [154] which iteratively updates a candidate $\mathrm{SU}(N)$ matrix $U_\mu(x)$ to maximise the following,

$$\max \mathrm{Re}\,\mathrm{Tr}\left[U_\mu(x)\, V^\dagger_\mu(x)\right], \tag{7.35}$$

where $V_\mu(x)$ is the sum of link paths defined in Eq. (7.23). MaxReTr reuniterisation is fundamentally connected with cooling [152], as if we set the smearing fraction $\alpha = 1$, then we have $V_\mu(x) \propto \Sigma_\mu(x)$ and then the MaxReTr update selects the link

which minimises the local action in a way which does not depend on the original link.

Due to the nonanalytic nature of the MaxReTr update process, it is able to shift the vortex fields away from the centre group in a way that the differentiable smoothing methods above cannot. It will prove useful to review the specific details of the MaxReTr method as applied to SU(3), which involves iterating over SU(2) subgroups in order to achieve the optimisation specified by Eq. (7.35). First, define the matrix L^1 by

$$L^1 = U_\mu(x)\, V_\mu^\dagger(x)\,. \tag{7.36}$$

From L^1, another matrix, $T_1 \in \mathrm{SU}(2) \subset \mathrm{SU}(3)$, given by

$$T_1 = \frac{1}{2}\begin{bmatrix} L^1_{11} + (L^1_{22})^* & L^1_{12} - (L^1_{21})^* & 0 \\ L^1_{21} - (L^1_{12})^* & (L^1_{11})^* + L^1_{22} & 0 \\ 0 & 0 & 2 \end{bmatrix}, \tag{7.37}$$

is constructed, where L^1_{ij} is element (i,j) of L^1. Setting $k = \sqrt{\det T_1}$, this matrix is cooled such that

$$\left[T_1^c\right]_{2\times 2} = \frac{1}{k}\left[T_1^\dagger\right]_{2\times 2} \in \mathrm{SU}(2)\,, \tag{7.38}$$

within the embedded 2×2 subgroup, and the full matrix T_1^c is the embedding of the resulting submatrix into SU(3). The original link is then updated by

$$U_\mu(x) \to U'_\mu(x) = T_1^c\, U_\mu(x)\,, \tag{7.39}$$

This process is typically repeated for the other two diagonal SU(2) subgroups which together comprehensively cover SU(3), such that

$$L^2 = U'_\mu(x)\, V_\mu^\dagger(x) = T_1^c\, U_\mu(x)\, V_\mu^\dagger(x)\,, \tag{7.40}$$

$$L^3 = U''_\mu(x)\, V_\mu^\dagger(x) = T_2^c\, T_1^c\, U_\mu(x)\, V_\mu^\dagger(x)\,, \tag{7.41}$$

and

$$T_2 = \frac{1}{2}\begin{bmatrix} 2 & 0 & 0 \\ 0 & L^2_{22} + (L^2_{33})^* & L^2_{23} - (L^2_{32})^* \\ 0 & L^2_{32} - (L^2_{23})^* & (L^2_{22})^* + L^2_{33} \end{bmatrix}, \tag{7.42}$$

$$T_3 = \frac{1}{2}\begin{bmatrix} L^3_{11} + (L^3_{33})^* & 0 & L^3_{13} - (L^3_{31})^* \\ 0 & 2 & 0 \\ L^3_{31} - (L^3_{13})^* & 0 & (L^3_{11})^* + L^3_{33} \end{bmatrix}. \tag{7.43}$$

The updated link $U_\mu^{(1)}(x)$ after one loop over the SU(2) subgroups is given by

$$T_3^c\, T_2^c\, T_1^c\, U_\mu(x)\,. \tag{7.44}$$

In principle, one loop over the subgroups is considered sufficient for approaching the maximum defined by Eq. (7.35). Here we choose to perform three iterations over the subgroups as multiple loops provide an advantage in converging to the optimal link [152].

Let us now explore how the MaxReTr reuniterisation algorithm applies to a centre-vortex gauge field which has undergone an arbitrary gauge transformation

$$Z_\mu(x) \to G(x)\, Z_\mu(x)\, G^\dagger(x+\hat{\mu})\,. \tag{7.45}$$

Using the gauge equivariance of $V_\mu(x)$, L^1 has the gauge invariant form

$$\begin{aligned} L^1 &= G(x)\, Z_\mu(x)\, G^\dagger(x+\hat{\mu})\, G(x+\hat{\mu})\, V_\mu^\dagger(x)\, G^\dagger(x) \\ &= G(x)\, r e^{i\left(\frac{2\pi n}{3}-\theta\right)}\, G^\dagger(x) \\ &\equiv r e^{i\phi}\, \mathbb{1}\,, \end{aligned} \tag{7.46}$$

where $V_\mu(x) = re^{i\theta}$ is in MCG and we have defined $\phi \equiv \frac{2\pi n}{3} - \theta$ for $Z_\mu(x) = e^{i\frac{2\pi n}{3}}\,\mathbb{1}$ also in MCG. Hence, T_1 is given by

$$\begin{aligned} T_1 &= \frac{1}{2}\begin{bmatrix} r(e^{i\phi}+e^{-i\phi}) & 0 & 0 \\ 0 & r(e^{i\phi}+e^{-i\phi}) & 0 \\ 0 & 0 & 2 \end{bmatrix} \\ &= \begin{bmatrix} r\cos\phi & 0 & 0 \\ 0 & r\cos\phi & 0 \\ 0 & 0 & 1 \end{bmatrix}. \end{aligned} \tag{7.47}$$

It follows then, that

$$k = \sqrt{\det T_1} = \sqrt{r^2\cos^2\phi} = |r\cos\phi|\,, \tag{7.48}$$

and

$$T_1^c = \begin{bmatrix} \mathrm{sgn}\,(r\cos\phi) & 0 & 0 \\ 0 & \mathrm{sgn}\,(r\cos\phi) & 0 \\ 0 & 0 & 1 \end{bmatrix}. \tag{7.49}$$

If $r\cos\phi > 0 \implies T_1^c = \mathbb{1}$ and

$$Z'_\mu(x) = T_1^c\, Z_\mu(x) = Z_\mu(x)\,. \tag{7.50}$$

It is straightforward to see that $T_1^c = \mathbb{1} \implies T_i^c = \mathbb{1} \;\; \forall \;\; i$, and hence

$$Z_\mu^{(1)}(x) = Z_\mu(x)\,. \tag{7.51}$$

By induction,

$$Z_\mu^{(n)}(x) = Z_\mu(x) \;\; \forall \;\; n\,, \tag{7.52}$$

and the centre-vortex field is unchanged.

As such, in order to perturb the vortex field we require $r\cos\phi < 0$, or equivalently, $|\phi| > \frac{\pi}{2}$. This necessarily places a condition on the smearing parameter α. We consider this condition within the context of the over-improvement formalism [153], for which the staples term is given by the diagrammatic equation

$\Sigma_\mu^\dagger(x) = \sum_{\nu\neq\mu} \frac{5-2\epsilon}{3}$ 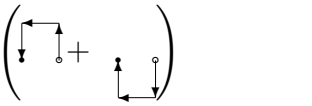 $+ \frac{\epsilon-1}{12u_0^2}$ 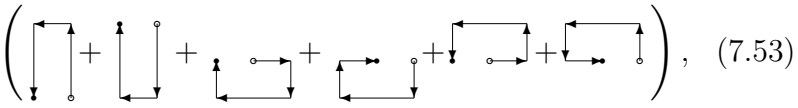 (7.53)

where the solid dot represents the point x, the open dot represents the point $x+\hat{\mu}$, and the links in the positive orthogonal direction $\hat{\nu}$ are shown as pointing vertically up the page. Note also that we have illustrated the link paths as oriented for the Hermitian conjugate $\Sigma_\mu^\dagger(x)$ which enters into Eq. (7.35).

The over-improvement formalism encapsulates standard APE smearing at over-improvement term $\epsilon = 1$. To ensure $r\cos\phi < 0$ we require that

$$\alpha > \alpha_{\min} = \frac{-6}{2\epsilon - 11 + \frac{3}{2}\left(\frac{\epsilon-1}{u_0^2}\right)}\,, \tag{7.54}$$

for $\epsilon \in \left[-\frac{5}{2}, 1\right]$, where u_0 is the mean link. See Appendix A.2 for a derivation.

In Figure 7.2, all possible values of $re^{i\phi}$ originating from a centre-vortex configuration for $\epsilon = -0.25$ and $u_0 = 1$, at $\alpha = 0.4$ and $\alpha = 0.7$, respectively, are plotted on the complex plane. At $\alpha = 0.7$ there are many combinations of links which yield $|\phi| > \frac{\pi}{2}$, but none at $\alpha = 0.4$. In fact, from equation (7.54), $\alpha_{\min}(\epsilon = -0.25, u_0 = 1) \approx 0.4486$. Of course, this is the limit to have *any* combi-

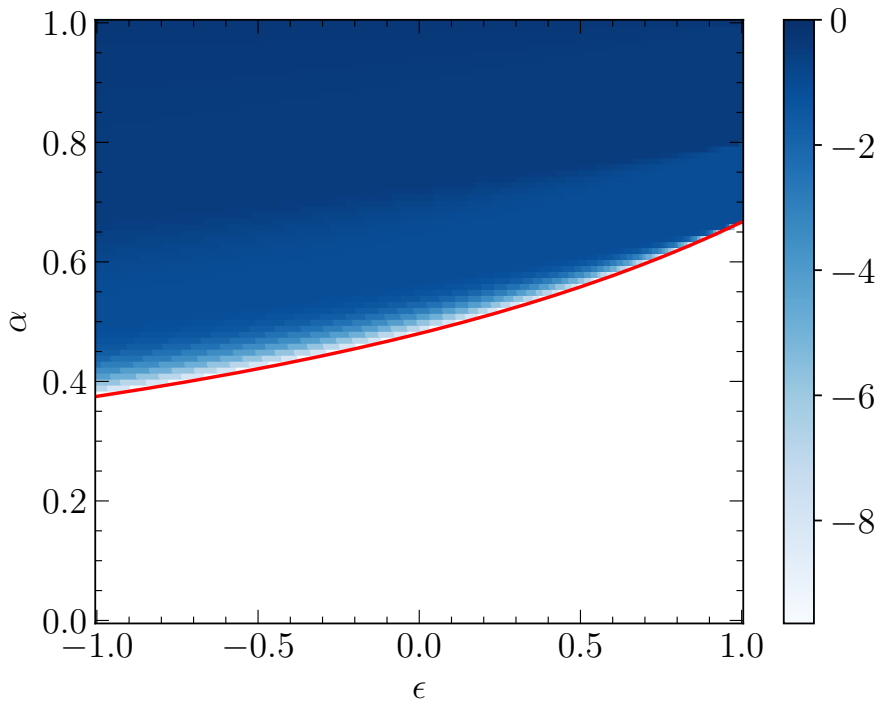

Figure 7.1: $\log_{10}(p_{\text{in}})$ as a function of ϵ and α, at $u_0 = 1$ fixed in the limit $\beta \to 0$. The shaded region illustrates the admissible values of α and ϵ where the proportion of acceptable link combinations, p_{in}, exceeds zero. The red line is $\alpha_{\min}(\epsilon)$.

nation of links yield $|\phi| > \frac{\pi}{2}$. In a practical sense, we require something more like $\alpha > 0.6$ to achieve effective smearing.

Figure 7.1 presents the proportion p_{in} of link combinations for which $|\phi| > \frac{\pi}{2}$ in the $\beta \to 0$ limit where each link in the construction of L^1 has an equal probability to be one of the centre phase elements. Each combination is weighted by its multiplicity. These do not reflect the true probabilities which would be encountered on an actual Z(3) centre-vortex gauge field, but suffice for demonstrative purposes.

7.3.1 Cooling/Annealing

While smearing algorithms update all links simultaneously, smoothing via a cooling or annealing process updates each link individually. These updates can be done in parallel with appropriate masking so as to preserve the validity of the cooling or annealing process [155]. The Wilson flow can be considered as an annealed version of stout-link smearing with a small smearing parameter. *Annealed U-link smearing* (AUS) [156] is similarly related to APE smearing in that the update process uses APE-style blocking and reuniterisation, but applied to individual links rather than

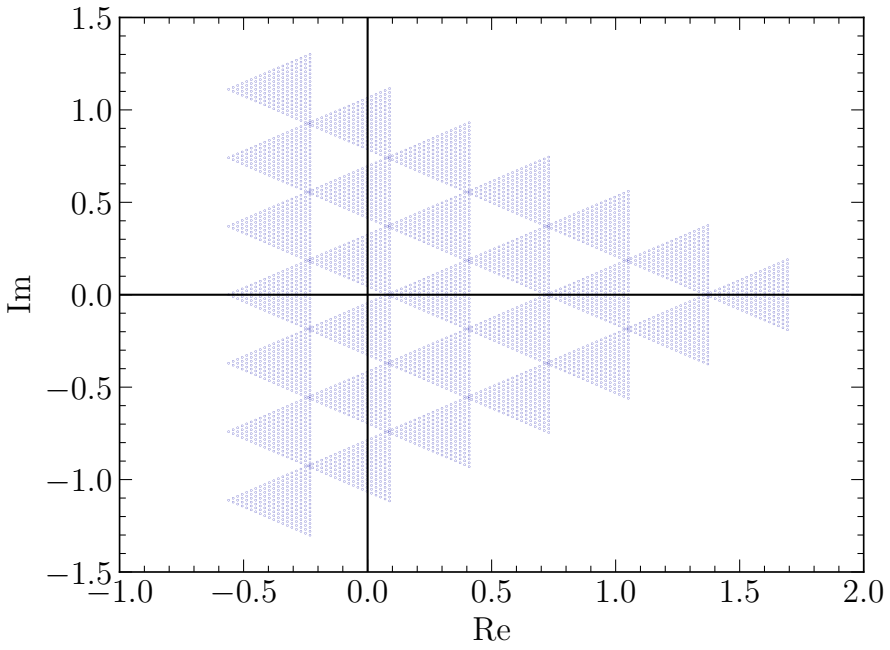

(a) $\epsilon = -0.25$, $\alpha = 0.7$

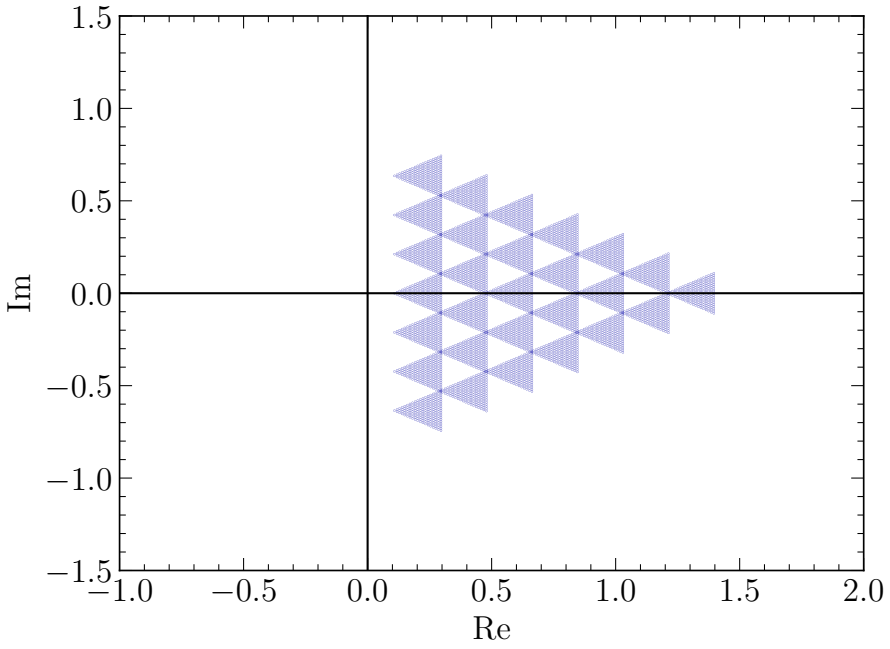

(b) $\epsilon = -0.25$, $\alpha = 0.4$

Figure 7.2: The complex plane showing all possible values of $re^{i\phi}$ for over-improvement term $\epsilon = -0.25$, at smearing parameters (a) $\alpha = 0.7$ and (b) $\alpha = 0.4$.

all links simultaneously. In particular, at $\alpha = 1.0$ the form of AUS with MaxReTr reuniterisation at the individual link level reduces to that of cooling [157–161], up to choice of operators in the staples term.

Our analysis with regard to vortex smoothing above extends to the annealed form of the various methods, and also to cooling in the special case of $\alpha = 1.0$. With regard to cooling it should be noted that it is possible to encounter some numerical issues when smoothing centre-vortex fields. From equations (7.36) and (7.46), we can write L^1 in arbitrary gauge as

$$L^1 = (1-\alpha) + \frac{\alpha}{6} Z_\mu(x)\, \Sigma_\mu^\dagger(x)\,, \tag{7.55}$$

which reduces to

$$L^1 = \frac{1}{6} Z_\mu(x)\, \Sigma_\mu^\dagger(x)\,, \tag{7.56}$$

for cooling ($\alpha = 1.0$), where $Z_\mu(x)$ and $\Sigma_\mu(x)$ are in MCG, i.e. they are proportional to $\mathbb{1}$.

Since $\Sigma_\mu(x)$ is a sum of elements of Z(3), each multiplied by some real factor, there exists combinations of links for which $\Sigma_\mu(x) = is\mathbb{1}$ and $s \in \mathbb{R}$, which is to say that the nonzero (diagonal) elements of $\Sigma_\mu(x)$ are purely imaginary. For example, in standard Wilson cooling where the 6 operators comprising the staples term are split two-to-four between $\mathbb{1}$ and $e^{\pm i\frac{2\pi}{3}}$ are examples of such combinations. In these cases the staples term is given by

$$\Sigma_\mu(x) = 2\mathbb{1} + 4e^{\pm i\frac{2\pi}{3}} = is \approx \pm i\, 3.464\ldots\,. \tag{7.57}$$

Without loss of generality, choose $Z_\mu(x) = \mathbb{1}$. Then

$$\begin{aligned} L^1 &= Z_\mu(x)\, V_\mu^\dagger(x) \\ &= \begin{bmatrix} -is & 0 & 0 \\ 0 & -is & 0 \\ 0 & 0 & -is \end{bmatrix}. \end{aligned} \tag{7.58}$$

Constructing T_1 according to equation (7.37),

$$\begin{aligned} T_1 &= \frac{1}{2} \begin{bmatrix} -is+is & 0 & 0 \\ 0 & +is-is & 0 \\ 0 & 0 & 2 \end{bmatrix} \\ &= \begin{bmatrix} 0 & 0 & 0 \\ 0 & 0 & 0 \\ 0 & 0 & 1 \end{bmatrix}, \end{aligned} \tag{7.59}$$

which implies $k = \sqrt{\det T_1} = 0$ and thus

$$\left[T_1^c\right]_{2\times 2} = \frac{1}{k}\left[T_1^\dagger\right]_{2\times 2}, \tag{7.60}$$

is undefined.

In practice, the diagonal elements of T_1 are not precisely 0 due to floating-point artefacts. From these artefacts, the algorithm is able to generate an essentially random SU(3) link without breaking or resulting in any obvious errors. This is apparent in Table 7.1, where at $\alpha = 1.0$, the number of links for which $Z_\mu^{(1)}(x) \neq Z_\mu(x)$, n_{diff}, is greater than n_{in}, the number of links for which $|\phi| > \frac{\pi}{2}$. Whilst this situation is rare (12 of 1,280,000 links in Table 7.1), the link, generated essentially from random noise, contaminates neighbouring links on the next iteration when it contributes to the staples term. The noise contamination continues to propagate throughout the lattice after each successive sweep, as the contaminated neighbours then contaminate their neighbours.

7.4 Centrifuge Preconditioning

The issues and limitations, outlined in previous sections, which arise when applying traditional smoothing methods to centre-vortex gauge fields, are all, at root, due to the proportionality of the links to the identity. As such, we introduce a method to break this symmetry without altering the fundamental vortex structure of the field. The key idea is to rotate the vortex links away from the centre elements before applying smoothing, and hence we call this new method *centrifuge preconditioning*.

We start with the original centre-vortex gauge field in MCG and denote

$$Z_\mu(x) = \begin{bmatrix} e^{i\lambda_\mu^1(x)} & 0 & 0 \\ 0 & e^{i\lambda_\mu^2(x)} & 0 \\ 0 & 0 & e^{i\lambda_\mu^3(x)} \end{bmatrix}, \tag{7.61}$$

where initially the diagonal entries $\lambda_\mu^i(x) = \lambda_\mu(x)$ are all equal. Noting that we are now within the diagonal subgroup of SU(3), which is isomorphic to U(1) × U(1) × Z(3), we can work with the phases directly in the noncompact representation. We

define the staple phase as

$$\sigma_\mu(x) = \frac{1}{6}\sum_{\nu\neq\mu}[\lambda_\nu(x) + \lambda_\mu(x+\hat{\nu}) - \lambda_\nu(x+\hat{\mu}) \\ -\lambda_\nu(x-\hat{\nu}) + \lambda_\mu(x-\hat{\nu}) + \lambda_\nu(x-\hat{\nu}+\hat{\mu})] \,. \quad (7.62)$$

A pair of indices $(j,k) \in \{(1,2),(2,3),(3,1)\}$ are selected randomly for each link, and then the corresponding phases of each original link are updated according to

$$\lambda^j_\mu(x) \to (1-\omega)\,\lambda_\mu(x) + \omega\,\sigma_\mu(x)\,, \quad (7.63)$$

$$\lambda^k_\mu(x) \to (1+\omega)\,\lambda_\mu(x) - \omega\,\sigma_\mu(x)\,, \quad (7.64)$$

where $\omega \in \mathbb{R}$ specifies the *centrifugal rotation angle,* noting that the centrifuge update above corresponds to a phase rotation by $\mp\omega(\lambda-\sigma)$. This leaves the sum of the three phases invariant. Hence, as the sum of the three phases of each centre element is distinct,

$$\sum_j \lambda^j_\mu(x) = n\,2\pi, \quad n \in \{-1,0,1\}, \quad (7.65)$$

after centrifuge preconditioning it is possible to uniquely identify the original centre element by this sum.

7.4.1 Preservation of Vortex Structure

Recall from equations (7.3) and (7.4) that the centre-vortex links are obtained by projecting the untouched link in maximal-centre gauge $U^G_\mu(x)$ to the centre element with phase nearest to $\arg\operatorname{Tr} U^G_\mu(x)$. Since we seek to break the diagonal symmetry of the centre-vortex links in such a way that preserves the underlying vortex structure, we restrict ω in Eqs. (7.63) and (7.64) such that $\arg\operatorname{Tr} Z_\mu(x) = 2\pi n_\mu(x)/3$ is preserved.

Let $Z'_\mu(x)$ denote the preconditioned centre vortex link with updated phases $\lambda^j_\mu(x)$ and $\lambda^k_\mu(x)$. It is simple to see that

$$\operatorname{Tr}\left[Z'_\mu(x)\right] = e^{i\lambda^j_\mu(x)} + e^{i\lambda^k_\mu(x)} + e^{i\frac{2\pi n}{3}}\,. \quad (7.66)$$

We then define

$$\Lambda^\pm = \frac{1}{2}\left(\lambda^j_\mu(x) \pm \lambda^k_\mu(x)\right). \quad (7.67)$$

Utilising polar form $e^{iA} = \cos A + i \sin A$, and the following trigonometric properties,

$$\cos A + \cos B = 2 \cos \frac{A+B}{2} \cos \frac{A-B}{2} \,, \tag{7.68}$$

$$\sin A + \sin B = 2 \sin \frac{A+B}{2} \cos \frac{A-B}{2} \,, \tag{7.69}$$

we obtain

$$\begin{aligned} e^{i\lambda_\mu^j(x)} + e^{i\lambda_\mu^k(x)} &= 2 \cos \Lambda^+ \cos \Lambda^- + i2 \sin \Lambda^+ \cos \Lambda^- \\ &= 2 \cos \Lambda^- \left(\cos \Lambda^+ - i \sin \Lambda^+ \right) \\ &= 2 \cos \Lambda^- e^{i \frac{2\pi n}{3}} \,. \end{aligned} \tag{7.70}$$

Hence,

$$\mathrm{Tr} \left[Z'_\mu(x) \right] = \left(2 \cos \Lambda^- + 1 \right) e^{n \frac{2\pi i}{3}} \tag{7.71}$$

and the phase of the trace is preserved,

$$\arg \mathrm{Tr} \left[Z_\mu(x) \right] = \arg \mathrm{Tr} Z'_\mu(x) = n \, 2\pi/3 \,, \tag{7.72}$$

provided

$$2 \cos \Lambda^- + 1 > 0 \,. \tag{7.73}$$

For the above condition to hold we must have

$$-\frac{2\pi}{3} < \Lambda^- < \frac{2\pi}{3} \,. \tag{7.74}$$

Explicitly this implies that

$$-\frac{2\pi}{3} < \omega \left[\sigma_\mu(x) - \lambda_\mu(x) \right] < \frac{2\pi}{3} \,, \tag{7.75}$$

where we have used equations (7.63) and (7.64). Since

$$\lambda_\mu(x) = n \, \frac{2\pi}{3} \,, \quad n \in \{-1, 0, 1\} \,, \tag{7.76}$$

$$\sigma_\mu(x) = m \, \frac{2\pi}{6 \cdot 3} \,, \quad m \in [-18, 18] \subset \mathbb{Z} \,, \tag{7.77}$$

we can rewrite equation (7.75) as

$$-\frac{2\pi}{3} < \omega \left[m \, \frac{2\pi}{6 \cdot 3} - n \, \frac{2\pi}{3} \right] < \frac{2\pi}{3} \,, \tag{7.78}$$

which for $\omega > 0$ simplifies to

$$\omega |m - 6n| < 6 \,. \tag{7.79}$$

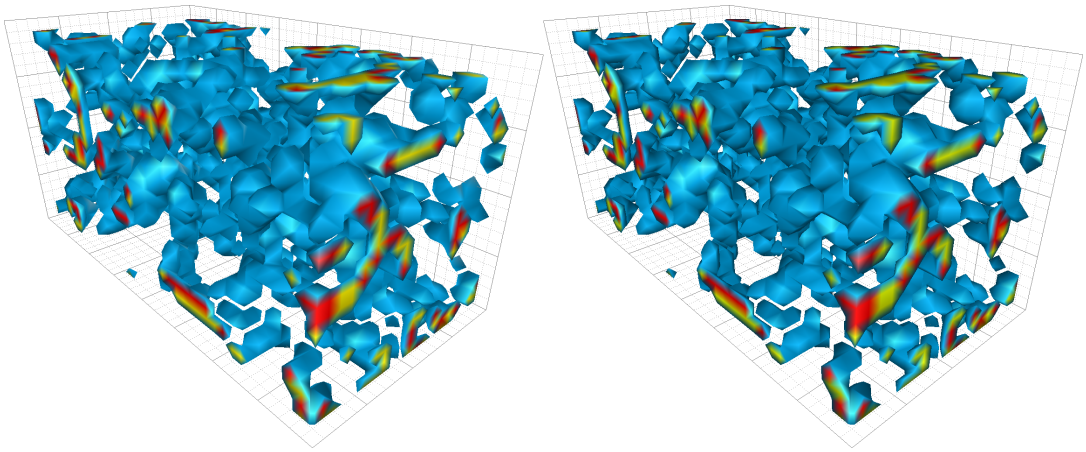

Figure 7.3: Action density $S(x)$ of a single time slice of a Z(3) centre-vortex gauge field before (left) and after (right) centrifuge preconditioning at $\omega = 0.02$. The initial mean action density $\langle S_{\mathrm{I}} \rangle = 0.046859$, the preconditioned mean action density $\langle S_{\mathrm{P}} \rangle = 0.049082$, and the correlation of the respective action densities $C^{S}_{\mathrm{IP}} = 0.99986$.

Considering the extrema where $m = \pm 18$ and $n = \mp 1$ we require that

$$\omega < \frac{1}{4} \,. \tag{7.80}$$

In practice, we always choose small $\omega \ll \frac{1}{4}$.

7.5 Centrifuge Preconditioned Smoothing

We consider a centre-vortex configuration projected from a $20^3 \times 40$ Luscher-Weisz $\mathcal{O}(a^2)$ mean-field-improved action pure-gauge configuration with lattice spacing $a = 0.125$ fm. This same configuration is used throughout the rest of this chapter. It is expected that the total action will increase after the vortex links have experienced centrifuge preconditioning. In general, we desire the centrifugal rotation angle ω to be small as we only wish to minimally perturb the vortex links.

In Figures 7.3 and 7.4 the action density $S(x)$ and topological charge density $q(x)$ of the centre-vortex gauge field are compared before and after the centrifuge preconditioning at $\omega = 0.02$ has been applied. This value of ω was chosen to sufficiently rotate the links away from the centre whilst keeping the increase in the total action to an acceptable level. Shown are the standard Wilson action density,

$$S(x) = \frac{\beta}{2n_c n_d (n_d - 1)} \sum_{\substack{\mu,\nu \\ \mu \neq \nu}} \mathrm{Re}\,\mathrm{Tr}\left[1 - P_{\mu\nu}(x)\right] \,, \tag{7.81}$$

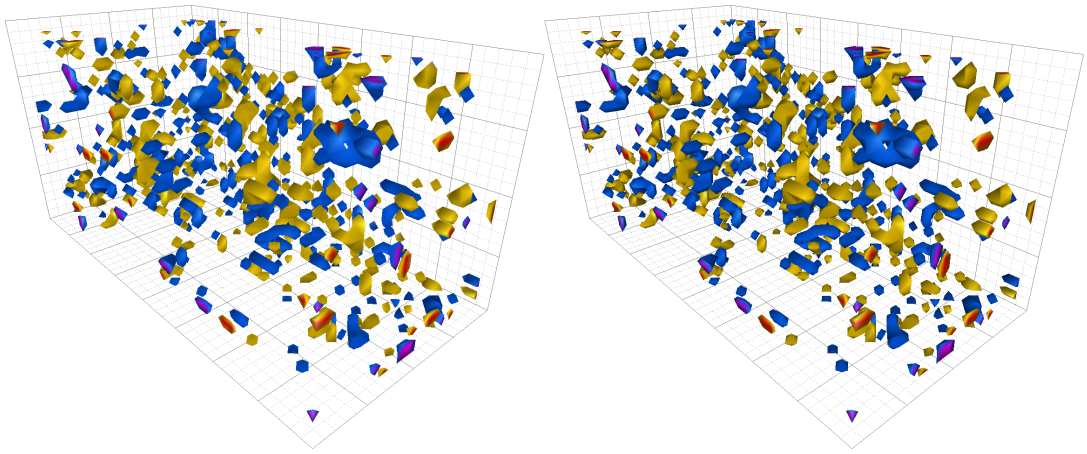

Figure 7.4: Topological charge density $q(x)$ of a single time slice of a Z(3) centre-vortex gauge field before (left) and after (right) centrifuge preconditioning at $\omega = 0.02$. The initial integrated topological charge $Q_{\mathrm{I}} = 0.75282$, the preconditioned integrated topological charge $Q_{\mathrm{P}} = 0.76792$, and the correlation of the respective topological charge densities $C^{q}_{\mathrm{IP}} = 0.99870$.

and the one-loop topological charge density,

$$q(x) = \frac{1}{32\pi^2}\epsilon_{\mu\nu\rho\sigma}\mathrm{Tr}\left[F^{\mu\nu}(x)F^{\rho\sigma}\right] , \tag{7.82}$$

where

$$F_{\mu\nu}(x) = \frac{1}{2ig}\left[C_{\mu\nu}(x) - C^{\dagger}_{\mu\nu}(x)\right] , \tag{7.83}$$

and $C_{\mu\nu}(x)$ is the 1×1 clover term. We denote the integrated topological charge as Q, where

$$Q = \sum_{x} q(x) . \tag{7.84}$$

Both the action and the topological charge densities appear invariant with only a few pixels in each respective image changing. This is reflected in the near-perfect correlation between the initial and precondition densities for both the action ($C^{S}_{IP} = 0.99986$) and topological charge ($C^{q}_{IP} = 0.99870$) where

$$C^{S}_{IP} = \frac{\langle S_I(x)\, S_P(x)\rangle}{\sqrt{\langle S^2_I(x)\rangle}\,\sqrt{\langle S^2_P(x)\rangle}} , \tag{7.85}$$

$$C^{q}_{IP} = \frac{\langle q_I(x)\, q_P(x)\rangle}{\sqrt{\langle q^2_I(x)\rangle}\,\sqrt{\langle q^2_P(x)\rangle}} , \tag{7.86}$$

and the subscripts I and P denote *initial* and *preconditioned*, respectively. This suggests that we have successfully broken the diagonal symmetry without significantly altering the underlying centre-vortex structure of the gauge field.

In general, we would consider the topological charge density to have physical meaning when the gauge field is smooth enough for the Atiyah-Singer index theorem to be satisfied [162], such that the gluonic definition of the integrated topological charge is approximately an integer and also agrees with the fermionic definition measured by the difference of left- and right-handed zero modes of the overlap-Dirac operator [163]. Previous studies show that 2 to 3 sweeps of standard stout-link smoothing at $\rho = 0.1$ is required for the lattice operators to become good approximations to the physical charge [164–166]. The extremely rough nature of the projected vortex fields do not satisfy this condition. However, we do note that on a centre vortex field the topological charge density necessarily correlates with the singular points of the dual vortices [167], and that after smoothing vortex fields can generate instanton-like structures [168]. Hence, the topological charge density remains of interest.

7.5.1 Smoothness Condition

As a measure of smoothness, we compare the mean densities of the standard Wilson action, and the reconstructed Wilson action [169], given by

$$\langle S \rangle = \frac{1}{n_{\text{lat}}} \sum_{x} S(x) \,, \tag{7.87}$$

and

$$\langle S_{\text{R}} \rangle = \frac{\beta}{2 n_c n_d (n_d - 1)} \frac{1}{n_{\text{lat}}} \sum_{x,\mu,\nu} \text{Tr} \left[F_{\mu\nu}(x) \, F_{\mu\nu}(x) \right] \,, \tag{7.88}$$

respectively.

The standard and reconstructed Wilson actions differ by $\mathcal{O}(a^6)$ terms and perturbative renormalisation factors. As the gauge field becomes smoother the perturbative contributions are suppressed and the renormalisation factors tend towards 1. Thus, the difference between the standard and reconstructed action can be used as a measure of the smoothness of the gauge field. We consider the gauge field sufficiently smoothed when $\langle S \rangle \approx \langle S_{\text{R}} \rangle$.

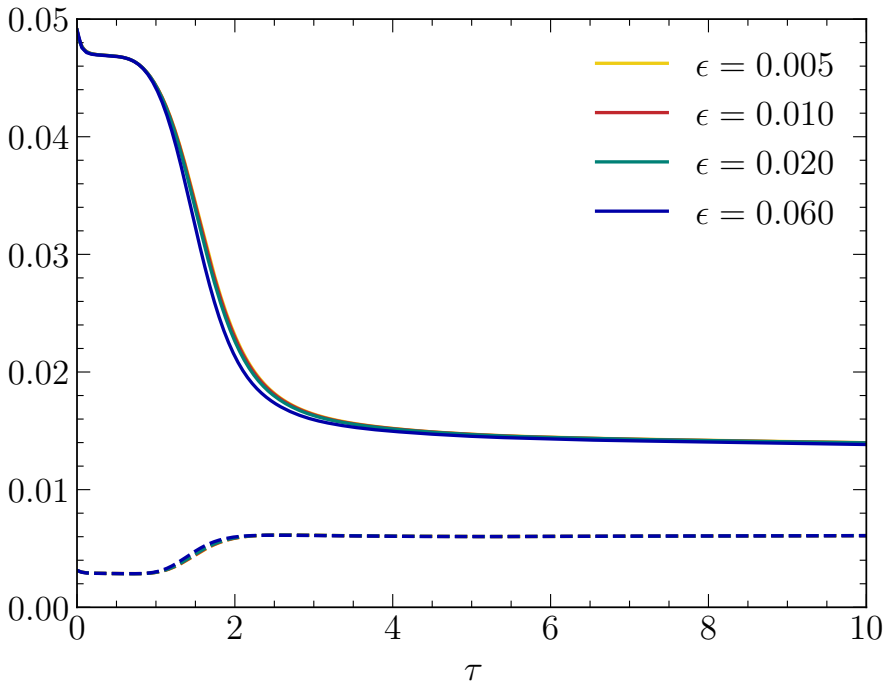

Figure 7.5: $\langle S \rangle$ (solid) and $\langle S_{\mathrm{R}} \rangle$ (dashed) as a function of Wilson flow time τ for integration step size $\epsilon = 0.005$, 0.01, 0.02, 0.06.

7.5.2 Smoothing in MCG

We examine centrifuge-preconditioned vortex fields that have been smoothed in MCG, starting with the Wilson flow. The Euler method for numerically integrating the Wilson flow [145] updates links according to

$$U_\mu(x,\tau) \to U_\mu(x,\tau+\epsilon) = e^{\epsilon Q_\mu(x)[U]}\, U_\mu(x,\tau). \tag{7.89}$$

In effect, this is an annealed implementation of stout-link smearing [33], where links are updated one at a time rather than simultaneously, and the smearing parameter ρ corresponds to the integration step size ϵ. It follows then, that flow time $\tau = n\rho$ after n sweeps of smearing. Whilst more sophisticated Runge-Kutta methods exist and have been used, we restrict our initial investigation to the Euler method.

Figure 7.5 shows the mean densities $\langle S \rangle$ and $\langle S_{\mathrm{R}} \rangle$ of the centrifuge-preconditioned gauge field as a function of Wilson flow time τ computed with Euler integration step sizes $\epsilon = 0.06$, 0.02, 0.01, 0.005. The flow is no longer invariant and smooths the gauge field, however the direct smearing of centrifuge-preconditioned vortex fields is insufficient to bring $\langle S \rangle$ and $\langle S_{\mathrm{R}} \rangle$ into agreement. The field remains rough and does

not satisfy the smoothness condition above, required for the overlap Dirac operator to be well-defined.

In the spirit of gradient flow, we now turn to annealed U-link smearing (AUS) with small $\alpha = 0.02$. As mentioned previously, AUS is identical in form to APE smearing, but the links are effectively updated one at a time rather than simultaneously. We employ the over-improvement formalism where the staples term is given in equation (7.53). We choose $\epsilon = -0.25$ as per Ref. [153]. We can consider AUS coupled with either unit-circle projection (AUS+UCP) or MaxReTr reuniterisation (AUS+MaxReTr).

Figure 7.6a shows the results for AUS with unit-circle projection. Again, as with the Wilson flow above, the centrifuge-preconditioned vortex field is smoothed, but insufficiently to bring $\langle S \rangle$ and $\langle S_{\mathrm{R}} \rangle$ into agreement and satisfy the required smoothness condition. We find similar results in Figure 7.6b where the MaxReTr reuniterisation has been used instead.

In all three of the cases above the smeared links remain diagonal. This is expected, as taking a linear combination of the diagonal matrices will result in a diagonal matrix for the staples, such that the smoothed link will also remain within the diagonal subgroup of SU(3). This means that the smoothing process is unable to form links that encompass the full manifold of the special unitary group.

The inability of these algorithms to smear the diagonal elements of a particular link into its off-diagonal elements appears to present a fundamental limitation to the amount of smoothing which can be achieved. As such, it seems necessary to employ an algorithm which is able to mix the diagonal and nondiagonal elements of a link. To this end, rather than starting from maximal-centre gauge we consider the addition of a random gauge transformation.

7.5.3 Smoothing in Random Gauge

The Wilson flow and AUS with unit-circle projection are gauge equivariant, which is to say for some smoothing process $\mathcal{S}$ and gauge transformation

$$U_\mu(x) \to U_\mu^G(x) = G(x)\, U_\mu(x)\, G^\dagger(x + \hat{\mu}) \tag{7.90}$$

that

$$\mathcal{S}\left\{U_\mu^G(x)\right\} = G(x)\, \mathcal{S}\left\{U_\mu(x)\right\} G^\dagger(x + \hat{\mu})\,. \tag{7.91}$$

As the linear combination of two diagonal matrices remains diagonal, this gauge equivariance prevents the analytic smoothing algorithms from leaving the diago-

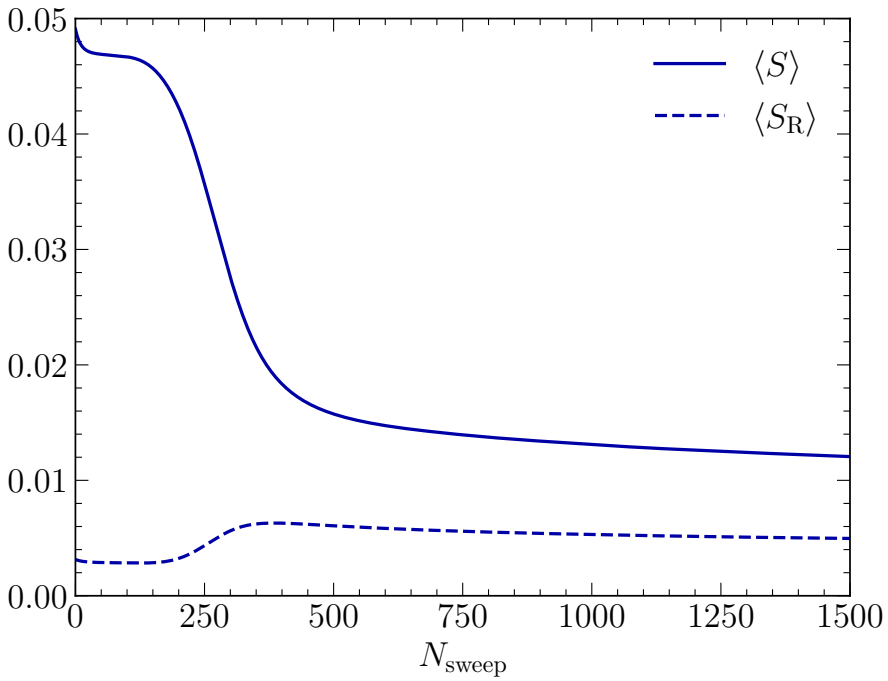

(a) Unit-circle projection.

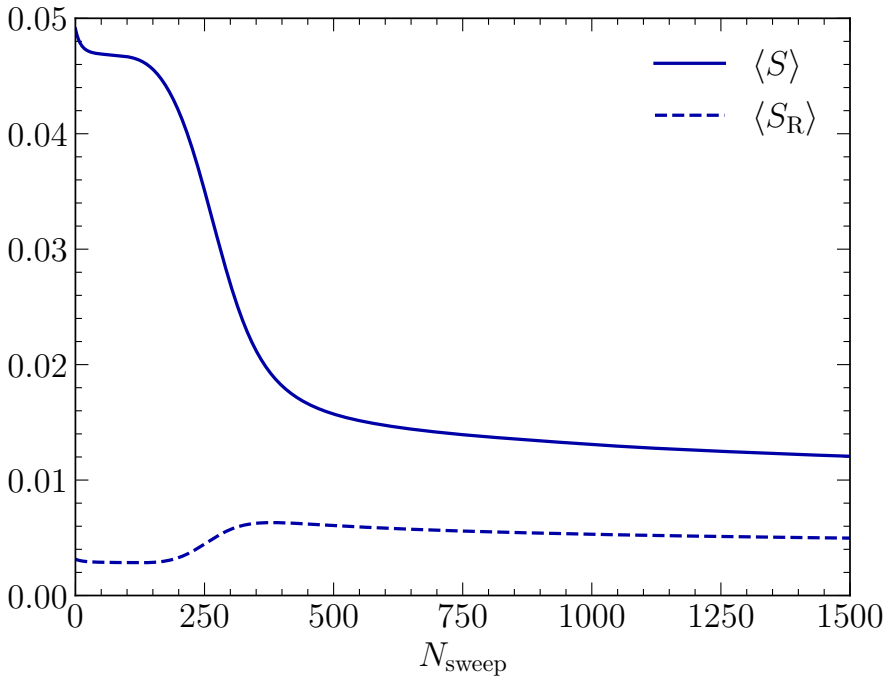

(b) MaxReTr reuniterisation.

Figure 7.6: $\langle S \rangle$ and $\langle S_{\text{R}} \rangle$ as a function of N_{sweep} iterations of over-improved AUS at $\epsilon = -0.25$ and $\omega = 0.02$ using (a) unit-circle projection and (b) MaxReTr reuniterisation, applied to a centrifuge preconditioned gauge field.

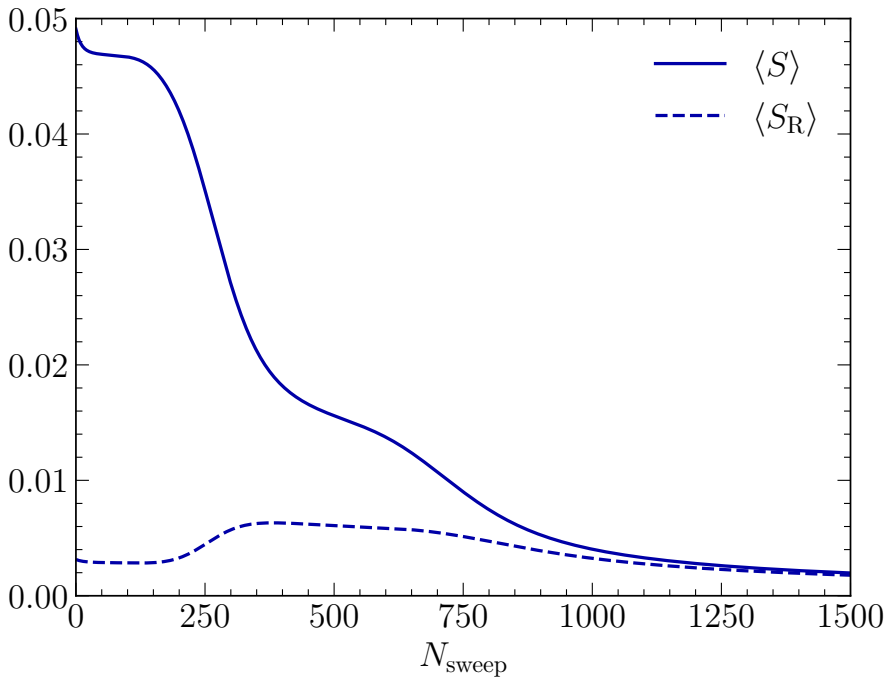

Figure 7.7: $\langle S \rangle$ and $\langle S_{\text{R}} \rangle$ as a function of N_{sweep} iterations of over-improved AUS at $\epsilon = -0.25$ and $\omega = 0.02$ using the MaxReTr reuniterisation applied to a centrifuge preconditioned gauge field which has been transformed to a random gauge.

nal subgroup of SU(3). This is not the case in general for AUS with MaxReTr reuniterisation. As such, we repeat the AUS+MaxReTr calculation with identical parameters, but this time we have transformed the centrifuge-preconditioned gauge field to a random gauge before smoothing. We see in Figure 7.7 that now the gauge field can be sufficiently smoothed, achieving agreement between the action and reconstructed action with enough ($N_{\text{sweeps}} > 1000$) sweeps of smoothing. We find that this smoothness condition is sufficient for the overlap Dirac operator to be well-defined.

7.6 Vortex-Preserved Annealing

One of the stated goals of finding a method to smooth centre-vortex gauge fields was to preserve the underlying vortex structure. To this end, we introduce *vortex-preserved annealed smoothing* (VPAS) via an additional accept/reject step, which, in principle, can be applied to any iterative smoothing algorithm.

Let us first consider VPAS applied to centre vortices in MCG. The AUS algorithm is run as usual to produce a candidate link in SU(3),

$$Z'_\mu(x) = \mathcal{P}_{\mathrm{SU(3)}} \left\{ V^{(n)}_\mu(x) \right\} . \tag{7.92}$$

The updated link is then given by

$$Z^{(n+1)}_\mu(x) = \begin{cases} Z'_\mu(x) \text{ if } \mathcal{P}_{\mathrm{Z(3)}} \left\{ Z'_\mu(x) \right\} = Z_\mu(x) , \\ Z^{(n)}_\mu(x) \text{ otherwise,} \end{cases} \tag{7.93}$$

which is to say a candidate link is only accepted if it projects back to the original centre vortex link using Eq. (7.3). In the case where the original centre vortex link as undergone an arbitrary gauge transformation

$$Z_\mu(x) \to G(x)\, Z_\mu(x)\, G^\dagger(x + \hat{\mu}) \tag{7.94}$$

the acceptance condition becomes

$$\mathcal{P}_{\mathrm{Z(3)}} \left\{ G^\dagger(x)\, Z'_\mu(x)\, G(x + \hat{\mu}) \right\} = Z_\mu(x) , \tag{7.95}$$

where the inverse of the original gauge transformation is applied to the candidate link. Note that in either case, the Z(3) projection test is performed directly without reasserting the MCG condition in Eq. (7.2).

We now consider how VPAS with MaxReTr reuniterisation applies to Z(3) centre-vortex gauge field configurations by studying the outcome of the first sweep. We first examine the MCG case, where no centrifuge preconditioning has been applied. We study three quantities in our analysis:

- p_{in} (n_{in}), the proportion (absolute number) of links which satisfy $|\phi| > \frac{\pi}{2}$ (required to perturb the vortex link),
- p_{diff} (n_{diff}), the proportion (absolute number) of links for which $Z^{(1)}_\mu(x) \neq Z_\mu(x)$ (accounting for the possibility that although the ϕ condition is satisfied, it is still possible the projected link could be the same as the original), and
- p_{pass} (n_{pass}), the proportion (absolute number) of candidate links which pass the vortex preservation step, given $Z^{(1)}_\mu(x) \neq Z_\mu(x)$.

These definitions necessitate the condition $p_{\mathrm{in}} \geqslant p_{\mathrm{diff}} \geqslant p_{\mathrm{pass}}$ holds.[1]

[1] See Section 7.3.1 for an explanation of the apparent violation of this condition at $\alpha = 1.0$ in Table 7.1.

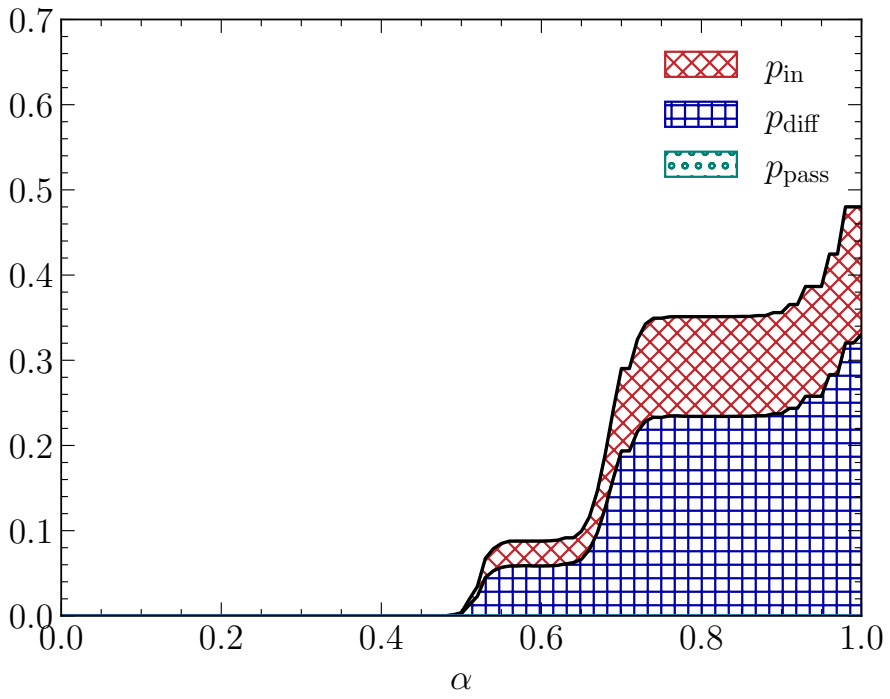

Figure 7.8: The proportion of all possible combinations of links, weighted by multiplicity, which satisfy $|\phi| > \frac{\pi}{2}$ (p_{in}), $Z_\mu^{(1)}(x) \neq Z_\mu(x)$ (p_{diff}), and pass the vortex preservation step given $Z_\mu^{(1)}(x) \neq Z_\mu(x)$ (p_{pass}). Note $p_{\text{pass}} = 0$ for all α.

In Figure 7.8, we compute these values for all combination of links, once again in the $\beta \to 0$ limit where a given link has an equal probability to be one of the three centre phases, and weight each combination by its multiplicity. Most strikingly, $p_{\text{pass}} = 0$ for all values of α. This implies that if the updated link is different from the original, the phase of its trace will always fall outside the sector which centre projects to the original link.

We repeat this analysis on a true Z(3)-projected gauge field configuration. The proportions are presented in Figure 7.9, whilst the absolute values are tabulated at intervals of 0.1 for α in Table 7.1. Consistent with the analysis presented in Figure 7.8, we see $p_{\text{pass}} = 0$ for all values of α and similar shaped curves for $p_{\text{diff}}(\alpha)$. However, unlike the previous analysis, we have that $p_{\text{in}} = p_{\text{diff}}$ for all α.

The same analysis is performed after centrifuge preconditioning and presented in Figure 7.10 and Table 7.2, where p_{in} has been dropped as this condition only applies to an unconditioned Z(3) gauge field where all links are proportional to the identity. Here (aside from the trivial $\alpha = 0$ case), we see not only that every updated link is different from the original at all values of α, but also that every candidate link passes the vortex preservation step below $\alpha \approx 0.5$ and almost all ($> 99.5\%$)

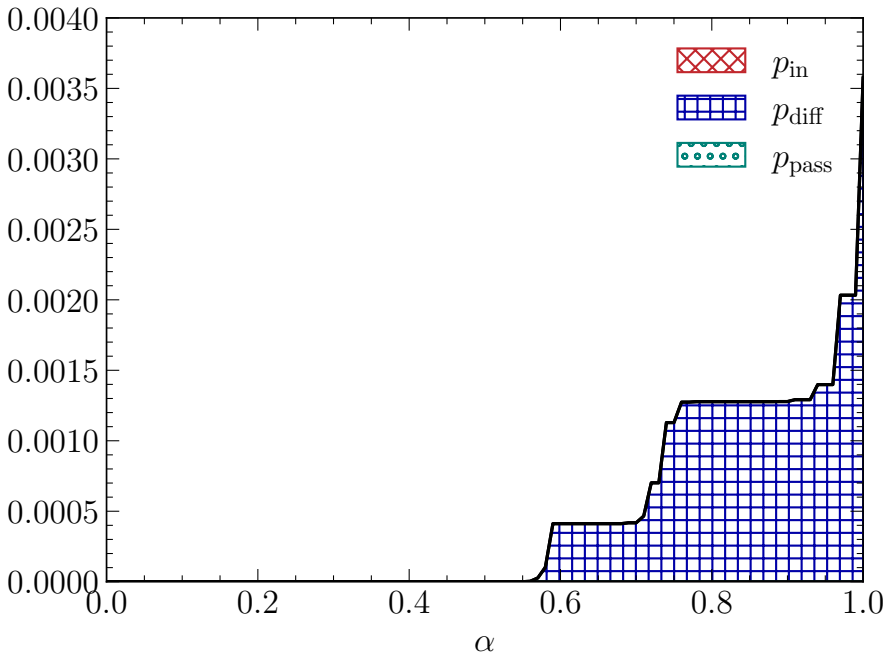

Figure 7.9: The proportion of links of a Z(3) pure gauge field configuration, which satisfy $|\phi| > \frac{\pi}{2}$ (p_{in}), $Z_\mu^{(1)}(x) \neq Z_\mu(x)$ (p_{diff}), and pass the vortex preservation step given $Z_\mu^{(1)}(x) \neq Z_\mu(x)$ (p_{pass}). Note $p_{\text{pass}} = 0$ for all α and $p_{\text{in}} = p_{\text{diff}}$ for all $\alpha < 1$.

at larger values of α. While this suggests that a vortex-preservation step is not required for $\alpha < 0.5$, we note this is only for the first sweep following centrifuge preconditioning. Eventually, the vortex-preservation step does have an effect on the smoothing process.

Performing the same one-sweep analyses, after a random gauge transform has been applied, produces near-identical results, and for the sake of brevity will not be presented herein. This is not unexpected, as we are only considering the first sweep. Comparing Figures 7.6 and 7.7, the random gauge transformation only begins to have significance after several sweeps.

Applying VPAS with MaxReTr reuniterisation to a centrifuge-preconditioned gauge field, we find similar results, presented in Figure 7.11, to what we have seen with regular AUS. Once again, applying a random gauge transformation to the field is necessary to achieve sufficient smoothing.

7.7 Smoothing Method Comparison

Throughout the previous sections, we have arrived at three viable smoothing methods for Z(3) centre-vortex gauge fields. In Section 7.2.3 we showed that an APE-style

Table 7.1: The number of links of a Z(3) pure gauge field configuration satisfying various conditions. n_{in} counts the links which satisfy $|\phi| > \frac{\pi}{2}$. n_{diff} counts the links for which $Z_\mu^{(1)}(x) \neq Z_\mu(x)$. n_{pass} counts the links satisfying the preservation condition given $Z_\mu^{(1)}(x) \neq Z_\mu(x)$. The $20^3 \times 40$ lattice has 1,280,000 links.

α	n_{in}	n_{diff}	n_{pass}
0.4	0	0	0
0.5	0	0	0
0.6	527	527	0
0.7	535	535	0
0.8	1635	1635	0
0.9	1636	1636	0
1.0	4570	4582	0

smearing algorithm can only alter a Z(3) vortex field provided the smearing parameter α is sufficiently large. Furthermore, in Section 7.3 we found that the degree of smoothing was only sufficient if the vortex field had undergone a random gauge transformation and the MaxReTr reuniterisation was employed. Choosing also to employ the over-improvement formalism at $\epsilon = -0.25$ with smearing parameter $\alpha = 0.7$ and, implementing the algorithm in an annealed manner, we have arrived at our first smoothing recipe which we denote throughout this section as 'AS' for annealed smoothing.

In the spirit of approaching the gradient flow, we showed in Section 7.5 that the use of a small smearing parameter $\alpha < \alpha_{\text{min}}$ is enabled by centrifuge preconditioning the vortex field. A random gauge transformation is necessarily applied after preconditioning to achieve the required level of smoothing to define our second recipe which we denote 'CP' for centrifuge preconditioning. We choose an AUS smearing parameter of $\alpha = 0.02$ applied to a random-gauge-transformed, centrifuge-preconditioned gauge field with rotation angle $\omega = 0.02$. Finally, in our third recipe, denoted 'VP' for vortex preservation, we include the vortex preservation step in what is otherwise identical to our second recipe.

In addition to the resultant gauge fields of each smoothing recipe, we also consider the original Z(3) gauge field (denoted 'VO' for vortex-only) without any smoothing as a reference.

In summary, we have four gauge fields to compare:

VO original vortex-projected gauge field,

AS large α, APE-style, random-gauge-transformed annealed smoothing,

Table 7.2: The number of links of a centrifuge preconditioned Z(3) pure gauge field configuration, which satisfy $|\phi| > \frac{\pi}{2}$ (p_{in}), $Z_\mu^{(1)}(x) \neq Z_\mu(x)$ (p_{diff}), and pass the vortex preservation step given $Z_\mu^{(1)}(x) \neq Z_\mu(x)$ (p_{pass}). The lattice has 1280000 links.

α	n_{diff}	n_{pass}
0.1	1280000	1280000
0.2	1280000	1280000
0.3	1280000	1280000
0.4	1280000	1280000
0.5	1280000	1280000
0.6	1280000	1279473
0.7	1280000	1278853
0.8	1280000	1278363
0.9	1280000	1277673
1.0	1280000	1274937

CP as for AS except with small α and centrifuge preconditioning,

VP as for CP but with vortex-preservation step applied.

We present the mean action $\langle S \rangle$ and reconstructed action $\langle S_{\text{R}} \rangle$ densities for each algorithm as a function of αN_{sweep} in Figure 7.12. Similarly, in Figure 7.13, we present the integrated topological charge Q for each algorithm as a function of αN_{sweep}. The reference value for the vortex-only field (without any smoothing) is represented as a dashed horizontal line.

The trajectories of the mean action density for CP and VP are nearly identical, so as to be almost indistinguishable for the majority of the smoothing trajectory. A more detailed analysis is necessary to elucidate any subtle differences that exist between the respective algorithms. Meanwhile the trajectory for AS is roughly proportionate to the CP and VP curves for $\alpha N_{\text{sweep}} < 6$ but diverges rapidly above that threshold.

The difference between the large-α AS algorithm and the small-α CP and VP algorithms is most apparent in the trajectories of the integrated topological charge. CP and VP track relatively closely, with a small divergence from $\alpha N_{\text{sweep}} \sim 7$ after which they appear to be converging on the same integer value by $\alpha N_{\text{sweep}} \sim 30$. By contrast, the AS trajectory acutely diverges from the CP and VP curves at around $\alpha N_{\text{sweep}} \sim 5$.

In order to perform a more detailed analysis, we choose a fixed number of AUS sweeps for each algorithm (20 for AS, and 1190 for CP and VP) as a point of comparison, such that the different gauge fields have approximately matched total

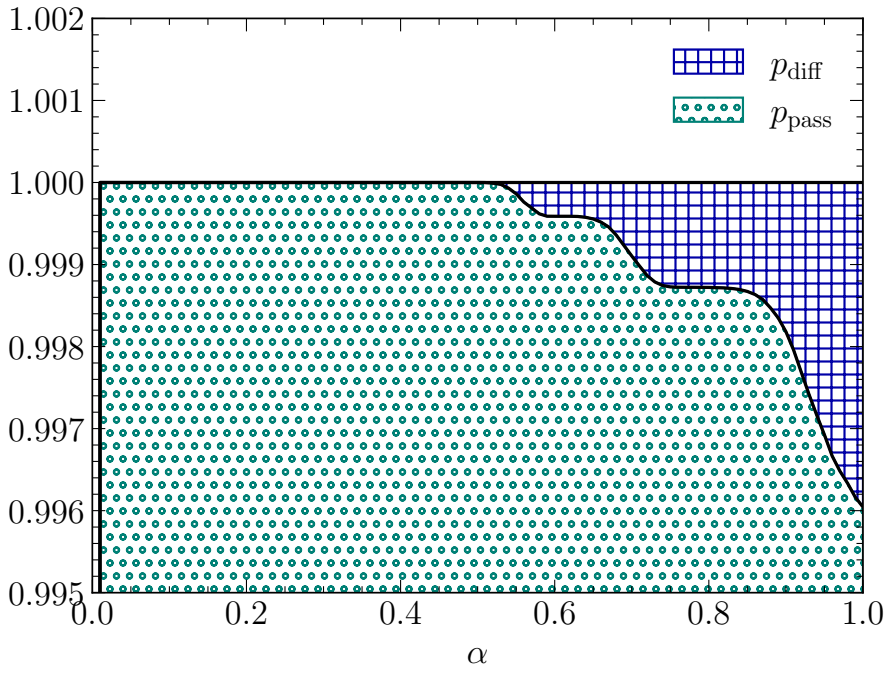

Figure 7.10: The proportion of links of a centrifuge preconditioned Z(3) pure gauge field configuration, which satisfy $Z_\mu^{(1)}(x) \neq Z_\mu(x)$ (p_{diff}), and pass the vortex preservation step given $Z_\mu^{(1)}(x) \neq Z_\mu(x)$ (p_{pass}). Note that $p_{\text{in}} = 1$ for all α.

actions. The respective number of sweeps chosen for each algorithm are marked by stars in Figures 7.12 and 7.13. See Table 7.3 for a summary of each algorithm in the context of the following discussion.

We present visualisations of the respective action densities in Figure 7.14 and compute their correlations where C_{XY}^S given by

$$C_{XY}^S = \frac{\langle S_X(x)\, S_Y(x)\rangle}{\sqrt{\langle S_X^2(x)\rangle}\,\sqrt{\langle S_Y^2(x)\rangle}}\,, \tag{7.96}$$

is the correlation between $S_X(x)$ and $S_Y(x)$ for respective smearing processes X and Y. These are presented in Table 7.4.

Similarly, we present visualisations of the respective topological charge densities in Figure 7.15 and compute their correlations where C_{XY}^q given by

$$C_{XY}^q = \frac{\langle q_X(x)\, q_Y(x)\rangle}{\sqrt{\langle q_X^2(x)\rangle}\,\sqrt{\langle q_Y^2(x)\rangle}}\,, \tag{7.97}$$

is the correlation between $q_X(x)$ and $q_Y(x)$ for respective smearing processes X and Y. These are presented in Table 7.5.

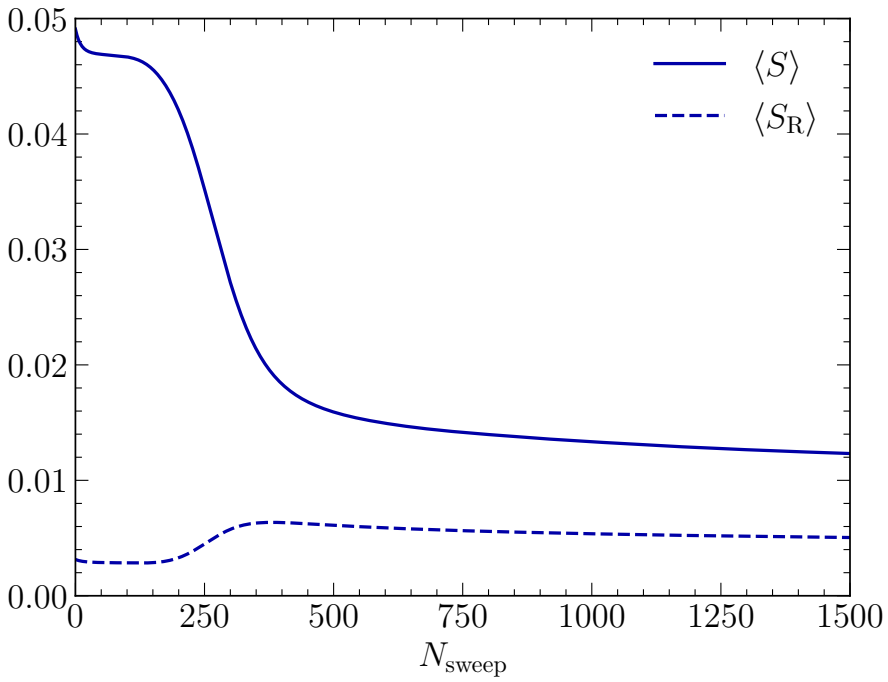

(a) No random gauge transformation.

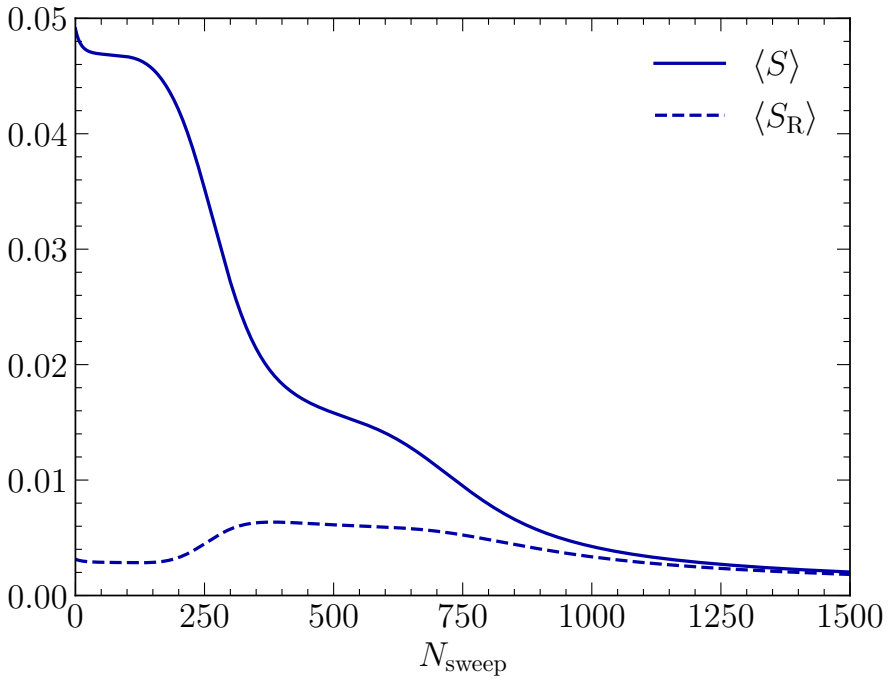

(b) Random gauge transformation.

Figure 7.11: $\langle S \rangle$ and $\langle S_{\text{R}} \rangle$ as a function of N_{sweep} iterations of over-improved VPAS at $\epsilon = -0.25$ and $\omega = 0.02$ using the MaxReTr reuniterisation applied to a centrifuge preconditioned gauge field (a) without and (b) with a random gauge transformation applied after preconditioning and before smoothing.

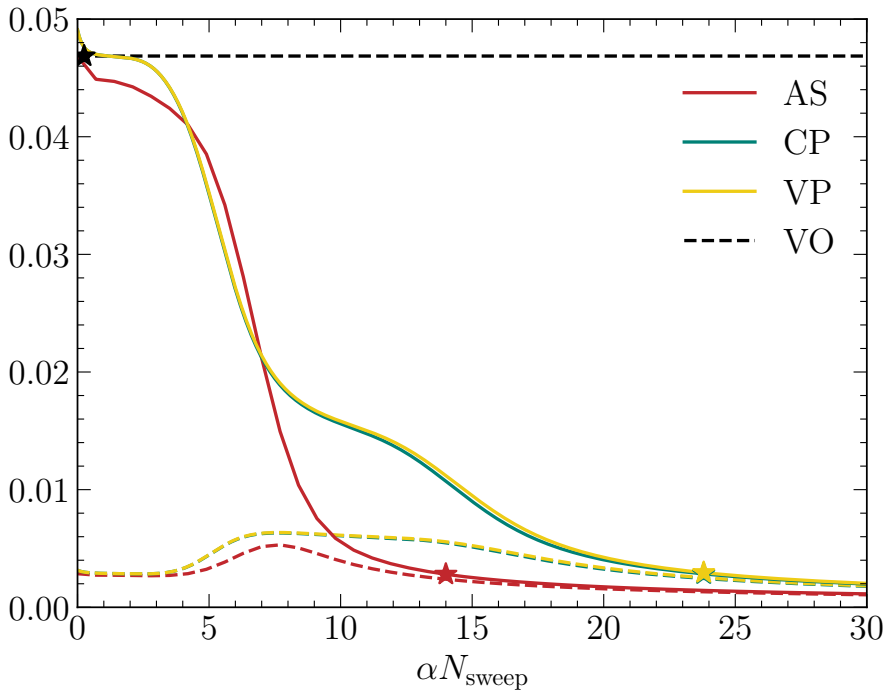

Figure 7.12: $\langle S \rangle$ (solid) and $\langle S_{\text{R}} \rangle$ (dashed) as a function of αN_{sweep} for each smoothing algorithm. The stars denote the number of sweeps chosen for algorithm comparison ($N_{\text{sweep}} = 20$ for AS, $N_{\text{sweep}} = 1190$ for CP and VP).

The superior similarity of the CP and VP action densities to the original vortex field evident in the visualisations, as compared to AS, indicates not only that the use of a small smearing parameter is desirable, but it is fundamentally important in preserving the underlying vortex structure. With regard to the action density, the numerical correlation of VP with the original vortex field is slightly higher (by $\sim 2\%$) as compared to AS and CP.

Visually, the topological charge density for VO is qualitatively different to the three smoothed fields in terms of the size and number of objects. The numerical comparison of the topological charge densities indicates they are essentially uncorrelated, with the exception of CP and VP which do show a strong positive numerical correlation and similarity in their visualisations.

7.8 Summary

Throughout this chapter we have studied the application of a variety of SU(3) gauge field smoothing methods to Z(3) centre-vortex gauge fields, with an aim to achieve sufficient smoothness to be able to meaningfully evaluate the overlap Dirac operator.

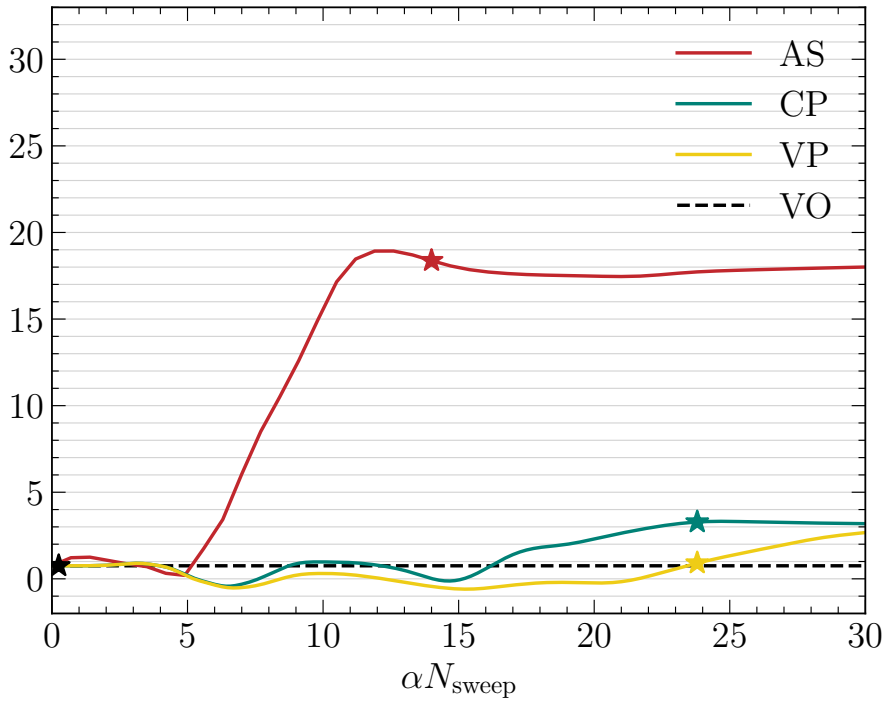

Figure 7.13: Integrated topological charge Q as a function of αN_{sweep} for each smoothing algorithm. The stars denote the number of sweeps chosen for algorithm comparison ($N_{\text{sweep}} = 20$ for AS, $N_{\text{sweep}} = 1190$ for CP and VP).

An additional aim is to preserve (as much as possible) the original vortex structure identified in MCG. Due to the proportionality of the vortex-field links to the identity, a naive application of traditional smoothing algorithms is either ineffectual or limited, containing subtle issues which are not obviously manifest.

To overcome these issues, we introduced a novel method, centrifuge preconditioning, which perturbs the centre elements from Z(3) into the U(1) × U(1) × Z(3) diagonal subgroup of SU(3). The centrifuge preconditioning step is constructed in a manner that breaks the proportionality of the links to the identity while preserving the original vortex information.

Agreement between the action and reconstructed action was set as the condition for sufficient smoothness in order to employ overlap fermions on the smoothed vortex field. The amount of smoothing that can be obtained with analytic methods is fundamentally limited by the gauge equivariant property of these methods, which even with centrifuge preconditioning remain within the diagonal subgroup of SU(3) (up to a gauge transformation).

It is only through the application of a random gauge transformation, together with the MaxReTr reuniterisation – an update-based method that is not gauge

Table 7.3: Summary of smoothing recipes. Steps are applied from left to right starting with the Z(3) centre-vortex configuration in MCG. C indicates centrifuge preconditioning with rotation angle ω. R indicates the application of a random gauge transformation. N_{AUS} indicates the number of sweeps of AUS at smearing parameter α. V indicates if a vortex-preservation step was included in the AUS smearing.

Algorithm	C	ω	R	N_{AUS}	α	V
VO	×	-	×	0	-	-
AS	×	-	✓	20	0.7	×
CP	✓	0.02	✓	1190	0.02	×
VP	✓	0.02	✓	1190	0.02	✓

Table 7.4: The correlation C^S_{XY} of action densities $S_X(x)$ and $S_Y(x)$ of the gauge fields after respective smoothing algorithms X and Y have been applied.

	VO	AS	CP	VP
VO	1.000	0.397	0.397	0.404
AS	-	1.000	0.518	0.512
CP	-	-	1.000	0.943
VP	-	-	-	1.000

equivariant – as part of an APE-based annealed smoothing formalism, that it becomes possible to depart from the diagonal subgroup and expand the smoothed links to the greater part of the SU(3) group manifold.

Additional to centrifuge preconditioning, to preserve the vortex structure throughout the annealed smoothing process, the concept of a vortex-preservation step was introduced. This consists of an accept/reject step within the annealed smoothing process, where the update for a given link is only accepted if the argument of the trace projects to the same Z(3) element as the centre phase identified in the MCG of the original gauge field.

Table 7.5: The correlation C^q_{XY} of topological charge densities $q_X(x)$ and $q_Y(x)$ of the gauge fields after respective smoothing algorithms X and Y have been applied.

	VO	AS	CP	VP
VO	1.000	0.010	-0.001	0.002
AS	-	1.000	0.009	0.000
CP	-	-	1.000	0.886
VP	-	-	-	1.000

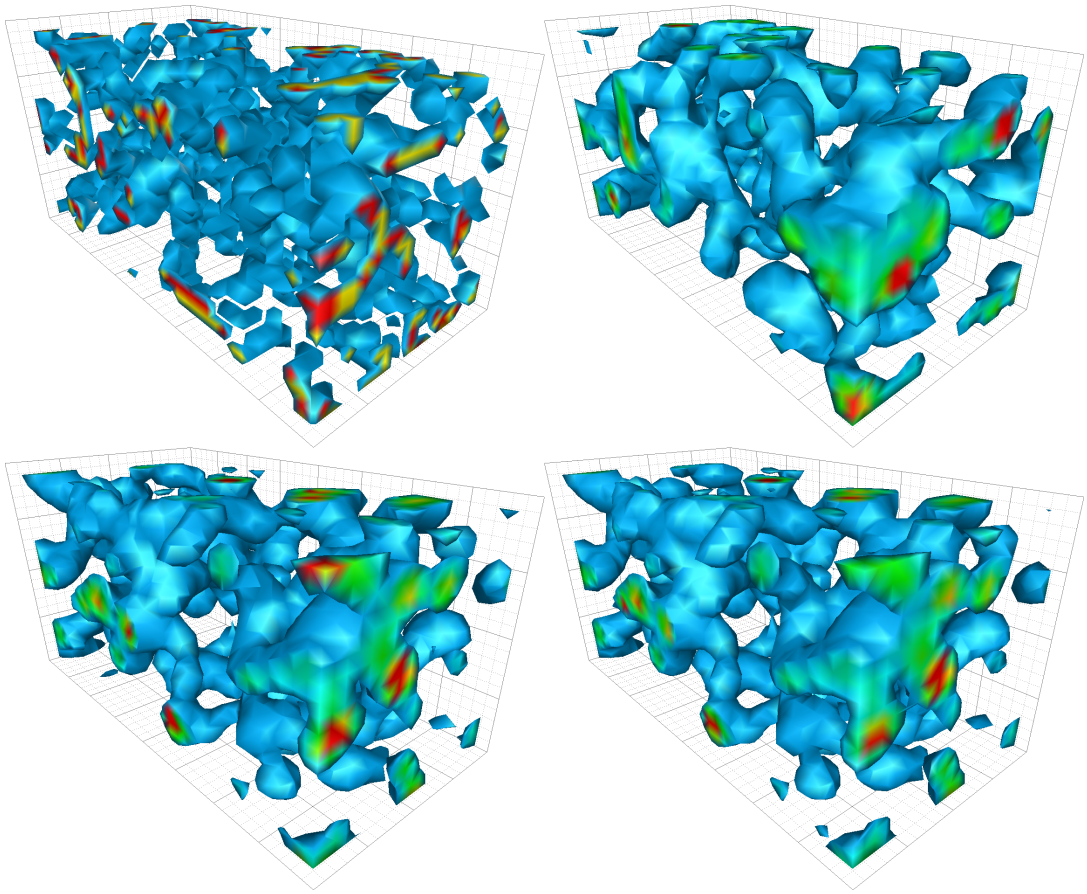

Figure 7.14: Action density of a single time slice after smoothing. Clockwise from top left: VO, AS, CP, VP.

Based on the above, three smoothing recipes were formulated (AS, CP, VP) which along with the pure vortex field (VO) were compared (refer to Table 7.3 for a summary). With regard to the action density, the visualisations in Figure 7.14 show the CP and VP algorithms produce action densities resembling the original vortex structure. Considering the quantitative measure of Eq. (7.96), all three smoothing recipes were found to have a similar correlation with the original field, with VP having the highest of the three by a small margin. On such rough fields, the microscopic structure of the topological charge density appears to be volatile and as a result there is essentially no correlation between three of the four fields examined. The exceptional pair is CP and VP, which produce highly correlated topological charge densities, the only difference between these two recipes being that VP includes the vortex-preserved annealing step ensuring that the argument of the trace of the links projects to the original centre element.

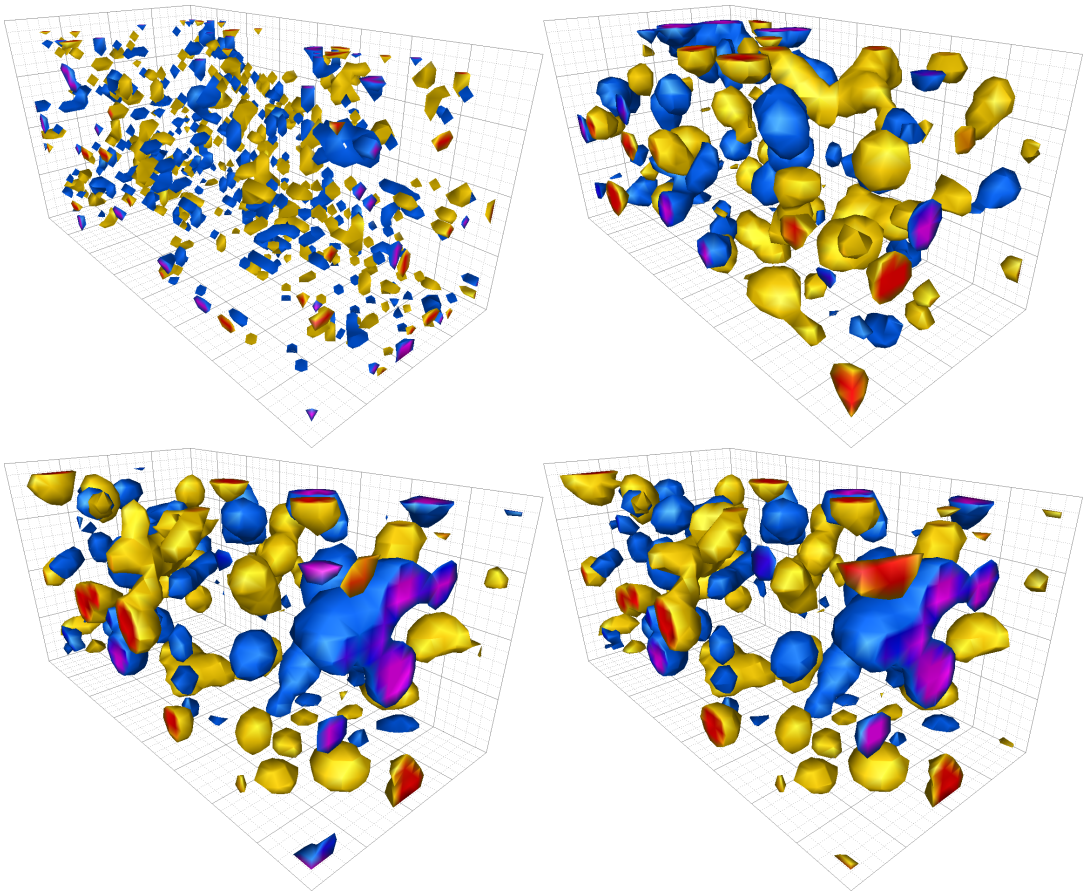

Figure 7.15: Topological charge density of a single time slice after smoothing. Clockwise from top left: VO, AS, CP, VP.

We conclude that centrifuge preconditioning and vortex-preserved annealing techniques enable the successful smoothing of vortex fields, and will be studied further in future work.

Chapter 8

Vortex-Modified Quark Propagator

8.1 Centre Vortices and Nonperturbative QCD

There is a strong and increasing body of evidence supporting centre vortices as the mechanism underpinning confinement and dynamical chiral symmetry breaking, the two key features of low-energy, nonperturbative QCD [4, 5, 99, 137, 140, 142, 168, 170–199]. Whilst the results of these studies demonstrate a clear role for centre vortices in the mediation of these phenomena, it is also clear there is more to be understood.

This is apparent in recent studies of the static quark potential and the gluon propagator in dynamical QCD. Whilst vortex removal in pure-SU(3) gauge results in a loss of string tension, and thus confinement, only about two-thirds of the original string tension is recovered on the corresponding vortex-only background [137, 168, 191]. The loss of string tension upon vortex removal is a clear sign of the important role of centre vortices in confinement, and is further supported by its partial recovery on a vortex-only background. However, the 'missing' third of the string tension remains unaccounted for, suggesting there is more to be understood. This quantitative discrepancy is broadly illustrative of the findings of pure-gauge centre-vortex studies, some of which are discussed in further detail below.

In light of these results, a recent study [4] explored the impact of dynamical fermions on the relationship between centre vortices and the string tension. Here, the centre vortex structure of configurations generated with 2+1 dynamical flavours of fermion [64] were examined. Once again, in agreement with pure-gauge results, the string tension vanishes upon vortex removal. However, it was found that the original string tension is fully recovered on a vortex-only background. The quantitative discrepancy present in the pure-gauge sector is resolved in the presence of dynamical fermions.

A similar pattern is observed in studies of the gluon propagator. Although the infrared enhancement of the gluon propagator is suppressed upon vortex removal in pure gauge, a residual strength still persists [5, 193, 198]. This is consistent with positivity violation observed in the correlator at large distances, and demonstrates an imperfect separation between perturbative and nonperturbative physics upon vortex modification. In the presence of dynamical fermions, however, the vortex-removed correlator is consistent with positivity, and the residual infrared strength in the propagator is significantly diminished [5]. As such, vortex modification in the presence of dynamical fermions provides an effective separation between the perturbative and nonperturbative aspects of QCD.

These results demonstrate an intimate link between dynamical fermions and centre vortices. Although the nature of this relationship is at this stage unclear, the resolution of the quantitative discrepancies present in the pure-gauge sector provide further strong evidence supporting centre vortices as the origin of confinement in QCD. The existence of such a link provides strong motivation to consider the effect of dynamical fermions on the role of centre vortices in dynamical chiral symmetry breaking.

It is well-established that centre vortices are responsible for dynamical chiral symmetry breaking in SU(2) gauge theory [175, 182, 188–190, 195, 196]. Meanwhile, hadron spectra computed with Wilson fermions on pure-SU(3) gauge vortex-removed ensembles display an absence of dynamical chiral symmetry breaking [194]. A similar study which instead employed overlap fermions was not only able to demonstrate the restoration of chiral symmetry upon vortex-removal, but reproduced the salient features of the spectrum on a vortex-only background [142]. There are, however, slight discrepancies in the masses obtained on the vortex-only background which are lower than those obtained from the original, untouched ensemble, although this may simply be an artefact of the cooling applied to the vortex-only gauge fields.

Less readily explainable discrepancies are manifest in the pure-SU(3) gauge Landau-gauge overlap quark propagator [99]. Although dynamical mass generation in the quark propagator mass function, a clear signal of dynamical chiral symmetry breaking, is fully reproduced on a vortex-only ensemble, a quantitative discrepancy arises in the persistence of dynamical mass generation upon vortex-removal. This once again suggests centre vortices do not capture the full nonperturbative physics of the pure-gauge sector.

Given the intimate link between dynamical fermions and centre vortices demonstrated by the resolution of quantitative discrepancies present in the pure-gauge string tension and gluon propagator, it is plausible that dynamical fermions could

resolve the discrepancy present in the pure-gauge Landau-gauge overlap quark propagator. To this end, in this chapter we investigate the behaviour of the Landau-gauge overlap quark propagator upon vortex modification in dynamical QCD.

8.2 Vortex-Removed Quark Propagator

8.2.1 Simulation Parameters

We compute the overlap quark propagator as per Subsection 5.1.1, with the sole exception that the $32^3 \times 64$ PACS-CS 2+1-flavour ensemble [64] used in Chapter 5 has here undergone vortex-removal as outlined in Section 7.1.

8.2.2 Results

The vortex-removed mass function is compared with the untouched mass function of Chapter 5 in Figure 8.1, for each mass considered. Similarly, the respective renormalisation functions are presented in Figure 8.2. We also compare the current dynamical results with those from Ref. [99] which were obtained in the pure-gauge sector in Figures 8.3 and 8.4. For this purpose, we select the lightest available quark mass from Ref. [99], $m_q = 12$ MeV, and compare it to the nearest (and second-lightest) quark mass considered in this work, $m_q = 9$ MeV.

Upon vortex removal, dynamical mass generation vanishes at the lightest quark masses. Whilst dynamical mass generation is suppressed upon vortex removal in the pure-gauge sector, a significant remnant with a peak above 100 MeV persists as seen in Figure 8.4a. In the dynamical case, however, the removal of centre vortices suppresses dynamical mass generation to the fullest extent possible in the presence of some small explicit chiral symmetry breaking associated with the finite bare mass. The significant improvement in the elimination of dynamical mass generation upon centre vortex removal in the dynamical case resolves an important shortcoming in the pure-gauge sector. More generally, the quark mass governs the degree to which chiral symmetry is explicitly broken. This is reflected in Figure 8.1 by the small remnant of dynamical mass generation becoming more prominent with increasing quark mass. This offers a framework to interpret the renormalisation function results presented in Figure 8.2.

The respective untouched and vortex-removed renormalisation functions are near identical for $p > 1$ GeV. The similarity in this region is consistent with previous pure-gauge overlap results as highlighted in Figure 8.4. We see however, that whilst the

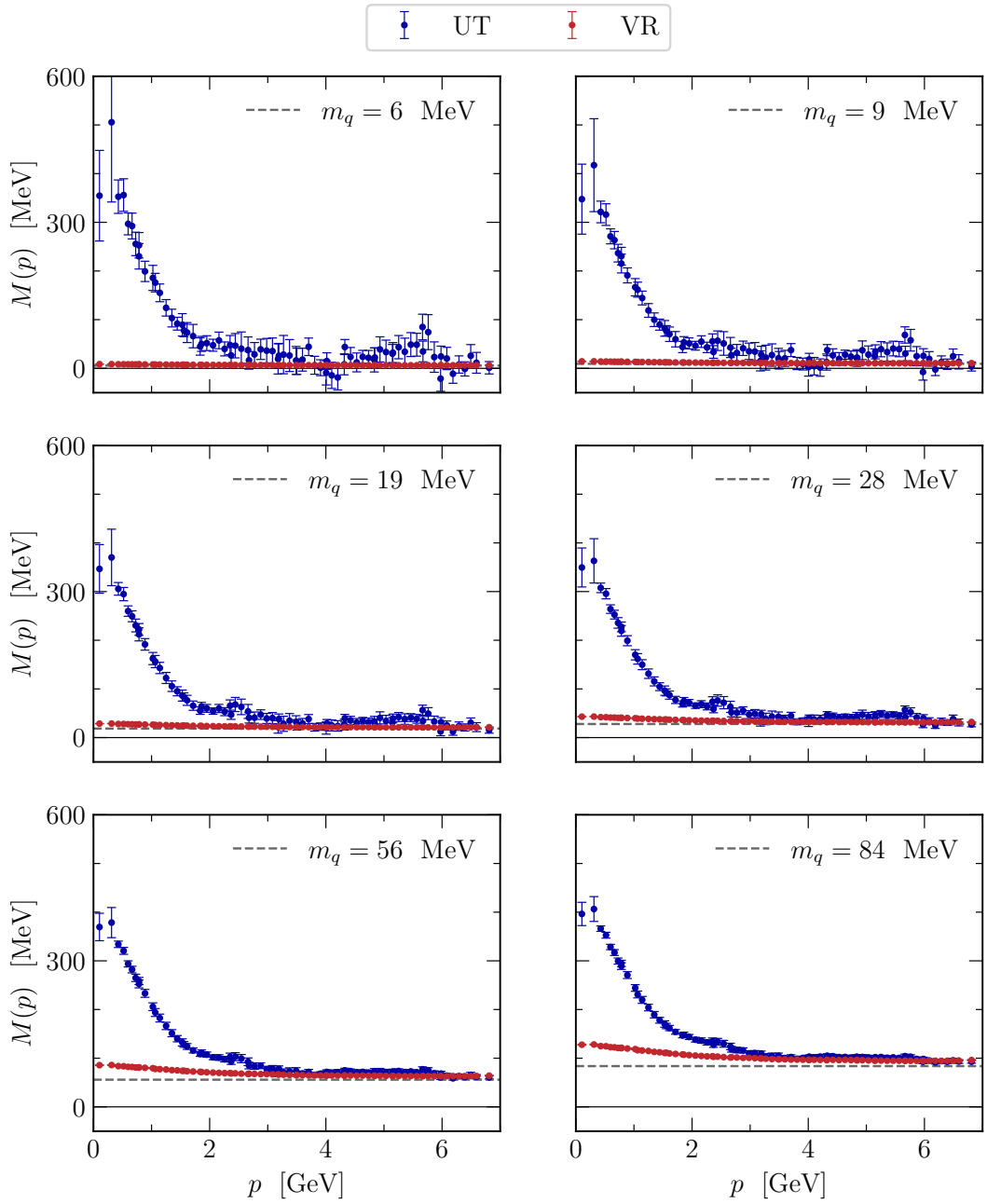

Figure 8.1: Untouched (blue) and vortex-removed (red) mass functions $M(p)$ for all quark masses considered.

untouched and vortex-removed renormalisation functions in the pure-gauge sector are also in agreement for $p < 1$ GeV, this is not so in the dynamical case where the renormalisation function is suppressed upon vortex removal. The novelty of this result, and the decreasing severity of the suppression with increasing quark mass as seen in Figure 8.2 is unsurprising when considered in light of the mass function

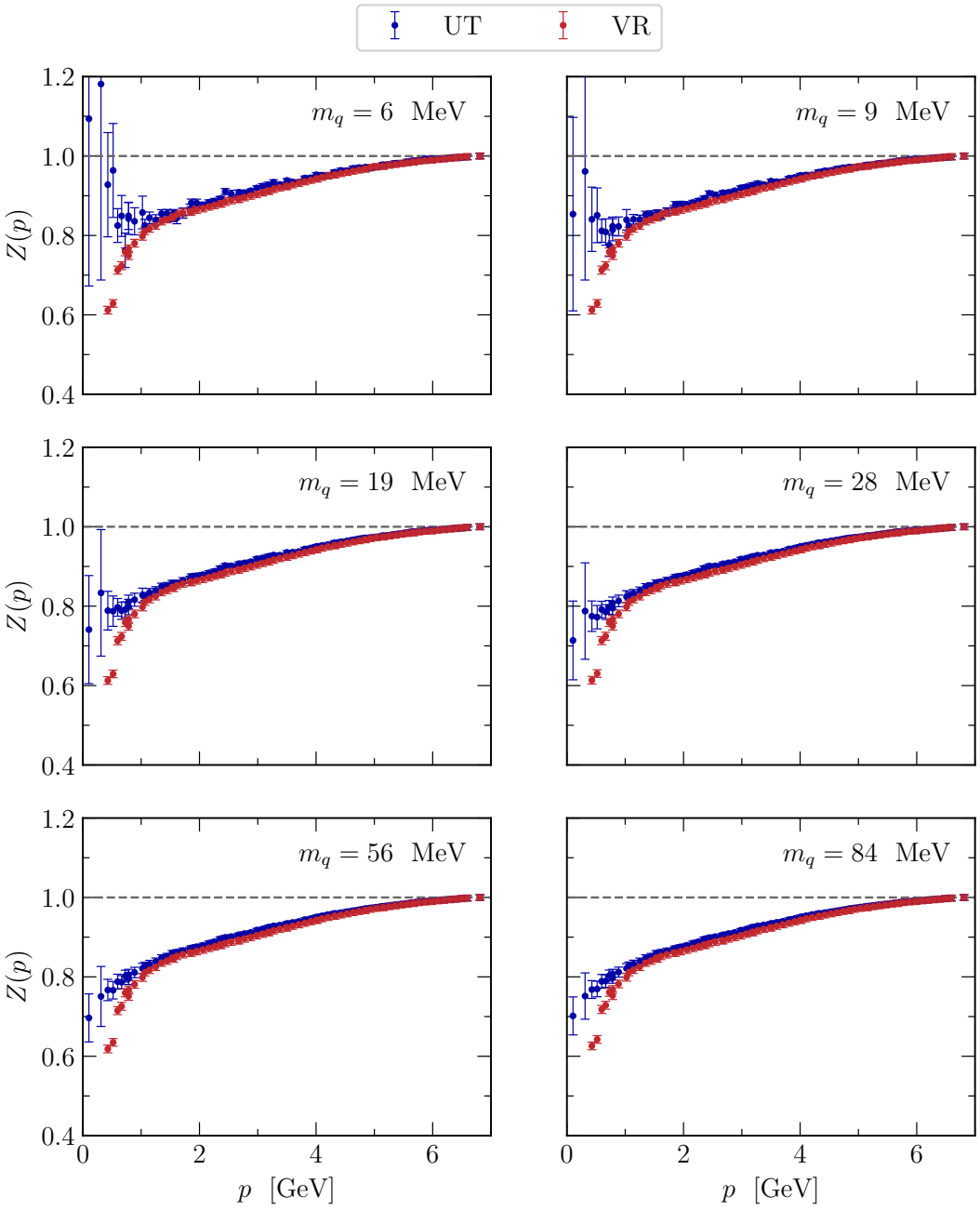

Figure 8.2: Untouched (blue) and vortex-removed (red) renormalisation functions $Z(p)$ for all masses considered.

results. Since dynamical mass generation vanishes at the lightest masses

$$M(p) \approx 0 \quad \forall\, p\,, \tag{8.1}$$

and

$$q \to 0 \text{ as } p \to 0\,, \tag{8.2}$$

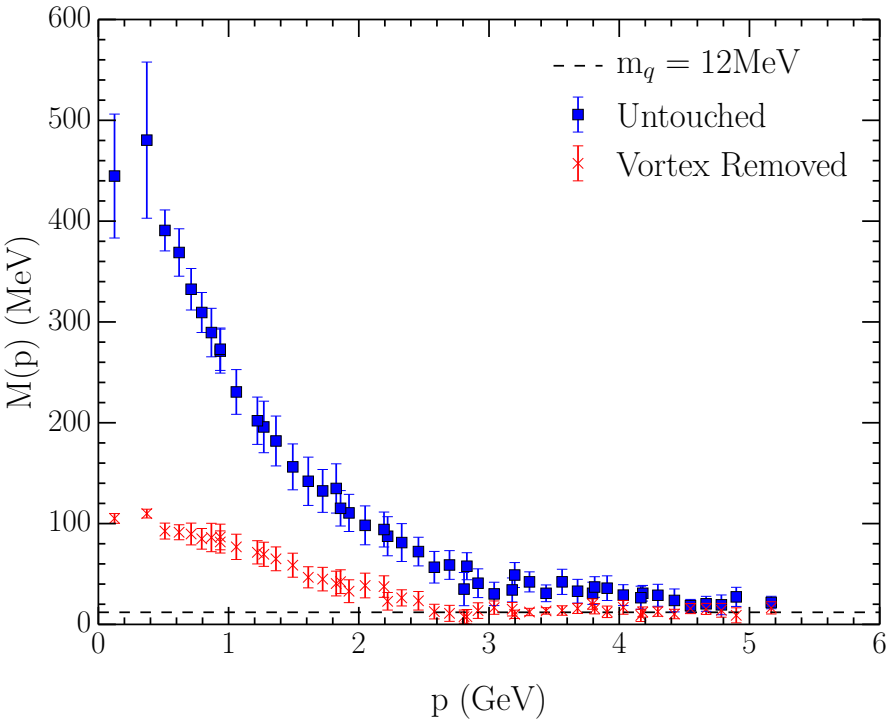

(a)

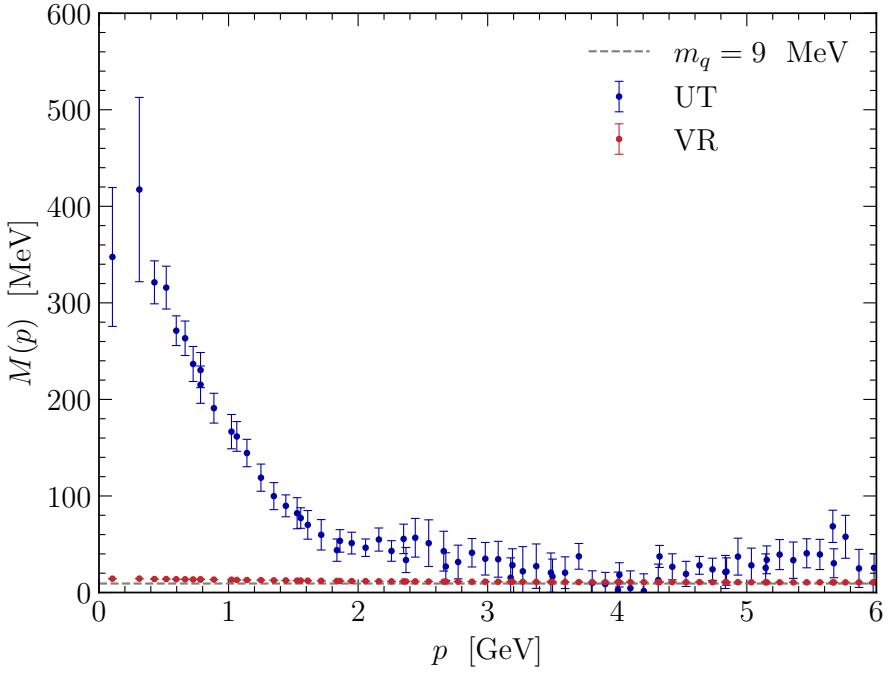

(b)

Figure 8.3: Comparison of mass functions from Ref. [99] in pure-gauge for $m_q = 12$ MeV (a), and this study for $m_q = 9$ MeV (b). While 12 MeV is the lightest available mass from Ref. [99], 9 MeV is the closest mass in the current study.

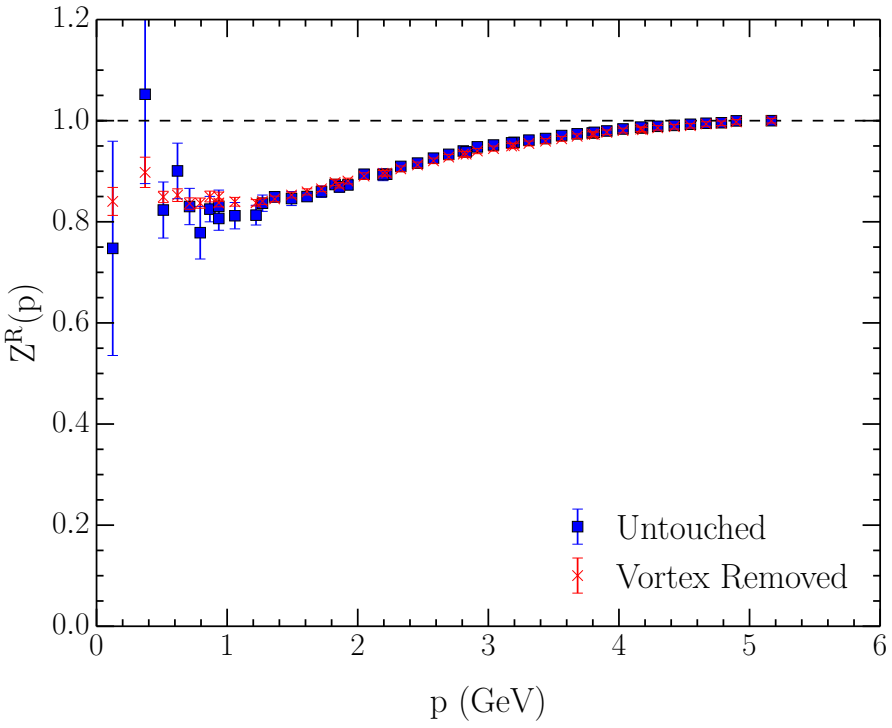

(a)

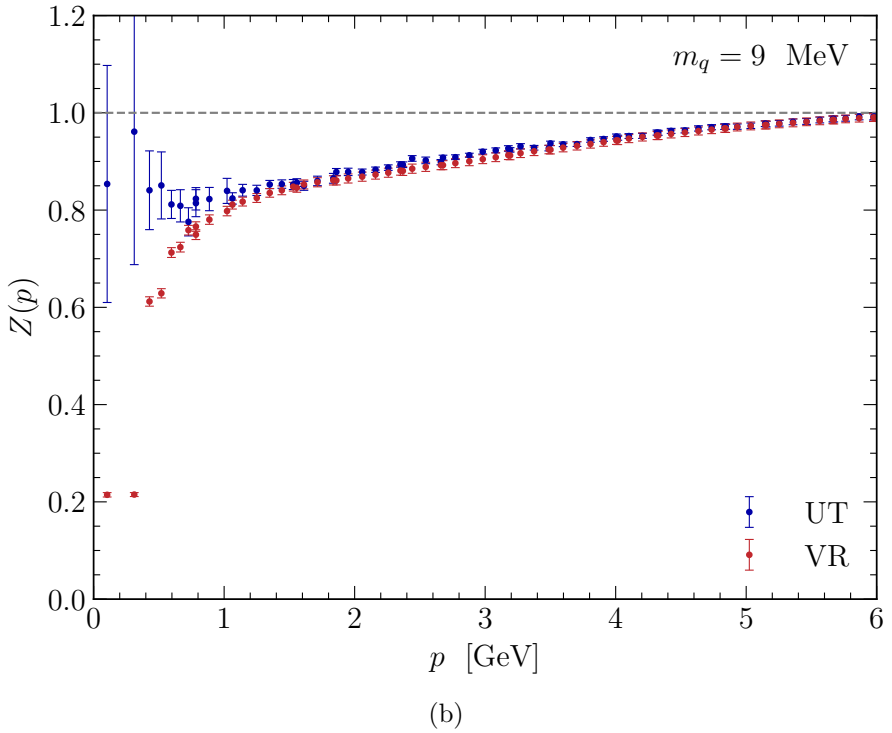

(b)

Figure 8.4: Comparison of renormalisation functions from Ref. [99] in pure-gauge for $m_q = 12$ MeV (a), and this study for $m_q = 9$ MeV (b). While 12 MeV is the lightest available mass from Ref. [99], 9 MeV is the closest mass in the current study.

it must be that

$$Z(p) \to 0 \text{ as } p \to 0\,, \tag{8.3}$$

to ensure

$$S(p) = \frac{Z(p)}{i\not{q} + M(p)}\,, \tag{5.5}$$

remains finite. In the pure-gauge sector, the imperfect removal of dynamical mass generation removes the restriction of $Z(p) \to 0$ as $p \to 0$. Analogously, the reduced suppression at larger quark masses seen in the dynamical results can be seen as a consequence of the greater prominence of remnant dynamical mass generation in the mass function associated with the greater degree of explicit chiral symmetry breaking.

8.3 Vortex-Only Quark Propagator

Given the remarkable results of the vortex-removed quark propagator, it is naturally of interest to consider the Landau-gauge overlap quark propagator on a vortex-only background in dynamical QCD. To compute the overlap quark propagator, the vortex-only background must be smoothed to ensure it satisfies the smoothness condition which guarantees the exponential locality of the overlap Dirac operator. In Chapter 7 we developed three approaches to this end. Initially, we shall compute the quark propagator on four respective vortex-only ensembles smoothed by each of these approaches, and in addition, three-loop $\mathcal{O}(a^4)$-improved cooling [169] which was used in the pure-gauge studies of Refs. [99, 168]. As well as serving as an initial investigation into the vortex-only quark propagator in dynamical QCD, it also provides insight into any benefits or drawbacks of the various smoothing regimes which may exist. This could potentially aid the selection of a single approach to use in a definitive high-statistics calculation for comparison with the untouched propagator of Chapter 5.

8.3.1 Simulation parameters

We start with the same $32^3 \times 64$ PACS-CS 2+1-flavour ensemble [64] used in Chapter 5, from which we obtain a Z(3) vortex-only gauge field ensemble as outlined in Section 7.1. This vortex-only ensemble is then smoothed by each of the respective algorithms developed in Chapter 7, and with $\mathcal{O}(a^4)$-improved cooling, such that we obtain four distinct smoothed vortex-only ensembles. The respective algorithms are outlined in Table 8.1.

Table 8.1: Summary of smoothing recipes. Steps are applied from left to right starting with the Z(3) center-vortex configuration in MCG. C indicates centrifuge preconditioning with rotation angle ω. R indicates the application of a random gauge transformation. N indicates the number of sweeps of cooling (CL) or AUS at smearing parameter α. V indicates if a vortex-preservation step was included in the AUS smearing.

Algorithm	C	ω	R	N	α	V
CL	×	-	×	10	-	×
AS	×	-	✓	20	0.7	×
CP	✓	0.02	✓	1190	0.02	×
VP	✓	0.02	✓	1190	0.02	✓

We compute the quark propagator as per Chapter 5, however with a different choice of kernel. Whereas previously we chose $H = \gamma^5 D_{\text{fllic}}$, here we choose $H = \gamma^5 D_{\text{clover}}$. The additional smearing in the kernel provided by D_{fllic} offers little-to-no benefit on these already-smoothed vortex-only gauge field ensembles. For the same reason, in contrast to Chapter 5, we also elect to not use mean-field improvement as the mean link of these ensembles $u_0 \approx 1.00$. For optimal computational efficiency, we choose to project out the 150 lowest-lying eigenmodes, and set the Wilson mass parameter to the canonical value $am_w = -1.0$, corresponding to a hopping parameter of $\kappa = 0.16667$ in the kernel and quark masses $m_q = 5$, 8, 17, 25, 51, 76 MeV.

8.3.2 Results

The mass functions from each respective ensemble are plotted together in Figure 8.5, for each quark mass considered. Similarly, the respective renormalisation functions are presented in Figure 8.6.

There are subtle differences between the quark propagators obtained from the various smoothing algorithms. These are most easily observed in the middle to high quark masses, as they are lost in the statistical noise at the lightest quark masses. In the mass function, these differences occur around the peak and in the $p = 2$–5 GeV region, whilst in the renormalisation function they occur in the infrared region.

In an attempt to tease out these differences we consider the correlated differences of the mass and renormalisation functions of each ensemble. We choose the CP ensemble as a consistent baseline since this algorithm most closely approaches the ideal of Wilson flow.

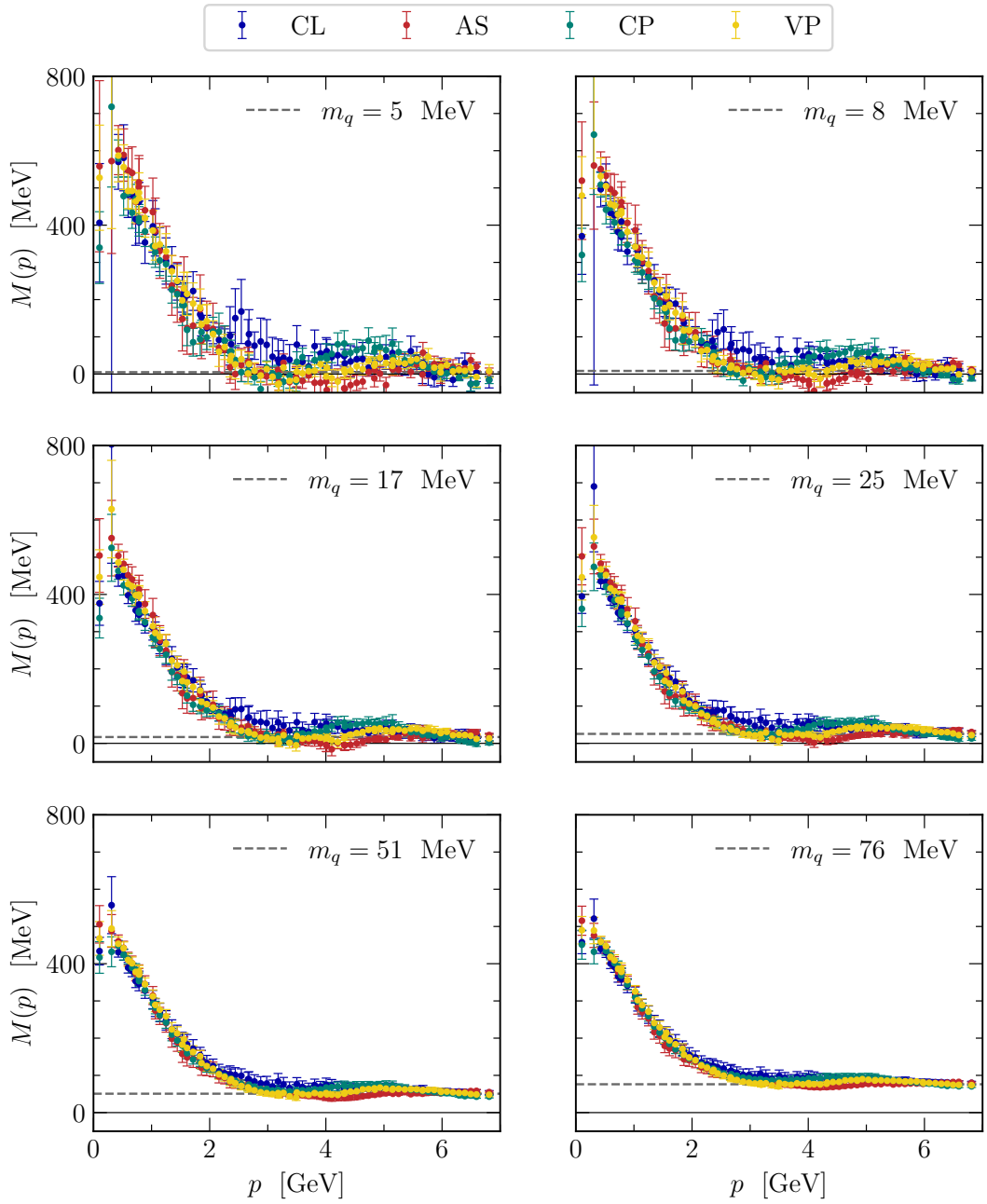

Figure 8.5: Mass functions $M(p)$ for all quark masses considered. Each smoothed vortex-only ensemble contains 30 configurations. The labels for each simulation are defined in Table 8.1.

The correlated differences for the mass and renormalisation functions are presented in Figures 8.7 and 8.8, respectively. The CL renormalisation function is consistent with CP outside a slight deviation in the $p = 1$–2 GeV region where it sits high. Both AS and VP also sit high relative to CP in this region. However, whereas CL shows a downward trend back towards CP for $p < 1$ GeV, AS and VP

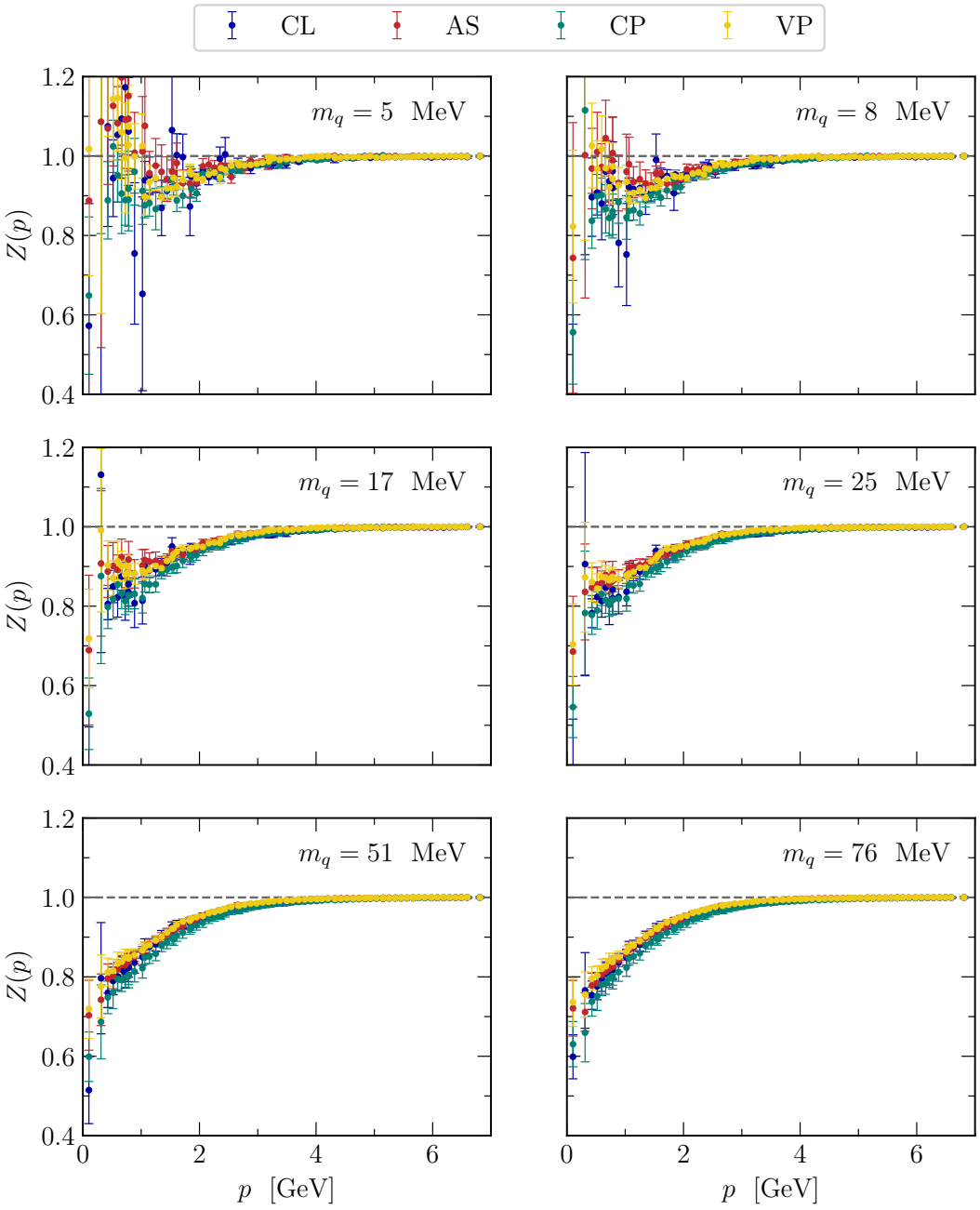

Figure 8.6: Renormalisation functions $Z(p)$ for all quark masses considered. Each smoothed vortex-only ensemble contains 30 configurations. The labels for each simulation are defined in Table 8.1.

appear to continue to diverge on an upward trend away from CP as $p \to 0$. These differences are subtle, however, and are lost in the statistical noise at the smallest momenta and quark masses considered.

The correlated differences in the mass function reaffirm the subtlety of the differences between the respective ensembles. The most prominent feature is in the

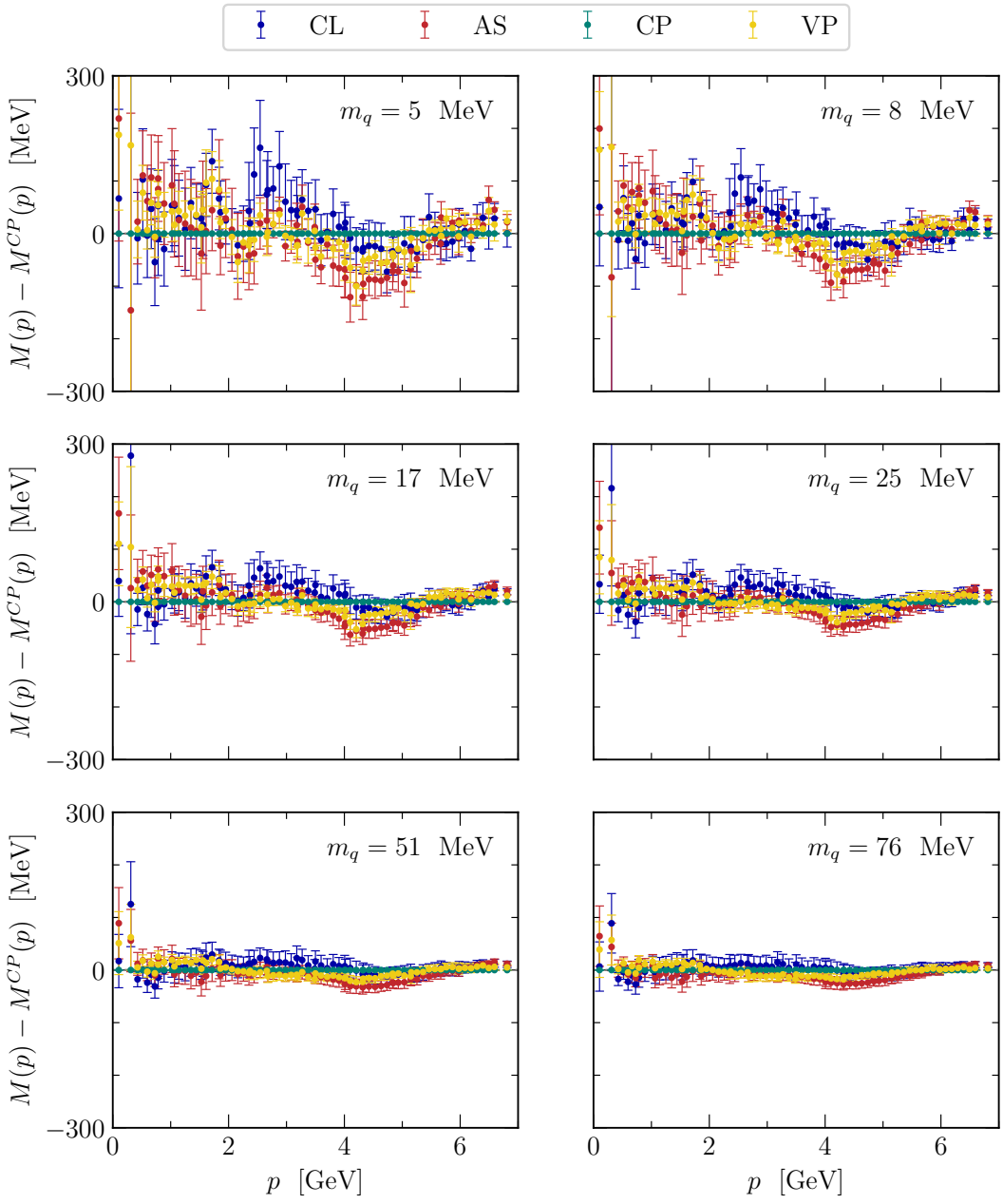

Figure 8.7: The correlated differences between the respective mass function $M(p)$ from each smoothing algorithm and the CP-smoothed mass function $M^{\mathrm{CP}}(p)$.

$p = 4$–5 GeV region where both AS and VP sit low relative to CP. Outside the neighbourhood of this region, AS is otherwise consistent with CP. VP, on the other hand, also sits above CP in the $p = 1$–2 GeV region. Similarly, CL sits high in the $p = 2.5$–3.5 GeV region. Whilst taking the correlated difference we were able to tease out some of the more subtle differences present between the respective ensembles, it is clear that a thorough comparison would require improved statistics.

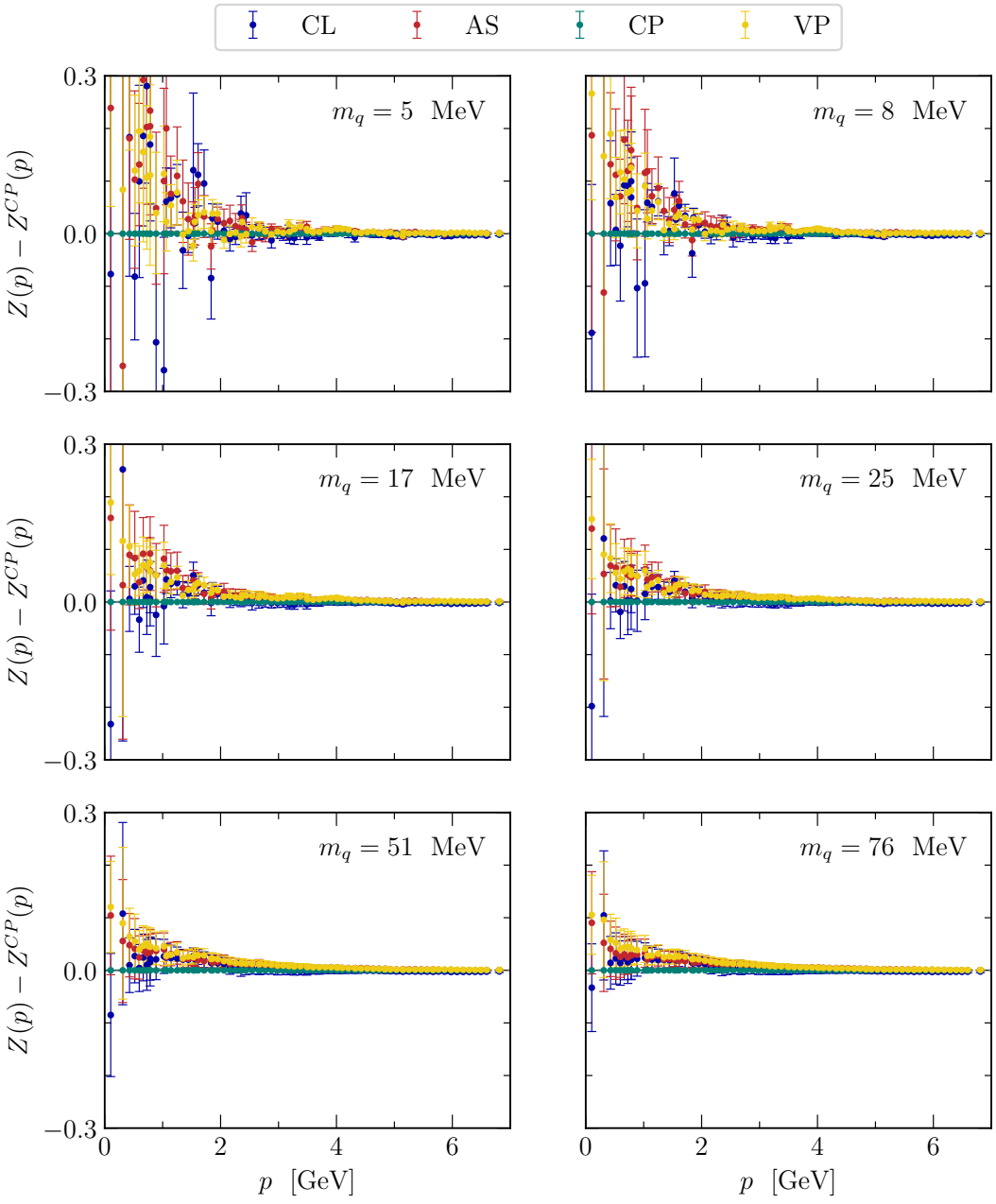

Figure 8.8: The correlated differences between the respective renormalisation function $Z(p)$ from each smoothing algorithm and the CP-smoothed renormalisation function $Z^{\mathrm{CP}}(p)$.

The most notable aspect of these results applies to all ensembles considered and is the much higher than expected peak in the mass function at small p, which is seen neither in the untouched, nor the pure-gauge vortex-only mass function [99, 168]. In this sense, the results of the respective ensembles are broadly similar.

8.4 Comparison of Vortex-Only and Untouched Quark Propagators

We now proceed to compute the vortex-only quark propagator for the purposes of comparison with the untouched propagator of Chapter 5. As there are no striking differences between the quark propagators computed in Section 8.3 for a particular choice of smoothing regime, we choose to employ the CP algorithm as this most closely approaches the ideal of Wilson flow.

8.4.1 Simulation Parameters

The simulation is similar to that of Section 8.3, with some minor differences. Here we consider only the CP-smoothed Z(3) vortex-only gauge field ensemble. We also employ an additional 30 gauge field configurations for improved statistics, for a total of 60. Furthermore, we choose $am_w = -1.1$, corresponding to hopping parameter $\kappa = 0.17241$ in the kernel. This ensures the quark masses match those of of the untouched propagator in Chapter 5, which are $m_q = 6$, 9, 19, 28, 56, 84 MeV.

8.4.2 Results

The CP-smoothed vortex-only mass and renormalisation functions for each quark mass are plotted against the respective untouched counterparts of Chapter 5 in Figures 8.9 and 8.10, respectively.

It is in this direct comparison that the apparent excessive dynamical mass generation in the vortex-only mass function becomes clear. Even against the unsmoothed untouched mass function, the vortex-only mass function sits consistently higher in the region in which dynamical mass generation occurs. This is in contrast to the pure-gauge sector where the dynamical mass generation in the vortex-only mass function matches that of the equivalently-smoothed untouched mass function.

There is a clear peak in the vortex-only mass function at lighter masses, which becomes less prominent with increasing quark mass, ultimately reaching a plateau at the heaviest quark mass. Whilst the height of the peak is mass dependent, the data point at the smallest momentum is independent of valence quark mass. In the untouched case this value is likely governed by the sea quark masses which are treated with the nonperturbatively-improved clover action.

The relative degree of 'excess' dynamical mass generation in the $0.5 < p < 2.5$ increases with decreasing quark mass. The separation between the respective mass

functions shifts rightward with decreasing mass, separating at $p \sim 2$ GeV at the heaviest mass, but closer to $p \sim 2.5$ GeV at the lightest. This is of potential interest given that the quark mass serves as a measure of explicit chiral symmetry breaking.

Meanwhile, the direct comparison of the respective vortex-only and untouched renormalisation functions reveals a divergence between the two. The degree of divergence appears consistent across the different quark masses in the $p = 1.5$–5 GeV range. At all but the heaviest masses, this divergence persists into the infrared with the vortex-only function sitting consistently above the untouched. As such, like the untouched, there is an uptick in the vortex-only function at the lightest masses. However, the minimum prior to the uptick is shifted rightward relative to the untouched, and is less prominent making it more difficult to precisely pinpoint. Like the untouched case, the uptick vanishes at heavier masses, to the point that the respective functions are in agreement in the region at the heaviest mass. For $p > 5$ GeV the respective functions are in agreement.

8.5 Summary

In the pure-gauge sector, a significant remnant of dynamical mass generation in the quark propagator mass function persists upon vortex-removal. This is despite the full reproduction of dynamical mass generation on a vortex-only background. Recent studies of the static quark potential and gluon propagator found that the presence of dynamical fermions resolves similar quantitative discrepancies related to vortex modification in the pure-gauge sector. Motivated by these results, it was investigated whether dynamical fermions could play a similar role in the context of the vortex-modified quark propagator.

To this end, the Landau-gauge overlap quark propagator was computed on a vortex-removed 2+1 dynamical fermion flavour gauge field ensemble. Dynamical mass generation in the mass function vanishes upon vortex removal at the lightest quark mass, demonstrating an absence of dynamical chiral symmetry breaking and resolving the discrepancy present in the pure-gauge sector. Furthermore the quark mass governs the degree to which chiral symmetry is explicitly broken. As the quark mass increases, a remnant of dynamical mass generation emerges and becomes more prominent, but remains small. Within this framework, it is clear that the novel infrared suppression in the renormalisation function upon vortex-removal is necessary for the quark propagator to remain finite.

The Landau-gauge overlap quark propagator was also computed on smoothed centre-vortex ensembles obtained from 2+1-flavour dynamical gauge fields. Respec-

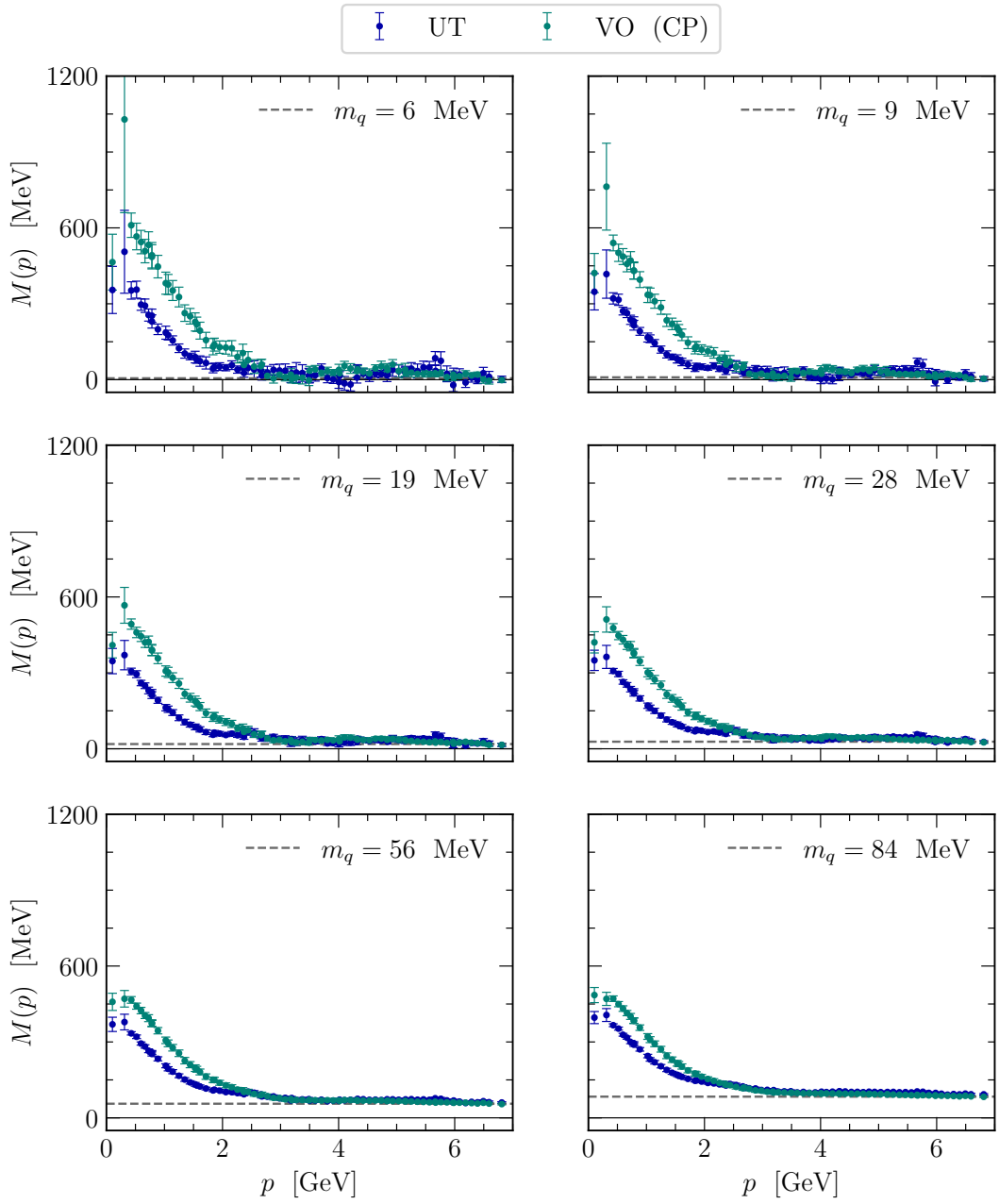

Figure 8.9: The CP-smoothed vortex-only (green) and untouched (blue) mass functions $M(p)$ for all quark masses considered.

tive ensembles were smoothed by each of the recipes developed in Chapter 7, in addition to $\mathcal{O}(a^4)$-improved cooling. For direct comparison with the untouched propagator of Chapter 5, a more precise calculation was performed using the CP smoothing recipe with an additional 30 gauge field configurations for an ensemble total of 60.

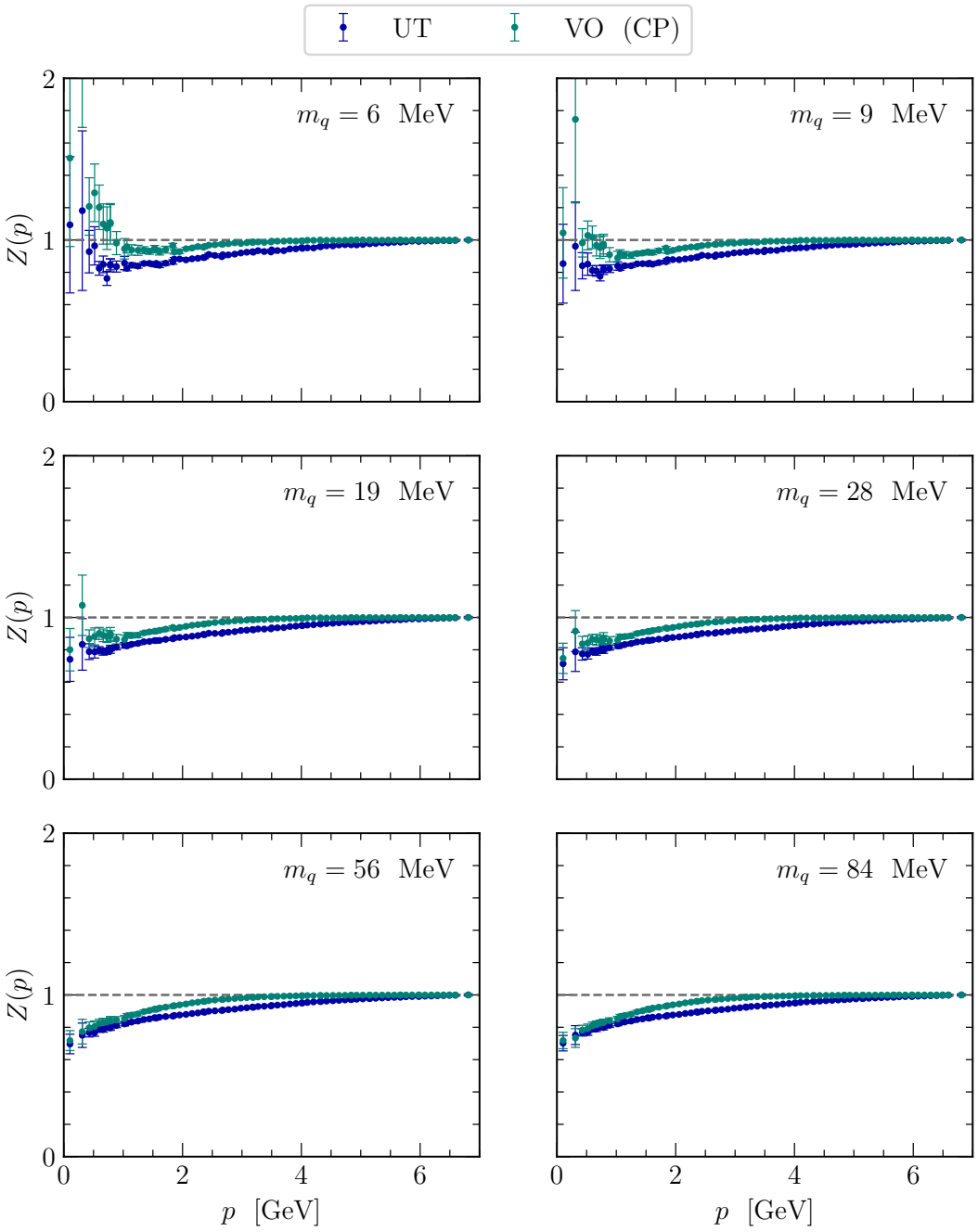

Figure 8.10: The CP-smoothed vortex-only (green) and untouched (blue) renormalisation functions $Z(p)$ for all quark masses considered.

Dynamical mass generation in the mass function is qualitatively reproduced on the vortex-only background, consistent with the pure-gauge sector. Unlike the pure-gauge sector, where the amount of dynamical mass generation on the vortex-only background is consistent with that of an equivalently smoothed untouched background, excess dynamical mass generation is observed in the vortex-only mass func-

tion – even when compared to the unsmoothed untouched mass function. The relative degree of the excess dynamical mass generation appears to have a quark mass dependence, being larger at lighter masses. These results appear to be independent of choice of smoothing algorithm. It is difficult to tease out any subtle differences which may be present between the various smoothing algorithms, especially at lighter masses.

Nevertheless, the presence of dynamical fermions resolves the quantitative discrepancy observed in the pure-gauge vortex-removed quark propagator. The cause and mechanism of the excess dynamical mass generation from the vortex-only background is unknown, and is a topic of further research. Together, these results support an important relationship between dynamical fermions and centre vortices, and further add to the body of evidence supporting centre vortices as the mechanism underpinning dynamical chiral symmetry breaking.

Chapter 9

Summary

Throughout this thesis we made extensive use of overlap fermions. Overlap fermions were developed as a solution to the Ginsparg-Wilson relation which provides an implementation of chiral symmetry on the lattice. In addition to their chiral nature, overlap fermions are also sensitive to the topological structures of the gauge field. They do however, come at significant computational expense relative to Wilson fermions, and therefore their use is typically restricted to situations where these, and other properties are deemed beneficial or necessary.

Overlap fermions are protected from additive renormalisation which makes them an ideal choice for computations of the quark propagator due to the straightforward, prescribed manner in which the mass and renormalisation functions are extracted. In Chapter 5 we computed the Landau-gauge quark propagator from 2+1-flavour dynamical gauge fields for the first time. A plateau at the smallest momenta was observed in the mass function which was independent of valence quark mass, suggesting this behaviour is determined by the sea quarks which were treated with the nonperturbatively-improved clover action. A suggestion of a minimum in the renormalisation function at the lightest masses was observed, consistent with Schwinger-Dyson results which reported similar results in quenched calculations. This observation contrasts results from $\mathcal{O}$(a)-improved Wilson fermions on 2-flavour dynamical backgrounds which observed a peak in the renormalisation function not seen elsewhere. Future investigations which use larger volume lattices, or twisted boundary conditions, would provide better access to smaller nontrivial momenta, enabling confirmation of the behaviours observed in the infrared.

Typically, overlap fermions are not used in hadron spectrum calculations as the explicit breaking of chiral symmetry by the Wilson term is expected to have negligible impact, after the associated additive mass renormalisation is taken into account through the standard pion mass analysis. As such, it is difficult to justify the computational expense of the overlap formalism. It has been suggested, however, that chiral symmetry could be key to understanding the origin of the low-lying

nature of the $N^*(1440)$ Roper resonance. In Chapter 6 we systematically examined the role of chiral symmetry in the low-lying nucleon spectrum by directly comparing the Wilson-type clover fermion action with the overlap fermion action, such that the only difference between respective simulations is the choice of fermion action. We found that the clover and overlap fermion actions show a remarkable level of agreement, and do not find any evidence that chiral symmetry in the fermion action plays a significant role in understanding the Roper resonance on the lattice.

Where the use of overlap fermions is important, not only due to their chiral nature, but also their sensitivity to topological structures of the gauge field, is in the study of the role of centre vortices in the nonperturbative aspects of QCD, particularly dynamical chiral symmetry breaking. Before proceeding to consider the impact of vortex-modification on the Landau-gauge quark propagator in dynamical QCD, it was necessary to investigate viable approaches to smoothing the rough centre-vortex gauge field configurations. This was to ensure the smoothness condition of the overlap Dirac operator was satisfied, and by extension its locality guaranteed. In Chapter 7 we developed three viable recipes to this end, where both *centrifuge preconditioning*, and *vortex-preserved annealed smoothing* were introduced to overcome the limited applicability and shortcomings of typical SU(3) gauge field smoothing algorithms.

In Chapter 8 we considered the impact of vortex modification on the Landau-gauge overlap quark propagator. We found that the dynamical mass generation in the mass function vanishes upon vortex removal at the lightest quark mass considered, resolving the quantitative discrepancy present in the pure-gauge sector.

We also computed the Landau-gauge overlap quark propagator on smoothed vortex-only ensembles. Respective ensembles were smoothed by each of the recipes developed in Chapter 7, in addition to cooling. Taking the correlated difference between the respective smoothing algorithms for both the mass and renormalisation functions, we were able to tease out some subtle differences between the algorithms. However, a thorough comparison requires improved statistics. We then chose the CP algorithm to perform a direct comparison with the results of the untouched propagator of Chapter 5 with improved statistics. The qualitative features of the mass function were reproduced from the vortex-only background. Interestingly, the degree of dynamical mass generation was much higher than in the untouched case. The qualitative aspects of these results were independent of the smoothing algorithms considered. Together, these results lend further credence to the existence of an important relationship between dynamical fermions and centre vortices, and

provide further evidence for centre vortices underpinning dynamical chiral symmetry breaking.

Appendix A

Supplementary Material

A.1 Derivation of Eq. (3.54)

Starting with Eq. (3.52)

$$P_{\mu\nu}(x) = \exp\{-iagA_\mu(x)\}\exp\{-iagA_\nu(x+\hat{\mu})\} \times \exp\{iagA_\mu(x+\hat{\nu})\}\exp\{iagA_\nu(x+\hat{\nu})\} \quad (3.52)$$

and applying the Baker-Campbell-Hausdorf formula up to first order in the commutator

$$\exp(A)\exp(B) = \exp\left(A + B + \frac{1}{2}[A\,,B] + ...\right) \quad (3.53)$$

we have

$$\begin{aligned} P_{\mu\nu}(x) &= \exp\left\{-iagA_\mu(x) - iagA_\nu(x+\hat{\mu}) - \frac{a^2g^2}{2}[A_\mu(x)\,,A_\nu(x+\hat{\mu})]\right\} \\ &\quad \times \exp\left\{iagA_\mu(x+\hat{\nu}) + iagA_\nu(x) - \frac{a^2g^2}{2}[A_\mu(x+\hat{\nu})\,,A_\nu(x)]\right\} \\ &= \exp\left\{-iagA_\mu(x) - iagA_\nu(x+\hat{\mu}) - \frac{a^2g^2}{2}[A_\mu(x)\,,A_\nu(x+\hat{\mu})]\right. \\ &\quad + iagA_\mu(x+\hat{\nu}) + iagA_\nu(x) - \frac{a^2g^2}{2}[A_\mu(x+\hat{\nu})\,,A_\nu(x)] \\ &\quad + \frac{a^2g^2}{2}([A_\mu(x), A_\mu(x+\hat{\nu})] + [A_\mu(x)\,,A_\nu(x)] \\ &\quad \left. + [A_\nu(x+\hat{\mu}), A_\mu(x+\hat{\nu})] + [A_\nu(x+\hat{\mu})\,,A_\nu(x)]) + \mathcal{O}(a^3)\right\}. \end{aligned} \quad (A.1)$$

Taylor expanding the gauge vector fields up to terms of $\mathcal{O}(a)$ such that

$$A_\mu(x+\hat{\nu}) = A_\mu(x) + a\partial_\mu A_\nu(x) + \mathcal{O}(a^2)\,, \quad (A.2)$$

the each term from the exponent of Eq. (A.1) becomes

$$
\begin{aligned}
&- \cancel{iagA_\mu(x)} \\
&- iag\left\{\cancel{A_\nu(x)} + a\partial_\mu A_\nu(x)\right\} \\
&- \frac{a^2g^2}{2}\left[A_\mu(x)\,, A_\nu(x)\right] + \mathcal{O}(a^3) \\
&+ iag\left\{\cancel{A_\mu(x)} + a\partial_\nu A_\mu(x)\right\} \\
&+ \cancel{iagA_\nu(x)} \\
&- \frac{a^2g^2}{2}\left[A_\mu(x)\,, A_\nu(x)\right] + \mathcal{O}(a^3) \\
&+ \frac{a^2g^2}{2}\cancelto{0}{\left[A_\mu(x)\,, A_\mu(x)\right]} + \mathcal{O}(a^3) \\
&+ \frac{a^2g^2}{2}\cancel{\left[A_\mu(x)\,, A_\nu(x)\right]} + \mathcal{O}(a^3) \\
&+ \frac{a^2g^2}{2}\cancel{\left[A_\mu(x)\,, A_\mu(x)\right]} + \mathcal{O}(a^3) \\
&+ \frac{a^2g^2}{2}\cancelto{0}{\left[A_\nu(x)\,, A_\nu(x)\right]} + \mathcal{O}(a^3)
\end{aligned}
\tag{A.3}
$$

where terms have been cancelled. Hence, the exponent is given by

$$
\begin{aligned}
&- ia^2g\left\{\partial_\mu A_\nu(x) - \partial_\nu(x)A_\mu(x)\right\} - a^2g^2\left[A_\mu(x)\,, A_\nu(x)\right] + \mathcal{O}(a^3) \\
&= - ia^2g\left\{\partial_\mu A_\nu(x) - \partial_\nu(x)A_\mu(x) - ig\left[A_\mu(x)\,, A_\nu(x)\right]\right\} + \mathcal{O}(a^3) \\
&= - ia^2g\left\{\partial_\mu A^a_\nu(x)t^a - \partial_\nu(x)A^a_\mu(x)t^a - ig\left[A^b_\mu(x)t^b\,, A^c_\nu(x)t^c\right]\right\} + \mathcal{O}(a^3) \\
&= - ia^2g\left\{\partial_\mu A^a_\nu(x)t^a - \partial_\nu(x)A^a_\mu(x)t^a - ig\left[t^b\,, t^c\right]A^b_\mu(x)A^c_\nu(x)\right\} + \mathcal{O}(a^3) \\
&= - ia^2g\left\{\partial_\mu A^a_\nu(x)t^a - \partial_\nu(x)A^a_\mu(x)t^a + gf^{bca}t^aA^b_\mu(x)A^c_\nu(x)\right\} + \mathcal{O}(a^3) \\
&= - ia^2g\left\{\partial_\mu A^a_\nu(x) - \partial_\nu(x)A^a_\mu(x) + gf^{abc}A^b_\mu(x)A^c_\nu(x)\right\}t^a + \mathcal{O}(a^3) \\
&= - ia^2gF^a_{\mu\nu}(x)t^a + \mathcal{O}(a^3)\,,
\end{aligned}
\tag{A.4}
$$

and therefore

$$
P_{\mu\nu}(x) = \exp\left\{-ia^2gF_{\mu\nu}(x) + \mathcal{O}(a^3)\right\}\,. \tag{A.5}
$$

A.2 Derivation of $\alpha_{\mathbf{min}}$ for MaxReTr Reuniterization Within the Over-Improvement Formalism

Without loss of generality, let $Z_\mu(x) = \mathbb{1}$. Hence, L^1 from equation (7.55) becomes

$$L^1 = (1-\alpha) + \frac{\alpha}{6}\Sigma^\dagger_\mu(x)\,, \tag{A.6}$$

which explicitly within the over-improvement formalism is

$$L^1 = (1-\alpha) + \frac{\alpha}{6}\left\{\left(\frac{5-2\epsilon}{3}\right)S_\mu(x) + \left(\frac{\epsilon-1}{12u_0^2}\right)R_\mu(x)\right\}\,, \tag{A.7}$$

where $S_\mu(x)$ represents the 3-link staple terms and $R_\mu(x)$ represents the 5-link rectangle terms in Eq. (7.53). We restrict the over-improvement term such that $\epsilon \in \left[-\frac{5}{2}, 1\right]$ to ensure

$$\frac{5-2\epsilon}{3} \geqslant 0\,, \tag{A.8}$$

and

$$\frac{\epsilon-1}{12u_0^2} \leqslant 0\,. \tag{A.9}$$

Then, the minima of the real component of $L^1\left[\Sigma_\mu(x)\right]$ for a given α occur when all 6 terms contributing to $S_\mu(x)$ have nontrivial phase (and hence a real component equal to -0.5). Replacing any term with the identity necessarily increases the real component of $S_\mu(x)$. Hence, the values of $S_\mu(x)$ for which the real component of L^1 is minimized are given by

$$\begin{aligned} S_\mu(x) &= ne^{+i\frac{2\pi}{3}} + (6-n)e^{-i\frac{2\pi}{3}} \\ &= 6\cos\left(\frac{2\pi}{3}\right) + i(2n-6)\sin\left(\frac{2\pi}{3}\right) \\ &= -3 + i(2n-6)\sin\left(\frac{2\pi}{3}\right) \end{aligned} \tag{A.10}$$

where $n \in [0,6] \subset \mathbb{Z}$. As we are not concerned with the imaginary component, for simplicity and without loss of generality we take $n = 3$ for which the imaginary component of $S_\mu(x)$ vanishes. Evaluating $S_\mu(x)$ for $n = 3$, we have $S_\mu(x) = -3$.

On the other hand, as the factor in front of $R_\mu(x)$ is negative, the minima of L^1 for a given α occur when the real component of $R_\mu(x)$ is maximized. This occurs when all 18 loops contributing to $R_\mu(x)$ are the identity with real component equal

to 1. Replacing any term with one which has nontrivial phase (and hence real component equal to -0.5) necessarily reduces the real component of $R_\mu(x)$. Hence, the minima of L^1 must occur when $R_\mu(x) = 18$.

Substituting into equation (A.7) we have

$$L^1 = (1-\alpha) + \frac{\alpha}{6}\left\{\left(\frac{5-2\epsilon}{3}\right)(-3) + \left(\frac{\epsilon-1}{12u_0^2}\right)(18)\right\}. \tag{A.11}$$

Recalling that we require $\operatorname{Re} L^1 < 0$, and simplifying we have

$$\begin{aligned}
0 &> (1-\alpha) + \frac{\alpha}{6}\left\{\left(\frac{5-2\epsilon}{3}\right)(-3) + \left(\frac{\epsilon-1}{12u_0^2}\right)(18)\right\} \\
0 &> 1-\alpha+\alpha\left\{\frac{2\epsilon-5+\frac{3}{2}\left(\frac{\epsilon-1}{u_0^2}\right)}{6}\right\} \\
-1 &> \alpha\left\{\frac{2\epsilon-11+\frac{3}{2}\left(\frac{\epsilon-1}{u_0^2}\right)}{6}\right\} \\
\alpha &> \frac{-6}{2\epsilon-11+\frac{3}{2}\left(\frac{\epsilon-1}{u_0^2}\right)}.
\end{aligned} \tag{A.12}$$

Let $\Sigma_\mu^{\min}(x)$ denote a staples term which minimizes the real component of L^1 for $Z_\mu(x) = \mathbb{1}$. Then, for $Z_\mu(x) = e^{\pm i\frac{2\pi}{3}}$ the minima of the real component of L^1 occur at $e^{\mp i\frac{2\pi}{3}}\Sigma_\mu^{\min}(x)$, and the same derivation follows.

A.3 Generators of SU(3)

The eight traceless anti-Hermitian matrices T^a are the generators of SU(3), and are proportional to the Gell-Mann matrices. In Chapter 7 we choose the normalisation condition $\operatorname{Tr}\left[T^a T^b\right] = -\frac{1}{2}\delta^{ab}$ to ensure the structure constants f^{abc} defined by $\left[T^a, T^b\right] = f^{abc}T^c$ are real and totally antisymmetric in the indices.

Up to a centre phase factor, the diagonal subgroup of SU(3) is spanned by the subset of generators $\{T^3, T^8\}$, where T^3 and T^8 are diagonal. We can write an element of the diagonal subgroup as

$$\exp\left(n\frac{2\pi i}{3}\right)\exp\left(a_3T^3 + a_8T^8\right), \tag{A.13}$$

where $n \in \{-1, 0, 1\}$, and $a_3, a_8 \in \mathbb{R}$. The subgroup is Abelian as $[T^3, T^8] = 0$, and it is straightforward to see that it is isomorphic to $\mathrm{U}(1) \times \mathrm{U}(1) \times \mathrm{Z}(3)$.

Bibliography

[1] K. G. Wilson, "Confinement of Quarks," *Phys. Rev. D* **10** (1974) 2445–2459.

[2] O. Oliveira, P. J. Silva, J.-I. Skullerud, and A. Sternbeck, "Quark propagator with two flavors of O(a)-improved Wilson fermions," *Phys. Rev. D* **99** no. 9, (2019) 094506, arXiv:1809.02541 [hep-lat].

[3] K.-F. Liu, "Baryons and Chiral Symmetry," *Int. J. Mod. Phys. E* **26** no. 01n02, (2017) 1740016, arXiv:1609.02572 [hep-ph].

[4] J. C. Biddle, W. Kamleh, and D. B. Leinweber, "Static quark potential from center vortices in the presence of dynamical fermions," *Phys. Rev. D* **106** no. 5, (2022) 054505, arXiv:2206.00844 [hep-lat].

[5] J. C. Biddle, W. Kamleh, and D. B. Leinweber, "Impact of dynamical fermions on the center vortex gluon propagator," *Phys. Rev. D* **106** no. 1, (2022) 014506, arXiv:2206.02320 [hep-lat].

[6] C. Burgess and G. Moore, *The Standard Model: A Primer*. Cambridge University Press, 2006.

[7] S. Weinberg, *The Quantum Theory of Fields*, vol. 1. Cambridge University Press, 1995.

[8] M. E. Peskin and D. V. Schroeder, *An Introduction to Quantum Field Theory, Student Economy Edition*. CRC Press, 2016.

[9] S. Weinberg, *The Quantum Theory of Fields*, vol. 2. Cambridge University Press, 1996.

[10] W. Siegel, *Fields*. 1999. arXiv:hep-th/9912205.

[11] C. Gattringer and C. B. Lang, *Quantum Chromodynamics on the Lattice*. Springer Berlin, Heidelberg, 2010.

[12] N. Metropolis, A. W. Rosenbluth, M. N. Rosenbluth, A. H. Teller, and E. Teller, "Equation of state calculations by fast computing machines," *J. Chem. Phys.* **21** (1953) 1087–1092.

[13] W. K. Hastings, "Monte Carlo Sampling Methods Using Markov Chains and Their Applications," *Biometrika* **57** (1970) 97–109.

[14] D. J. E. Callaway and A. Rahman, "Lattice Gauge Theory in Microcanonical Ensemble," *Phys. Rev. D* **28** (1983) 1506.

[15] H. B. Nielsen and M. Ninomiya, "Absence of Neutrinos on a Lattice. 1. Proof by Homotopy Theory," *Nucl. Phys. B* **185** (1981) 20. [Erratum: Nucl.Phys.B 195, 541 (1982)].

[16] H. B. Nielsen and M. Ninomiya, "No Go Theorem for Regularizing Chiral Fermions," *Phys. Lett. B* **105** (1981) 219–223.

[17] H. B. Nielsen and M. Ninomiya, "Absence of Neutrinos on a Lattice. 2. Intuitive Topological Proof," *Nucl. Phys. B* **193** (1981) 173–194.

[18] P. H. Ginsparg and K. G. Wilson, "A Remnant of Chiral Symmetry on the Lattice," *Phys. Rev. D* **25** (1982) 2649.

[19] R. Narayanan and H. Neuberger, "Infinitely many regulator fields for chiral fermions," *Phys. Lett. B* **302** (1993) 62–69, `arXiv:hep-lat/9212019`.

[20] R. Narayanan and H. Neuberger, "Chiral determinant as an overlap of two vacua," *Nucl. Phys. B* **412** (1994) 574–606, `arXiv:hep-lat/9307006`.

[21] R. Narayanan and H. Neuberger, "Chiral fermions on the lattice," *Phys. Rev. Lett.* **71** no. 20, (1993) 3251, `arXiv:hep-lat/9308011`.

[22] R. Narayanan and H. Neuberger, "A Construction of lattice chiral gauge theories," *Nucl. Phys. B* **443** (1995) 305–385, `arXiv:hep-th/9411108`.

[23] H. Neuberger, "Exactly massless quarks on the lattice," *Phys. Lett. B* **417** (1998) 141–144, `arXiv:hep-lat/9707022`.

[24] Y. Kikukawa and H. Neuberger, "Overlap in odd dimensions," *Nucl. Phys. B* **513** (1998) 735–757, `arXiv:hep-lat/9707016`.

[25] W. Kamleh, D. H. Adams, D. B. Leinweber, and A. G. Williams, "Accelerated overlap fermions," *Phys. Rev. D* **66** (Jul, 2002) 014501, `arXiv:hep-lat/0112041`. `https://link.aps.org/doi/10.1103/PhysRevD.66.014501`.

[26] W. Bietenholz, "Convergence rate and locality of improved overlap fermions," *Nucl. Phys. B* **644** (2002) 223–247, arXiv:hep-lat/0204016.

[27] T. G. Kovacs, "Locality and topology with fat link overlap actions," *Phys. Rev. D* **67** (2003) 094501, arXiv:hep-lat/0209125.

[28] T. A. DeGrand and S. Schaefer, "Physics issues in simulations with dynamical overlap fermions," *Phys. Rev. D* **71** (2005) 034507, arXiv:hep-lat/0412005.

[29] S. Durr, C. Hoelbling, and U. Wenger, "Physics prospects of UV-filtered overlap quarks," *Nucl. Phys. B Proc. Suppl.* **153** (2006) 82–89, arXiv:hep-lat/0511046.

[30] S. Durr and C. Hoelbling, "Continuum physics with quenched overlap fermions," *Phys. Rev. D* **72** (2005) 071501, arXiv:hep-ph/0508085.

[31] W. Bietenholz and S. Shcheredin, "Overlap hypercube fermions in QCD simulations near the chiral limit," *Nucl. Phys. B* **754** (2006) 17–47, arXiv:hep-lat/0605013.

[32] J. M. Zanotti, S. O. Bilson-Thompson, F. D. R. Bonnet, P. D. Coddington, D. B. Leinweber, A. G. Williams, J. B. Zhang, W. Melnitchouk, and F. X. Lee, "Hadron masses from novel fat link fermion actions," *Phys. Rev. D* **65** (2002) 074507, arXiv:hep-lat/0110216.

[33] C. Morningstar and M. Peardon, "Analytic smearing of su(3)link variables in lattice qcd," *Phys. Rev. D* **69** no. 5, (Mar, 2004) 054501, arXiv:hep-lat/0311018. http://dx.doi.org/10.1103/PhysRevD.69.054501.

[34] B. Sheikholeslami and R. Wohlert, "Improved Continuum Limit Lattice Action for QCD with Wilson Fermions," *Nucl. Phys. B* **259** (1985) 572.

[35] P. Hernandez, K. Jansen, and M. Luscher, "Locality properties of Neuberger's lattice Dirac operator," *Nucl. Phys. B* **552** (1999) 363–378, arXiv:hep-lat/9808010.

[36] H. Neuberger, "Bounds on the Wilson Dirac operator," *Phys. Rev. D* **61** (2000) 085015, arXiv:hep-lat/9911004.

[37] R. G. Edwards, U. M. Heller, and R. Narayanan, "A Study of practical implementations of the overlap Dirac operator in four-dimensions," *Nucl. Phys. B* **540** (1999) 457–471, arXiv:hep-lat/9807017.

[38] T.-W. Chiu, T.-H. Hsieh, C.-H. Huang, and T.-R. Huang, "A Note on the Zolotarev optimal rational approximation for the overlap Dirac operator," *Phys. Rev. D* **66** (2002) 114502, arXiv:hep-lat/0206007.

[39] B. Jegerlehner, "Krylov space solvers for shifted linear systems," arXiv:hep-lat/9612014.

[40] A. Virgili, W. Kamleh, and D. Leinweber, "Overlap quark propagator near the physical pion mass," arXiv:2209.14864 [hep-lat].

[41] H. Neuberger, "Vector - like gauge theories with almost massless fermions on the lattice," *Phys. Rev. D* **57** (1998) 5417–5433, arXiv:hep-lat/9710089.

[42] D. Becirevic, V. Lubicz, G. Martinelli, and M. Testa, "Quark masses and renormalization constants from quark propagator and three point functions," *Nucl. Phys. B Proc. Suppl.* **83** (2000) 863–865, arXiv:hep-lat/9909039.

[43] D. Becirevic, V. Gimenez, V. Lubicz, and G. Martinelli, "Light quark masses from lattice quark propagators at large momenta," *Phys. Rev. D* **61** (2000) 114507, arXiv:hep-lat/9909082.

[44] J. I. Skullerud and A. G. Williams, "Quark propagator in Landau gauge," *Phys. Rev. D* **63** (2001) 054508, arXiv:hep-lat/0007028.

[45] J. Skullerud, D. B. Leinweber, and A. G. Williams, "Nonperturbative improvement and tree level correction of the quark propagator," *Phys. Rev. D* **64** (2001) 074508, arXiv:hep-lat/0102013.

[46] B. Blossier, P. Boucaud, M. Brinet, F. De Soto, Z. Liu, V. Morenas, O. Pene, K. Petrov, and J. Rodriguez-Quintero, "Renormalisation of quark propagators from twisted-mass lattice QCD at N_f=2," *Phys. Rev. D* **83** (2011) 074506, arXiv:1011.2414 [hep-ph].

[47] F. Burger, V. Lubicz, M. Müller-Preussker, S. Simula, and C. Urbach, "Quark mass and chiral condensate from the Wilson twisted mass lattice quark propagator," *Phys. Rev. D* **87** no. 3, (2013) 034514, arXiv:1210.0838 [hep-lat].

[48] P. O. Bowman, U. M. Heller, and A. G. Williams, "Lattice quark propagator with staggered quarks in Landau and Laplacian gauges," *Phys. Rev. D* **66** (2002) 014505, arXiv:hep-lat/0203001.

[49] M. B. Parappilly, P. O. Bowman, U. M. Heller, D. B. Leinweber, A. G. Williams, and J. B. Zhang, "Scaling behavior of quark propagator in full QCD," *Phys. Rev. D* **73** (2006) 054504, arXiv:hep-lat/0511007.

[50] P. O. Bowman, U. M. Heller, D. B. Leinweber, M. B. Parappilly, A. G. Williams, and J.-b. Zhang, "Unquenched quark propagator in Landau gauge," *Phys. Rev. D* **71** (2005) 054507, arXiv:hep-lat/0501019.

[51] S. Furui and H. Nakajima, "Unquenched Kogut-Susskind quark propagator in lattice Landau gauge QCD," *Phys. Rev. D* **73** (2006) 074503.

[52] **CSSM Lattice** Collaboration, F. D. R. Bonnet, P. O. Bowman, D. B. Leinweber, A. G. Williams, and J.-b. Zhang, "Overlap quark propagator in Landau gauge," *Phys. Rev. D* **65** (2002) 114503, arXiv:hep-lat/0202003.

[53] P. Boucaud, F. de Soto, J. P. Leroy, A. Le Yaouanc, J. Micheli, H. Moutarde, O. Pene, and J. Rodriguez-Quintero, "Quark propagator and vertex: Systematic corrections of hypercubic artifacts from lattice simulations," *Phys. Lett. B* **575** (2003) 256–267, arXiv:hep-lat/0307026.

[54] W. Kamleh, P. O. Bowman, D. B. Leinweber, A. G. Williams, and J. Zhang, "The fat link irrelevant clover overlap quark propagator," *Phys. Rev. D* **71** (2005) 094507, arXiv:hep-lat/0412022.

[55] **CSSM Lattice** Collaboration, J. B. Zhang, P. O. Bowman, D. B. Leinweber, A. G. Williams, and F. D. R. Bonnet, "Scaling behavior of the overlap quark propagator in Landau gauge," *Phys. Rev. D* **70** (2004) 034505, arXiv:hep-lat/0301018.

[56] J. B. Zhang, P. O. Bowman, R. J. Coad, U. M. Heller, D. B. Leinweber, and A. G. Williams, "Quark propagator in Landau and Laplacian gauges with overlap fermions," *Phys. Rev. D* **71** (2005) 014501, arXiv:hep-lat/0410045.

[57] W. Kamleh, P. O. Bowman, D. B. Leinweber, A. G. Williams, and J. Zhang, "Unquenching effects in the quark and gluon propagator," *Phys. Rev. D* **76** (2007) 094501, arXiv:0705.4129 [hep-lat].

[58] C. Wang, Y. Bi, H. Cai, Y. Chen, M. Gong, and Z. Liu, "Quark chiral condensate from the overlap quark propagator," *Chin. Phys. C* **41** no. 5, (2017) 053102, arXiv:1612.04579 [hep-lat].

[59] M. Pak and M. Schröck, "Overlap Quark Propagator in Coulomb Gauge QCD and the Interrelation of Confinement and Chiral Symmetry Breaking," *Phys. Rev. D* **91** no. 7, (2015) 074515, arXiv:1502.07706 [hep-lat].

[60] M. Schrock, "The chirally improved quark propagator and restoration of chiral symmetry," *Phys. Lett. B* **711** (2012) 217–224, arXiv:1112.5107 [hep-lat].

[61] G. Burgio, M. Schrock, H. Reinhardt, and M. Quandt, "Running mass, effective energy and confinement: the lattice quark propagator in Coulomb gauge," *Phys. Rev. D* **86** (2012) 014506, arXiv:1204.0716 [hep-lat].

[62] D. Becirevic, P. Boucaud, J. P. Leroy, J. Micheli, O. Pene, J. Rodriguez-Quintero, and C. Roiesnel, "Asymptotic behavior of the gluon propagator from lattice QCD," *Phys. Rev. D* **60** (1999) 094509, arXiv:hep-ph/9903364.

[63] F. de Soto and C. Roiesnel, "On the reduction of hypercubic lattice artifacts," *JHEP* **09** (2007) 007, arXiv:0705.3523 [hep-lat].

[64] S. Aoki *et al.*, "2+1 Flavor Lattice QCD toward the Physical Point," *Phys. Rev. D* **79** (2009) 034503, arXiv:0807.1661 [hep-lat].

[65] **CP-PACS, JLQCD** Collaboration, S. Aoki *et al.*, "Nonperturbative O(a) improvement of the Wilson quark action with the RG-improved gauge action using the Schrödinger functional method," *Phys. Rev. D* **73** (2006) 034501, arXiv:hep-lat/0508031.

[66] Y. Iwasaki, "Renormalization Group Analysis of Lattice Theories and Improved Lattice Action: Two-Dimensional Nonlinear O(N) Sigma Model," *Nucl. Phys. B* **258** (1985) 141–156.

[67] M. Luscher, "Lattice QCD and the Schwarz alternating procedure," *JHEP* **05** (2003) 052, arXiv:hep-lat/0304007.

[68] M. Luscher, "Schwarz-preconditioned HMC algorithm for two-flavour lattice QCD," *Comput. Phys. Commun.* **165** (2005) 199–220, arXiv:hep-lat/0409106.

[69] M. Hasenbusch, "Speeding up the hybrid Monte Carlo algorithm for dynamical fermions," *Phys. Lett. B* **519** (2001) 177–182, arXiv:hep-lat/0107019.

[70] M. Hasenbusch and K. Jansen, "Speeding up lattice QCD simulations with clover improved Wilson fermions," *Nucl. Phys. B* **659** (2003) 299–320, arXiv:hep-lat/0211042.

[71] R. C. Brower, T. Ivanenko, A. R. Levi, and K. N. Orginos, "Chronological inversion method for the Dirac matrix in hybrid Monte Carlo," *Nucl. Phys. B* **484** (1997) 353–374, arXiv:hep-lat/9509012.

[72] M. L. Parks, E. de Sturler, G. Mackey, D. D. Johnson, and S. Maiti, "Recycling krylov subspaces for sequences of linear systems," *SIAM Journal on Scientific Computing* **28** no. 5, (2006) 1651–1674, https://doi.org/10.1137/040607277. https://doi.org/10.1137/040607277.

[73] P. de Forcrand and T. Takaishi, "Fast fermion Monte Carlo," *Nucl. Phys. B Proc. Suppl.* **53** (1997) 968–970, arXiv:hep-lat/9608093.

[74] R. Frezzotti and K. Jansen, "A Polynomial hybrid Monte Carlo algorithm," *Phys. Lett. B* **402** (1997) 328–334, arXiv:hep-lat/9702016.

[75] R. Frezzotti and K. Jansen, "The PHMC algorithm for simulations of dynamical fermions. 2. Performance analysis," *Nucl. Phys. B* **555** (1999) 432–453, arXiv:hep-lat/9808038.

[76] R. Frezzotti and K. Jansen, "The PHMC algorithm for simulations of dynamical fermions: 1. Description and properties," *Nucl. Phys. B* **555** (1999) 395–431, arXiv:hep-lat/9808011.

[77] **JLQCD** Collaboration, S. Aoki *et al.*, "Polynomial hybrid Monte Carlo algorithm for lattice QCD with odd number of flavors," *Phys. Rev. D* **65** (2002) 094507, arXiv:hep-lat/0112051.

[78] P. de Forcrand, "UV filtered fermionic Monte Carlo," *Nucl. Phys. B Proc. Suppl.* **73** (1999) 822–824, arXiv:hep-lat/9809145.

[79] C. Alexandrou, P. de Forcrand, M. D'Elia, and H. Panagopoulos, "Efficiency of the UV filtered multiboson algorithm," *Phys. Rev. D* **61** (2000) 074503, arXiv:hep-lat/9906029.

[80] C. Alexandrou, P. de Forcrand, M. D'Elia, and H. Panagopoulos, "Improved multiboson algorithm," *Nucl. Phys. B Proc. Suppl.* **83** (2000) 765–767, arXiv:hep-lat/9909004.

[81] **PACS-CS** Collaboration, K. I. Ishikawa, S. Aoki, T. Ishikawa, N. Ishizuka, K. Kanaya, Y. Kuramashi, M. Okawa, Y. Taniguchi, A. Ukawa, and T. Yoshi, "An Application of the UV-filtering preconditioner to the polynomial hybrid Monte Carlo algorithm," *PoS* **LAT2006** (2006) 027, arXiv:hep-lat/0610037.

[82] G. P. Lepage and P. B. Mackenzie, "On the viability of lattice perturbation theory," *Phys. Rev. D* **48** (1993) 2250–2264, arXiv:hep-lat/9209022.

[83] **UKQCD** Collaboration, D. B. Leinweber, J. I. Skullerud, A. G. Williams, and C. Parrinello, "Gluon propagator in the infrared region," *Phys. Rev. D* **58** (1998) 031501, arXiv:hep-lat/9803015.

[84] **UKQCD** Collaboration, D. B. Leinweber, J. I. Skullerud, A. G. Williams, and C. Parrinello, "Asymptotic scaling and infrared behavior of the gluon propagator," *Phys. Rev. D* **60** (1999) 094507, arXiv:hep-lat/9811027. [Erratum: Phys.Rev.D 61, 079901 (2000)].

[85] F. D. R. Bonnet, P. O. Bowman, D. B. Leinweber, A. G. Williams, and D. G. Richards, "Discretization errors in Landau gauge on the lattice," *Austral. J. Phys.* **52** (1999) 939–948, arXiv:hep-lat/9905006.

[86] **RBC, UKQCD** Collaboration, R. J. Hudspith, "Fourier Accelerated Conjugate Gradient Lattice Gauge Fixing," *Comput. Phys. Commun.* **187** (2015) 115–119, arXiv:1405.5812 [hep-lat].

[87] C. S. Fischer and R. Alkofer, "Nonperturbative propagators, running coupling and dynamical quark mass of Landau gauge QCD," *Phys. Rev. D* **67** (2003) 094020, arXiv:hep-ph/0301094.

[88] A. C. Aguilar and J. Papavassiliou, "Chiral symmetry breaking with lattice propagators," *Phys. Rev. D* **83** (2011) 014013, arXiv:1010.5815 [hep-ph].

[89] F. Gao, J. Papavassiliou, and J. M. Pawlowski, "Fully coupled functional equations for the quark sector of QCD," *Phys. Rev. D* **103** no. 9, (2021) 094013, arXiv:2102.13053 [hep-ph].

[90] A. C. Aguilar, J. C. Cardona, M. N. Ferreira, and J. Papavassiliou, "Quark gap equation with non-abelian Ball-Chiu vertex," *Phys. Rev. D* **98** no. 1, (2018) 014002, arXiv:1804.04229 [hep-ph].

[91] A. C. Aguilar, D. Binosi, and J. Papavassiliou, "Unquenching the gluon propagator with Schwinger-Dyson equations," *Phys. Rev. D* **86** (2012) 014032, arXiv:1204.3868 [hep-ph].

[92] J. Skullerud and A. Kizilersu, "Quark gluon vertex from lattice QCD," *JHEP* **09** (2002) 013, arXiv:hep-ph/0205318.

[93] J. I. Skullerud, P. O. Bowman, A. Kizilersu, D. B. Leinweber, and A. G. Williams, "Nonperturbative structure of the quark gluon vertex," *JHEP* **04** (2003) 047, arXiv:hep-ph/0303176.

[94] M. S. Bhagwat and P. C. Tandy, "Quark-gluon vertex model and lattice-QCD data," *Phys. Rev. D* **70** (2004) 094039, arXiv:hep-ph/0407163.

[95] C. S. Fischer, "Infrared properties of QCD from Dyson-Schwinger equations," *J. Phys. G* **32** (2006) R253–R291, arXiv:hep-ph/0605173.

[96] A. Cucchieri, A. Maas, and T. Mendes, "Three-point vertices in Landau-gauge Yang-Mills theory," *Phys. Rev. D* **77** (2008) 094510, arXiv:0803.1798 [hep-lat].

[97] A. Kızılersü, O. Oliveira, P. J. Silva, J.-I. Skullerud, and A. Sternbeck, "Quark-gluon vertex from Nf=2 lattice QCD," *Phys. Rev. D* **103** no. 11, (2021) 114515, arXiv:2103.02945 [hep-lat].

[98] A. Trewartha, W. Kamleh, D. Leinweber, and D. S. Roberts, "Quark Propagation in the Instantons of Lattice QCD," *Phys. Rev. D* **88** (2013) 034501, arXiv:1306.3283 [hep-lat].

[99] A. Trewartha, W. Kamleh, and D. Leinweber, "Evidence that centre vortices underpin dynamical chiral symmetry breaking in SU(3) gauge theory," *Phys. Lett. B* **747** (2015) 373–377, arXiv:1502.06753 [hep-lat].

[100] A. Virgili, W. Kamleh, and D. Leinweber, "Role of chiral symmetry in the nucleon excitation spectrum," *Phys. Rev. D* **101** no. 7, (2020) 074504, arXiv:1910.13782 [hep-lat].

[101] L. D. Roper, "Evidence for a P-11 Pion-Nucleon Resonance at 556 MeV," *Phys. Rev. Lett.* **12** (1964) 340–342.

[102] **CSSM Lattice** Collaboration, M. S. Mahbub, W. Kamleh, D. B. Leinweber, P. J. Moran, and A. G. Williams, "Roper Resonance in 2+1 Flavor QCD," *Phys. Lett. B* **707** (2012) 389–393, arXiv:1011.5724 [hep-lat].

[103] M. S. Mahbub, W. Kamleh, D. B. Leinweber, P. J. Moran, and A. G. Williams, "Structure and Flow of the Nucleon Eigenstates in Lattice QCD," *Phys. Rev. D* **87** no. 9, (2013) 094506, arXiv:1302.2987 [hep-lat].

[104] Z.-W. Liu, W. Kamleh, D. B. Leinweber, F. M. Stokes, A. W. Thomas, and J.-J. Wu, "Hamiltonian effective field theory study of the $\mathbf{N}^*(\mathbf{1440})$ resonance in lattice QCD," *Phys. Rev. D* **95** no. 3, (2017) 034034, arXiv:1607.04536 [nucl-th].

[105] A. L. Kiratidis, W. Kamleh, D. B. Leinweber, and B. J. Owen, "Lattice baryon spectroscopy with multi-particle interpolators," *Phys. Rev. D* **91** (2015) 094509, arXiv:1501.07667 [hep-lat].

[106] A. L. Kiratidis, W. Kamleh, D. B. Leinweber, Z.-W. Liu, F. M. Stokes, and A. W. Thomas, "Search for low-lying lattice QCD eigenstates in the Roper regime," *Phys. Rev. D* **95** no. 7, (2017) 074507, arXiv:1608.03051 [hep-lat].

[107] C. Alexandrou, T. Leontiou, C. N. Papanicolas, and E. Stiliaris, "Novel analysis method for excited states in lattice QCD: The nucleon case," *Phys. Rev. D* **91** no. 1, (2015) 014506, arXiv:1411.6765 [hep-lat].

[108] C. B. Lang, L. Leskovec, M. Padmanath, and S. Prelovsek, "Pion-nucleon scattering in the Roper channel from lattice QCD," *Phys. Rev. D* **95** no. 1, (2017) 014510, arXiv:1610.01422 [hep-lat].

[109] R. G. Edwards, J. J. Dudek, D. G. Richards, and S. J. Wallace, "Excited state baryon spectroscopy from lattice QCD," *Phys. Rev. D* **84** (2011) 074508, arXiv:1104.5152 [hep-ph].

[110] **Hadron Spectrum** Collaboration, R. G. Edwards, N. Mathur, D. G. Richards, and S. J. Wallace, "Flavor structure of the excited baryon spectra from lattice QCD," *Phys. Rev. D* **87** no. 5, (2013) 054506, arXiv:1212.5236 [hep-ph].

[111] J. J. Dudek and R. G. Edwards, "Hybrid Baryons in QCD," *Phys. Rev. D* **85** (2012) 054016, arXiv:1201.2349 [hep-ph].

[112] Y. Chen, S.-J. Dong, T. Draper, I. Horvath, K.-F. Liu, N. Mathur, S. Tamhankar, C. Srinivasan, F. X. Lee, and J.-b. Zhang, "The Sequential empirical bayes method: An Adaptive constrained-curve fitting algorithm for lattice QCD," arXiv:hep-lat/0405001.

[113] K.-F. Liu, Y. Chen, M. Gong, R. Sufian, M. Sun, and A. Li, "The Roper Puzzle," *PoS* **LATTICE2013** (2014) 507, arXiv:1403.6847 [hep-ph].

[114] G. Eichmann, H. Sanchis-Alepuz, R. Williams, R. Alkofer, and C. S. Fischer, "Baryons as relativistic three-quark bound states," *Prog. Part. Nucl. Phys.* **91** (2016) 1–100, arXiv:1606.09602 [hep-ph].

[115] J. Segovia and C. D. Roberts, "Dissecting nucleon transition electromagnetic form factors," *Phys. Rev. C* **94** no. 4, (2016) 042201, arXiv:1607.04405 [nucl-th].

[116] G. Eichmann, C. S. Fischer, and H. Sanchis-Alepuz, "Light baryons and their excitations," *Phys. Rev. D* **94** no. 9, (2016) 094033, arXiv:1607.05748 [hep-ph].

[117] C. Liu, "Review on Hadron Spectroscopy," *PoS* **LATTICE2016** (2017) 006, arXiv:1612.00103 [hep-lat].

[118] G. Yang, J. Ping, and J. Segovia, "The S- and P-Wave Low-Lying Baryons in the Chiral Quark Model," *Few Body Syst.* **59** no. 6, (2018) 113, arXiv:1709.09315 [hep-ph].

[119] X.-L. Ren, "Roper mass in chiral perturbation theory," *PoS* **CD15** (2016) 130.

[120] C. D. Roberts and J. Segovia, "Baryons and the Borromeo," *Few Body Syst.* **57** no. 11, (2016) 1067–1076, arXiv:1603.02722 [nucl-th].

[121] J. Segovia, B. El-Bennich, E. Rojas, I. C. Cloet, C. D. Roberts, S.-S. Xu, and H.-S. Zong, "Completing the picture of the Roper resonance," *Phys. Rev. Lett.* **115** no. 17, (2015) 171801, arXiv:1504.04386 [nucl-th].

[122] N. Mathur, Y. Chen, S. J. Dong, T. Draper, I. Horvath, F. X. Lee, K. F. Liu, and J. B. Zhang, "Roper resonance and S(11)(1535) from lattice QCD," *Phys. Lett. B* **605** (2005) 137–143, arXiv:hep-ph/0306199.

[123] J.-j. Wu, D. B. Leinweber, Z.-w. Liu, and A. W. Thomas, "Structure of the Roper Resonance from Lattice QCD Constraints," *Phys. Rev. D* **97** no. 9, (2018) 094509, arXiv:1703.10715 [nucl-th].

[124] M. Padmanath, "Hadron Spectroscopy and Resonances: Review," *PoS* **LATTICE2018** (2018) 013, arXiv:1905.09651 [hep-lat].

[125] M. Luscher, "Two particle states on a torus and their relation to the scattering matrix," *Nucl. Phys. B* **354** (1991) 531–578.

[126] J. M. M. Hall, A. C. P. Hsu, D. B. Leinweber, A. W. Thomas, and R. D. Young, "Finite-volume matrix Hamiltonian model for a $\Delta \to N\pi$ system," *Phys. Rev. D* **87** no. 9, (2013) 094510, arXiv:1303.4157 [hep-lat].

[127] Y. Li, J.-J. Wu, C. D. Abell, D. B. Leinweber, and A. W. Thomas, "Partial Wave Mixing in Hamiltonian Effective Field Theory," *Phys. Rev. D* **101** no. 11, (2020) 114501, arXiv:1910.04973 [hep-lat].

[128] C. W. Andersen, J. Bulava, B. Hörz, and C. Morningstar, "Elastic $I = 3/2p$-wave nucleon-pion scattering amplitude and the $\Delta(1232)$ resonance from N_f=2+1 lattice QCD," *Phys. Rev. D* **97** no. 1, (2018) 014506, arXiv:1710.01557 [hep-lat].

[129] C. W. Andersen, J. Bulava, B. Hörz, and C. Morningstar, "$I = 3/2N\pi$ scattering and the $\Delta(1232)$ resonance on $N_f = 2 + 1$ CLS ensembles using the stochastic LapH method," *PoS* **LATTICE2019** (2019) 039, arXiv:1911.10021 [hep-lat].

[130] **Alpha** Collaboration, R. Frezzotti, P. A. Grassi, S. Sint, and P. Weisz, "Lattice QCD with a chirally twisted mass term," *JHEP* **08** (2001) 058, arXiv:hep-lat/0101001.

[131] C. Michael, "Adjoint Sources in Lattice Gauge Theory," *Nucl. Phys. B* **259** (1985) 58–76.

[132] M. Luscher and U. Wolff, "How to Calculate the Elastic Scattering Matrix in Two-dimensional Quantum Field Theories by Numerical Simulation," *Nucl. Phys. B* **339** (1990) 222–252.

[133] D. Leinweber, W. Kamleh, A. Kiratidis, Z.-W. Liu, S. Mahbub, D. Roberts, F. Stokes, A. W. Thomas, and J. Wu, "N* Spectroscopy from Lattice QCD:

The Roper Explained," *JPS Conf. Proc.* **10** (2016) 010011, arXiv:1511.09146 [hep-lat].

[134] M. S. Mahbub, A. O. Cais, W. Kamleh, B. G. Lasscock, D. B. Leinweber, and A. G. Williams, "Isolating Excited States of the Nucleon in Lattice QCD," *Phys. Rev. D* **80** (2009) 054507, arXiv:0905.3616 [hep-lat].

[135] S. Gusken, "A Study of smearing techniques for hadron correlation functions," *Nucl. Phys. B Proc. Suppl.* **17** (1990) 361–364.

[136] A. Virgili, W. Kamleh, and D. Leinweber, "Smoothing algorithms for projected center-vortex gauge fields," *Phys. Rev. D* **106** no. 1, (2022) 014505, arXiv:2203.09764 [hep-lat].

[137] K. Langfeld, "Vortex structures in pure SU(3) lattice gauge theory," *Phys. Rev. D* **69** (Jan, 2004) 014503, arXiv:hep-lat/0307030. http://dx.doi.org/10.1103/PhysRevD.69.014503.

[138] A. Montero, "Study of SU(3) vortex - like configurations with a new maximal center gauge fixing method," *Phys. Lett. B* **467** (1999) 106–111, arXiv:hep-lat/9906010.

[139] M. Faber, J. Greensite, and S. Olejnik, "First evidence for center dominance in SU(3) lattice gauge theory," *Phys. Lett. B* **474** (2000) 177–181, arXiv:hep-lat/9911006.

[140] G. 't Hooft, "On the Phase Transition Towards Permanent Quark Confinement," *Nucl. Phys. B* **138** (1978) 1–25.

[141] D. H. Adams, "General bounds on the Wilson-Dirac operator," *Phys. Rev. D* **68** (2003) 065009, arXiv:hep-lat/9907005.

[142] A. Trewartha, W. Kamleh, and D. B. Leinweber, "Centre vortex removal restores chiral symmetry," *J. Phys. G* **44** no. 12, (2017) 125002, arXiv:1708.06789 [hep-lat].

[143] K. Langfeld and E.-M. Ilgenfritz, "Confinement from semiclassical gluon fields in SU(2) gauge theory," *Nucl. Phys. B* **848** (2011) 33–61, arXiv:1012.1214 [hep-lat].

[144] R. Höllwieser and M. Engelhardt, "Approaching $SU(2)$ gauge dynamics with smeared $Z(2)$ vortices," *Phys. Rev. D* **92** no. 3, (2015) 034502, arXiv:1503.00016 [hep-lat].

[145] M. Lüscher, "Trivializing maps, the wilson flow and the hmc algorithm," *Commun. Math. Phys.* **293** no. 3, (Nov, 2009) 899–919, arXiv:0907.5491 [hep-lat]. http://dx.doi.org/10.1007/s00220-009-0953-7.

[146] M. Lüscher, "Properties and uses of the Wilson flow in lattice QCD," *JHEP* **08** (2010) 071, arXiv:1006.4518 [hep-lat]. http://dx.doi.org/10.1007/JHEP08(2010)071. [Erratum: JHEP 03, 092 (2014)].

[147] W. Kamleh, D. B. Leinweber, and A. G. Williams, "Hybrid Monte Carlo with fat link fermion actions," *Phys. Rev. D* **70** (2004) 014502, arXiv:hep-lat/0403019.

[148] S. Duane, A. D. Kennedy, B. J. Pendleton, and D. Roweth, "Hybrid Monte Carlo," *Phys. Lett. B* **195** (1987) 216–222.

[149] M. Falcioni, M. L. Paciello, G. Parisi, and B. Taglienti, "AGAIN ON SU(3) GLUEBALL MASS," *Nucl. Phys. B* **251** (1985) 624–632.

[150] M. Albanese *et al.*, "Glueball Masses and String Tension in Lattice QCD," *Phys. Lett. B* **192** (1987) 163–169.

[151] M. Garcia Perez, A. Gonzalez-Arroyo, J. R. Snippe, and P. van Baal, "Instantons from over - improved cooling," *Nucl. Phys. B* **413** (1994) 535–552, arXiv:hep-lat/9309009.

[152] F. D. R. Bonnet, D. B. Leinweber, A. G. Williams, and J. M. Zanotti, "Improved smoothing algorithms for lattice gauge theory," *Phys. Rev. D* **65** (2002) 114510, arXiv:hep-lat/0106023.

[153] P. J. Moran and D. B. Leinweber, "Over-improved stout-link smearing," *Phys. Rev. D* **77** (2008) 094501, arXiv:0801.1165 [hep-lat].

[154] N. Cabibbo and E. Marinari, "A New Method for Updating SU(N) Matrices in Computer Simulations of Gauge Theories," *Phys. Lett. B* **119** (1982) 387–390.

[155] F. D. R. Bonnet, D. B. Leinweber, and A. G. Williams, "General algorithm for improved lattice actions on parallel computing architectures," *J. Comput. Phys.* **170** (2001) 1–17, arXiv:hep-lat/0001017.

[156] F. D. R. Bonnet, P. Fitzhenry, D. B. Leinweber, M. R. Stanford, and A. G. Williams, "Calibration of smearing and cooling algorithms in SU(3): Color gauge theory," *Phys. Rev. D* **62** (2000) 094509, arXiv:hep-lat/0001018.

[157] B. Berg, "Dislocations and Topological Background in the Lattice O(3) σ Model," *Phys. Lett. B* **104** (1981) 475–480.

[158] M. Teper, "Instantons in the Quantized SU(2) Vacuum: A Lattice Monte Carlo Investigation," *Phys. Lett. B* **162** (1985) 357–362.

[159] M. Teper, "Axial Anomaly Suppression (and Axial U(1) Symmetry Restoration) at High Temperatures: A Lattice Monte Carlo Study," *Phys. Lett. B* **171** (1986) 81–85.

[160] M. Teper, "The Topological Susceptibility in SU(2) Lattice Gauge Theory: An Exploratory Study," *Phys. Lett. B* **171** (1986) 86–94.

[161] E.-M. Ilgenfritz, M. L. Laursen, G. Schierholz, M. Muller-Preussker, and H. Schiller, "First Evidence for the Existence of Instantons in the Quantized SU(2) Lattice Vacuum," *Nucl. Phys. B* **268** (1986) 693.

[162] M. F. Atiyah and I. M. Singer, "The Index of elliptic operators. 1," *Annals Math.* **87** (1968) 484–530.

[163] R. Narayanan and P. M. Vranas, "A Numerical test of the continuum index theorem on the lattice," *Nucl. Phys. B* **506** (1997) 373–386, arXiv:hep-lat/9702005.

[164] P. J. Moran and D. B. Leinweber, "Impact of Dynamical Fermions on QCD Vacuum Structure," *Phys. Rev. D* **78** (2008) 054506, arXiv:0801.2016 [hep-lat].

[165] P. J. Moran, D. B. Leinweber, and J. Zhang, "Wilson mass dependence of the overlap topological charge density," *Phys. Lett. B* **695** (2011) 337–342, arXiv:1007.0854 [hep-lat].

[166] M. Teper, "More methods for calculating the topological charge (density) of SU(N) lattice gauge fields in 3+1 dimensions," arXiv:2202.02528 [hep-lat].

[167] J. C. Biddle, W. Kamleh, and D. B. Leinweber, "Visualization of center vortex structure," *Phys. Rev. D* **102** no. 3, (2020) 034504, arXiv:1912.09531 [hep-lat].

[168] D. Trewartha, W. Kamleh, and D. Leinweber, "Connection between center vortices and instantons through gauge-field smoothing," *Phys. Rev. D* **92** no. 7, (2015) 074507, arXiv:1509.05518 [hep-lat].

[169] S. O. Bilson-Thompson, D. B. Leinweber, and A. G. Williams, "Highly improved lattice field strength tensor," *Annals Phys.* **304** (2003) 1–21, arXiv:hep-lat/0203008.

[170] G. 't Hooft, "A Property of Electric and Magnetic Flux in Nonabelian Gauge Theories," *Nucl. Phys. B* **153** (1979) 141–160.

[171] L. Del Debbio, M. Faber, J. Greensite, and S. Olejnik, "Center dominance and Z(2) vortices in SU(2) lattice gauge theory," *Phys. Rev. D* **55** (1997) 2298–2306, arXiv:hep-lat/9610005.

[172] M. Faber, J. Greensite, and S. Olejnik, "Casimir scaling from center vortices: Towards an understanding of the adjoint string tension," *Phys. Rev. D* **57** (1998) 2603–2609, arXiv:hep-lat/9710039.

[173] L. Del Debbio, M. Faber, J. Giedt, J. Greensite, and S. Olejnik, "Detection of center vortices in the lattice Yang-Mills vacuum," *Phys. Rev. D* **58** (1998) 094501, arXiv:hep-lat/9801027.

[174] R. Bertle, M. Faber, J. Greensite, and S. Olejnik, "The Structure of projected center vortices in lattice gauge theory," *JHEP* **03** (1999) 019, arXiv:hep-lat/9903023.

[175] P. de Forcrand and M. D'Elia, "On the relevance of center vortices to QCD," *Phys. Rev. Lett.* **82** (1999) 4582–4585, arXiv:hep-lat/9901020.

[176] M. Faber, J. Greensite, S. Olejnik, and D. Yamada, "The Vortex finding property of maximal center (and other) gauges," *JHEP* **12** (1999) 012, arXiv:hep-lat/9910033.

[177] M. Engelhardt, K. Langfeld, H. Reinhardt, and O. Tennert, "Deconfinement in SU(2) Yang-Mills theory as a center vortex percolation transition," *Phys. Rev. D* **61** (2000) 054504, arXiv:hep-lat/9904004.

[178] M. Engelhardt and H. Reinhardt, "Center projection vortices in continuum Yang-Mills theory," *Nucl. Phys. B* **567** (2000) 249, arXiv:hep-th/9907139.

[179] M. Engelhardt, "Center vortex model for the infrared sector of Yang-Mills theory: Topological susceptibility," *Nucl. Phys.* **B585** (2000) 614, arXiv:hep-lat/0004013 [hep-lat].

[180] R. Bertle, M. Faber, J. Greensite, and S. Olejnik, "P vortices, gauge copies, and lattice size," *JHEP* **10** (2000) 007, arXiv:hep-lat/0007043.

[181] K. Langfeld, H. Reinhardt, and J. Gattnar, "Gluon propagators and quark confinement," *Nucl. Phys. B* **621** (2002) 131–156, arXiv:hep-ph/0107141.

[182] M. Engelhardt, "Center vortex model for the infrared sector of Yang-Mills theory: Quenched Dirac spectrum and chiral condensate," *Nucl. Phys. B* **638** (2002) 81–110, arXiv:hep-lat/0204002.

[183] J. Greensite, "The Confinement problem in lattice gauge theory," *Prog. Part. Nucl. Phys.* **51** (2003) 1, arXiv:hep-lat/0301023.

[184] F. Bruckmann and M. Engelhardt, "Writhe of center vortices and topological charge: An Explicit example," *Phys. Rev.* **D68** (2003) 105011, arXiv:hep-th/0307219 [hep-th].

[185] M. Engelhardt, M. Quandt, and H. Reinhardt, "Center vortex model for the infrared sector of SU(3) Yang-Mills theory: Confinement and deconfinement," *Nucl. Phys. B* **685** (2004) 227–248, arXiv:hep-lat/0311029.

[186] P. Y. Boyko, V. G. Bornyakov, E. M. Ilgenfritz, A. V. Kovalenko, B. V. Martemyanov, M. Muller-Preussker, M. I. Polikarpov, and A. I. Veselov, "Once more on the interrelation between Abelian monopoles and P-vortices in SU(2) LGT," *Nucl. Phys. B* **756** (2006) 71–85, arXiv:hep-lat/0607003.

[187] E.-M. Ilgenfritz, K. Koller, Y. Koma, G. Schierholz, T. Streuer, V. Weinberg, and M. Quandt, "Localization of overlap modes and topological charge, vortices and monopoles in SU(3) LGT," *PoS* **LATTICE2007** (2007) 311, arXiv:0710.2607 [hep-lat].

[188] V. G. Bornyakov, E. M. Ilgenfritz, B. V. Martemyanov, S. M. Morozov, M. Muller-Preussker, and A. I. Veselov, "Interrelation between monopoles, vortices, topological charge and chiral symmetry breaking: Analysis using overlap fermions for SU(2)," *Phys. Rev. D* **77** (2008) 074507, arXiv:0708.3335 [hep-lat].

[189] P. O. Bowman, K. Langfeld, D. B. Leinweber, A. O' Cais, A. Sternbeck, L. von Smekal, and A. G. Williams, "Center vortices and the quark propagator in SU(2) gauge theory," *Phys. Rev. D* **78** (2008) 054509, arXiv:0806.4219 [hep-lat].

[190] R. Hollwieser, M. Faber, J. Greensite, U. M. Heller, and S. Olejnik, "Center Vortices and the Dirac Spectrum," *Phys. Rev. D* **78** (2008) 054508, arXiv:0805.1846 [hep-lat].

[191] A. O'Cais, W. Kamleh, K. Langfeld, B. Lasscock, D. Leinweber, P. Moran, A. Sternbeck, and L. von Smekal, "Preconditioning Maximal Center Gauge with Stout Link Smearing in SU(3)," *Phys. Rev. D* **82** (2010) 114512, arXiv:0807.0264 [hep-lat].

[192] M. Engelhardt, "Center vortex model for the infrared sector of SU(3) Yang-Mills theory: Topological susceptibility," *Phys. Rev.* **D83** (2011) 025015, arXiv:1008.4953 [hep-lat].

[193] P. O. Bowman, K. Langfeld, D. B. Leinweber, A. Sternbeck, L. von Smekal, and A. G. Williams, "Role of center vortices in chiral symmetry breaking in SU(3) gauge theory," *Phys. Rev. D* **84** (2011) 034501, arXiv:1010.4624 [hep-lat].

[194] E.-A. O'Malley, W. Kamleh, D. Leinweber, and P. Moran, "SU(3) centre vortices underpin confinement and dynamical chiral symmetry breaking," *Phys. Rev. D* **86** (2012) 054503, arXiv:1112.2490 [hep-lat].

[195] R. Höllwieser, T. Schweigler, M. Faber, and U. M. Heller, "Center Vortices and Chiral Symmetry Breaking in SU(2) Lattice Gauge Theory," *Phys. Rev. D* **88** (2013) 114505, arXiv:1304.1277 [hep-lat].

[196] R. Höllwieser, M. Faber, T. Schweigler, and U. M. Heller, "Chiral Symmetry Breaking from Center Vortices," *PoS* **LATTICE2013** (2014) 505, arXiv:1410.2333 [hep-lat].

[197] J. Greensite, "Confinement from Center Vortices: A review of old and new results," *EPJ Web Conf.* **137** (2017) 01009, arXiv:1610.06221 [hep-lat].

[198] J. C. Biddle, W. Kamleh, and D. B. Leinweber, "Gluon propagator on a center-vortex background," *Phys. Rev.* **D98** no. 9, (2018) 094504, arXiv:1806.04305 [hep-lat].

[199] F. Spengler, M. Quandt, and H. Reinhardt, "Branching of Center Vortices in SU(3) Lattice Gauge Theory," *Phys. Rev.* **D98** no. 9, (2018) 094508, arXiv:1810.04072 [hep-th].